# Exploring the Origins of Earth's Nitrogen

by

Thomas Sean Rice

A dissertation submitted in partial fulfillment
of the requirements for the degree of
Doctor of Philosophy
(Astronomy and Astrophysics)
in the University of Michigan
2019

Doctoral Committee:

Professor Edwin Bergin, Chair
Professor Fred Adams
Associate Professor Jes Jørgensen, Københavns Universitet
Professor Michael Meyer
Assistant Professor Emily Rauscher

Thomas Sean Rice

tsrice@umich.edu

ORCID iD: 0000-0002-7231-7328

*For John Goodricke, Annie Jump Cannon, Konstantin Tsiolkovsky, and Henrietta Swan Leavitt. For my parents, for Linda and Rick, and for Tim and Jen. And for all the Deaf people who made me and my work possible.*

# ACKNOWLEDGMENTS

I must give immense thanks to my advisor, Ted Bergin, for six years of careful advising, guidance, and scientific discussion. Likewise, I am incredibly grateful to Jes Jørgensen for hosting me as a guest PhD student at the Centre for Star and Planet Formation (StarPlan) in Copenhagen, Denmark, during two visits in 2017 and 2018 totaling six months, and for invaluable scientific training and collaboration. I am also grateful to the remaining members of my dissertation committee, Michael Meyer, Emily Rauscher, and Fred Adams, for useful guidance and discussion during these past few years, which have contributed to my research success.

For critical help with formatting, copy-editing and proofreading of this dissertation at various stages, I thank Richard Teague, Ian Roederer, Rachael Roettenbacher, Forrest Holden, Anna Cornel, Bryan Terrazas, Wendy Carter-Veale, Erin May, Traci Johnson, Ilse Cleeves, and Kamber Schwarz.

I am incredibly grateful to so many people who have been instrumental to the process of my becoming a scientist. My journey into astrophysics began in 2008, when I met David Charbonneau, the undergraduate advisor of Harvard Astronomy, and he encouraged me to take the introductory astrophysics course Astronomy 16 and to pursue research at the Center for Astrophysics. Through coursework and advising with Dave, and through years of incredibly patient research mentoring by Scott Wolk, I learned a few things about research and decided graduate school would be right for me. Colin Aspin and, later, Bo Reipurth, each mentored me in Hawai‘i, opening up a major way forward for me in astrophysics. Bo, thanks so much for your careful

mentorship. Sean Brittain at Clemson helped propel me forward in the study of forming solar systems. Alyssa Goodman, thank you so much for your mentorship and support as I finished my senior thesis, began grad school, and completed a Master's Thesis.

I spent a major part of my PhD as a visitor in Denmark, where I had the pleasure of receiving the mentorship and friendship of Lars Kristensen. Tak for alt, Lars-Lars, og jeg elskede din Julefrokost. Thanks so much to Mattia, Sigurd, Laura, Charl, Eli, Giulia, Hannah, Mafalda, Siw, and Ninna for making me feel like one of the StarPlan crew.

A Bryan y Alejo: gracias por todo, mis compañeros y amigos. El universo tiene más luz con ustedes. To Kate, Irene, Jenny, Hayley, and Qiana: thank you for restoring my faith. Anna, Megan, and Forrest: thank you for helping me heal.

# TABLE OF CONTENTS

# LIST OF TABLES

**Table**

# LIST OF FIGURES

**Figure**

# LIST OF APPENDICES

**Appendix**

# LIST OF ABBREVIATIONS

**ALMA** Atacama Large Millimeter/submillimeter Array

**AU, au** Astronomical unit

**GMC** Giant Molecular Cloud

**FUV** Far Ultraviolet

**HIFI** Heterodyne Instrument for the Far Infrared

**IOM** Insoluble Organic Matter

**IR** Infrared

**IRAM** Institut de Radioastronomie Millimétrique (Institute for Radio Astronomy in the Millimeter)

**IRAM 30m** Institut de Radioastronomie Millimétrique 30m telescope

**IRAS** Infrared Astronomical Satellite

**ISM** Interstellar medium

**LTE** Local thermodynamic equilibrium

**MCMC** Markov Chain Monte Carlo

**NOEMA** Northern Extended Millimeter Array

**pc** Parsec

**SED** Spectral energy distribution

**SMA** Submillimeter Array

**VLA** Very Large Array

# ABSTRACT

The origins of the ingredients necessary for life on Earth – such as water, carbon, and nitrogen – are unknown, with nitrogen's origins proving to be particularly elusive. By far the most abundant carrier of nitrogen in star-forming regions and protoplanetary disks is molecular nitrogen ($N_2$), which is too volatile to contribute directly to planetesimal formation in any solid form, is not disposed to chemical processing into more refractory forms, and is essentially invisible to astronomical observation. In this dissertation, I investigate the disposition of other nitrogen carriers, especially nitrogen-bearing organics, in a variety of protostellar environments to constrain how nitrogen makes its way into the building blocks of the Earth. In Chapter 2, I use *Herschel* observations to compare the abundance of nitrogen-bearing organics in a high-mass and a low-mass protostellar hot core, finding that HCN is the dominant carrier of nitrogen in organics. Its abundance relative to water ($HCN/H_2O$) can be compared to $N/H_2O$ ratios in comets. Through this comparison, I rule out organic molecular ices as the primary contributor to cometary nitrogen, but identify that they are a likely important donor of the $^{15}N$ isotopic enrichment which is seen in the Earth, comets, and other Solar System terrestrial bodies. I find that refractory forms of nitrogen are the likely source of the majority of cometary nitrogen, but their abundance is difficult to directly constrain or characterize. In Chapter 3, I describe an observational survey using the IRAM 30m and NOEMA observatories to measure HCN towards five additional low-mass protostars, to explore possible variations in the results described in Chapter 2. Here, I use models of the physical and chemical structure of the protostellar envelopes to jointly interpret the single-dish and inter-

ferometric observations. I find that on small scales, the brightness of HCN strongly depends on the bolometric luminosity of each protostar, leading to a strong detection of HCN on small scales in only one of the five protostars. Its abundance is close to the value measured for the low-mass protostar in Chapter 2, but the non-detections towards the other four protostars prevent a broader exploration of variation in HCN abundances in low-mass protostellar hot cores. In Chapter 4, I use high-resolution ALMA observations to better-characterize the physical and chemical properties of one protostar studied in Chapter 3. By comparing high-resolution CS, $CH_3OH$, and $H^{13}CN$ emission, I observe a velocity gradient that I identify as associated with a tentative protostellar disk. NOEMA measurements of the sensitive temperature probe $CH_3CN$ indicate hot gas ($T \approx 170$ K) coincident with this disk, supporting a scenario of active disk accretion. In Chapter 5, I summarize the conclusions of each chapter, and outline several important paths forward for the study of the elusive nitrogen carriers that were the original source of the Earth's nitrogen. Overall, I find evidence supporting a common refractory-centric inheritance of nitrogen among the Galaxy's terrestrial worlds, and I advance the observational study of nitrogen carriers in the planet-forming zones of young protostellar systems.

# CHAPTER I

# Introduction

## 1.1 Motivation: Life Beyond Earth

In 1584, Giordano Bruno, a Dominican friar, published his philosophical dialogue *On the Infinite Universe and Worlds*. In this work, inspired by Nicolaus Copernicus's revolutionary work *On the Revolutions of the Celestial Spheres* (1543) published 41 years earlier, Bruno hypothesized that each star in the night sky was in fact a Sun with its own Earth, and that the Universe was full of Earths with life. Mathematical rigor was brought to this Copernican system by the German astronomer Johannes Kepler (making use of his Danish colleague Tycho Brahe's observations), and the use of the telescope (introduced to astronomy by Galileo Galilei in 1609) securely dislodged the Earth's unique place at the center of the cosmos; the Copernican Revolution was completed by Isaac Newton's unified physical theories of gravity and celestial motion (1687, *Philosophiæ Naturalis Principia Mathematica*). Aided by these twin arms of the telescope and of mathematical physics, astronomers proceeded to steadily proliferate the discovery of new worlds through the 18th and 19th centuries. Uranus was discovered in 1781 by William Herschel, and the dwarf planet Ceres and the asteroids Pallas, Vesta, and Juno were discovered between 1801–1807. Neptune was finally discovered in 1846 by Urbain Le Verrier's mathematical calculations.

Interest in the worlds of our Solar System, and their potential to host life, grew

Part Four Second Magazine Section

The New York Times.

SUNDAY, DECEMBER 9, 1906.

Music—Drama—Art Society—Fashions

# THERE IS LIFE ON THE PLANET MARS

*Prof. Percival Lowell, recognised as the greatest authority on the subject, declares there can be no doubt that living beings inhabit our neighbor world.*

By Lilian Whiting.

THE legions of canals on Mars, forming a colossal and a wisely planned system designed to irrigate the oases of the vast deserts which make up the surface of this planet, are an unanswerable argument for the existence of conscious, intelligent life. A thing made predicates a maker. This truism, of course, was Paley's favorite assertion, but it is none the worse for that. Schiaparelli discovered 104 canals; Prof. Percival Lowell and his staff of the Lowell Observatory at Flagstaff, Arizona, have discovered over 250, and they regard this number as no limit. The larger and more obvious are, like the larger asteroids, discovered first; but in each opposition of the planet the trained sight and skill of the great astronomer who is now held to be the specialist on Mars—the Martian expert, as it were—discovers new and smaller ones.

The observations of Mars present a series of paradoxes. Certain oppositions present the planet comparatively near, certain others more remote. But.

yet safe to assume that the professional tea-taster can so distinguish." In fact, Prof. Lowell lays emphasis on the fact that the astronomer must see with his mind as well as with his eyes.

In consultation with Prof. W. H. Pickering and other eminent counselors the site of the new observatory, whose supreme mission was to be the study of Mars, was selected in Arizona, on account of the steadiness of the air. Flagstaff is on a plateau casts some 7,000 feet above sea level, with the purple peaks of the San Francisco mountains as a background, and in this new observatory the first observation of Mars was made on May 31, 1894, by a telescope whose

quickening to vegetable growth would produce the phenomena we see," says Prof. Lowell. "Set free from the Winter locking up, the water accumulated in the cap starts vegetation, which produces the increased visibility of the canals. Thus started the vegetable quickening passes down the planet surface

The Peaks at Flagstaff, Arizona.

Figure 1.1 *New York Times* front-page headline from December 9, 1906 (Whiting, 1906), accompanying the publication of Percival Lowell's book "Mars and its Canals" (Lowell, 1906).

as telescopic observations grew more sophisticated. Telescopic observations of Mars eventually revealed an interesting and dynamic surface: by 1809, transient dust storms were first seen on Mars, noted as "yellow clouds" by French astronomer Honore Flaugergues. By 1813, Mars' ice caps were noted to show seasonal variation. The poor optical resolution of nineteenth-century telescopes led to over-optimistic interpretations of surface features: in 1877, Giovanni Schiaparelli published maps of Mars with putative identifications of "*canali*," straight-lined features on Mars's surface – perhaps canyons or trenches. The astronomer Percival Lowell interpreted these features as artificial canals, publishing detailed maps of "canals" based on his own observations at his observatory in Flagstaff, Arizona in 1895 (Lowell, 1895). His public claims of artificial canals on Mars (e.g., Fig. 1.1; Whiting 1906) sparked an era of "canal fever" and speculation about life on the Red Planet, inspiring (among other cultural touchstones) the publication of *The War of the Worlds* by H. G. Wells in

1897, which depicts an invasion of Earth by advanced Martian life-forms.

Improved telescopic observations later showed Mars's surface to be devoid of such features, and 20th century astronomy and space exploration revealed the Earth as the only obviously-inhabited world in the Solar System (e.g., as noted for Venus by Sagan, 1961). Faced with the apparent rarity of inhabited worlds in our Solar System, astronomers turned to the rest of the Universe for their methodical search for extraterrestrial life. One notable step taken in this direction has been the so-called Drake equation (Drake, 1962), a symbolic way to estimate the number $N$ of presently-communicating extraterrestrial civilizations in our Galaxy:

$$N = R_* \cdot f_p \cdot N_e \cdot f_l \cdot f_i \cdot f_c \cdot L \tag{1.1}$$

in which $R_*$ denotes the Galactic rate of formation of stars, $f_p$ is the fraction of those stars with planetary systems, $N_e$ is the number of planets per solar system with an environment suitable for life, $f_l$ is the fraction of those planets on which life actually appears, $f_i$ is the fraction of life-bearing planets on which intelligent life emerges, $f_c$ is the fraction of civilizations that develop a technology that releases detectable signs of their existence into space, and $L$ is the length of time these civilizations release such signals into space. In this newly-minted framework, an immediately-identifiable unknown was the fraction of stars in the Galaxy which hosted planets ($f_p$). Although it appeared unlikely, it seemed entirely possible that the Solar System was unique, with all other stars devoid of planetary companions.

Searches for planets around other stars (so-called extrasolar planets, or "exoplanets") took place in the latter half of the 20th century, and the first unambiguous discovery of a planet around a main-sequence star came in 1995, with the discovery of 51 Pegasi b (Mayor & Queloz, 1995) inferred from periodic radial velocity perturbations of 51 Peg. Four years later, a planet around HD 209458 was seen transiting the

face of its host star (Charbonneau et al., 2000; Henry et al., 2000), causing a regular 1.7% dip in brightness as seen from Earth. Widespread radial-velocity and transit surveys have proliferated in the two decades since, culminating in the now-complete *Kepler* mission (Borucki et al. 2010, which has discovered 2,662 planets to-date[1]), and the recently-launched Transiting Exoplanet Survey Satellite (TESS, Ricker et al. 2015), which is surveying the sky for transiting planets around bright stars that will facilitate sensitive follow-up. Among the results of these surveys has been the finding that multi-planet systems are both common and diverse (Weiss et al., 2018) and that a great many stars have small, rocky worlds in their so-called "habitable zone" (Dressing & Charbonneau, 2015).

Exoplanet surveys like *Kepler* and TESS can yield numbers, radii, and orbital parameters of detected planets and, in combination with ground-based radial velocity surveys, can allow planet masses to be measured, helping constrain $f_p$ and partly constraining $N_e$. However, the habitability of a planet (i.e, its suitability for life) depends not only on its bulk composition (small, rocky worlds seem more suitable than gas giants) and the amount of sunlight that it receives (life thrives in not-too-cold and not-too-hot conditions), but also on the chemical composition of the planet's surface and its atmosphere. The surface-layer composition not only moderates the temperature (e.g., due to the greenhouse effect, which is active on Earth and keeps our surface temperature above the freezing point of water), but also determines whether the chemical materials for life are present or absent in sufficient quantities. Fortunately, the atmospheres of exoplanets are, in principle, amenable to study: various methods of detecting and characterizing the atmospheres of exoplanets, including (most notably) transmission spectroscopy (Seager & Sasselov, 2000; Charbonneau et al., 2002), have been developed, and these methods are maturing when applied to warm and hot Jupiter-sized planets as well as "super-Neptunes" (e.g., May et al.

[1]Up-to-date *Kepler* mission statistics can be found on-line at `https://www.nasa.gov/kepler/missionstatistics/`.

2018b,a). The promise of identifying specific molecules in planet atmospheres that indicate the presence of life, the so-called "biosignatures" (Seager et al., 2016; Seager, 2018) such as $O_2$, $H_2O$, $O_3$, $CH_4$, and $CO_2$, as well as certain spectroscopic effects such as the "vegetation red edge" (i.e., the signature of a forest-covered planet with plants that reflect light strongly at wavelengths longer than $\sim 750$ nm; Seager et al. 2005), has received considerable attention. Unfortunately, the readily-detectable atmospheres of gas giant planets have little in common with the paltry atmospheres of Earth-like terrestrial worlds, and as such, present-day astronomical observatories (as of mid-2019) lack the sensitivity to detect and characterize such a signal from the atmosphere of an Earth-like world. To make matters more difficult, even the next generation of spaceborne telescopes (e.g., the 6.5 m James Webb Space Telescope, JWST) and giant ground-based observatories (such as the 39.3 m Extremely Large Telescope, ELT; the 24.5 m Giant Magellan Telescope, GMT; and the Thirty Meter Telescope, TMT) will only be able to measure the atmospheric composition of the nearest small handful of terrestrial worlds even in the most optimistic scenarios, as noted by Beichman et al. (2014) and Lopez-Morales et al. (2019).

A true statistical understanding of $N_e$, the number of potentially habitable worlds per planetary system, via direct studies of exoplanets thus seems elusive for the next many years. Given this, further progress on better-constraining the number of habitable (and inhabited) worlds in our Galaxy must come from another direction. In the following, I discuss how a better understanding of the formation of solar systems and especially the chemical inheritance of their terrestrial worlds is one of the best ways forward.

## 1.2 Making a Habitable Planet

As noted in the previous section, the prospects for a direct empirical census of terrestrial exoplanet surface compositions is out of reach even in the coming era

of JWST and extremely large ground-based telescopes. Here, I discuss another way forward: indirectly constraining habitability[2] by studying the materials available upon the formation of a young terrestrial world.

### 1.2.1 Forming terrestrial worlds

Because our knowledge of habitable worlds is limited to rocky worlds like the Earth, we here discuss the formation of those rocky (i.e., terrestrial) worlds to the exclusion of other types of planets. Planet formation happens within the broad context of star formation: the gravitational contraction of clouds of gas and dust into a centrally massive, luminous object powered by nuclear burning (a star) potentially surrounded by orbiting planets. A schematic of the star and planet formation process is shown in Fig. 1.2. This process can be said to begin in the interstellar medium (ISM). Here, cold gas primarily composed of molecular hydrogen ($H_2$) and atomic helium (He), with modest amounts of carbon monoxide (CO) and other less-abundant trace molecules, as well as $\sim 1\%$ dust[3] by mass, of size typically $< 0.1$ $\mu$m, resides in so-called giant molecular clouds (GMCs). These clouds are thought to be supported against collapse by a combination of turbulence and magnetic fields. A detailed review of GMCs and their properties appears in Heyer & Dame (2015). In the GMC phase, small pockets of dense gas can overcome these supporting pressures through various means including a kinetic "kick" from a nearby shock or supernova, beginning a collapse into denser stages such as the "cold dark cloud" (Bergin & Tafalla, 2007) or "dense pre-stellar core". As a pre-stellar core progressively collapses, a protostar forms

[2]Generally, a planet is considered "habitable" if it has a surface that supports the presence of liquid water and an atmosphere. More detailed definitions of habitability, alongside discussions of these definitions, can be found in Kasting et al. (1993); Lammer et al. (2009); Kopparapu et al. (2013).

[3]The detailed description of an interstellar substance which caused both the reddening and obscuration of distant stars was first presented by Trumpler (1930), who identified a "fine cosmic dust" which resided in a thin plane aligned with the Milky Way. The description of this substance took various names before it settled upon the standard "interstellar dust", with some authors calling it "smoke" – with which it shares many properties – as late as 1946 (Oort & van de Hulst). A review of interstellar dust grains appears in Draine (2003).

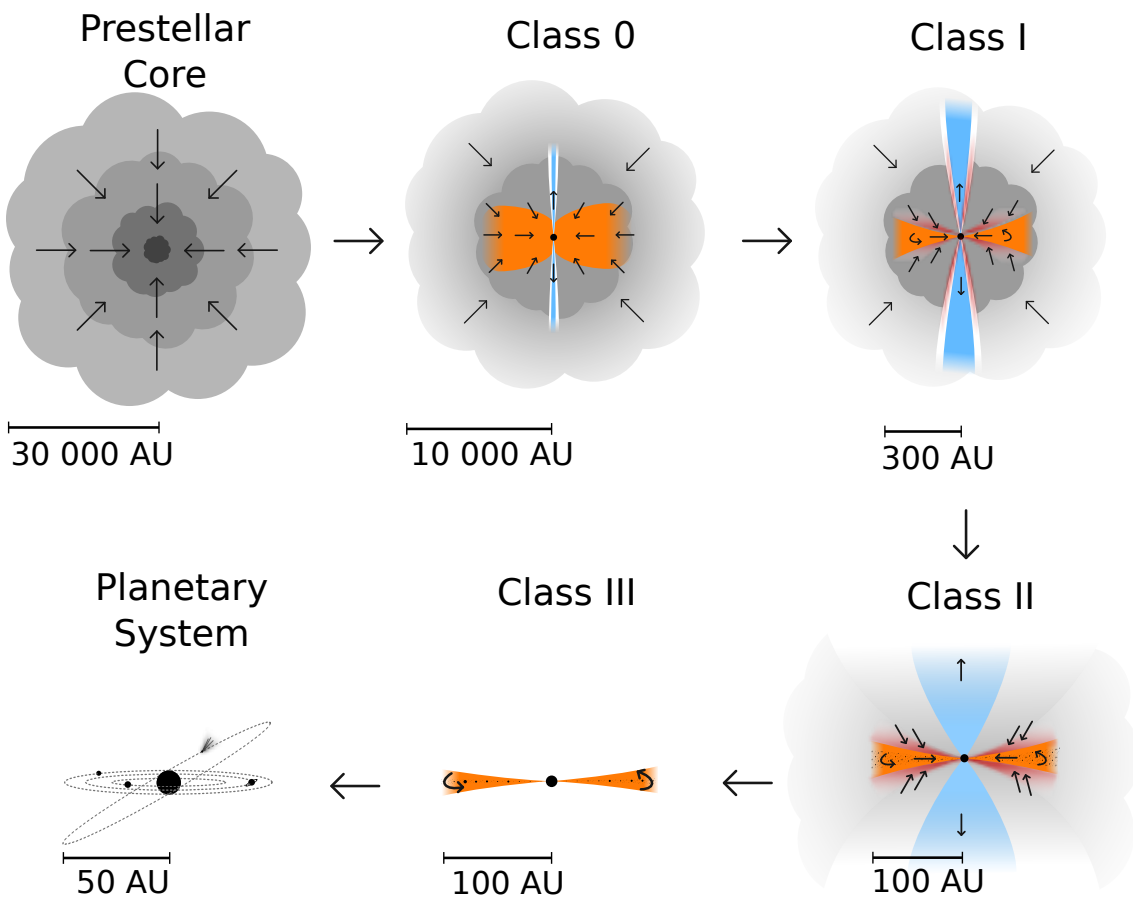


Figure 1.2 A schematic view of the evolutionary stages of star and planet formation. In this dissertation, I focus most on Class 0 and I objects, while I discuss links to earlier and later stages, especially the finished planetary system. Image credit: "Current view of protostellar evolution," Persson (2014).

and begins to release energy from its gravitational collapse and heat its immediate environment. Around this protostar, a disk of gas and dust forms, which eventually grows into a so-called "protoplanetary disk" while the cloud of material around the protostar (now known as its "envelope") dissipates by a combination of accretion onto the disk and outflowing material pushing it away.

During these stages of star formation, the microscopic dust grains begin to grow in size, driven by the simple coagulation (inter-molecular attraction) now facilitated by their higher number density and therefore increased collisional probability. The

dust grains settle to a thin layer in the disk midplanes (Weidenschilling, 1980), where they easily collect. They can grow to ∼cm-sized bodies in this way, but then hit a size at which various forces (including differential drift, the tendency of pebbles to bounce or fragment rather than "stick" upon collision, and other issues) are thought to make it difficult for further solid-body growth (Testi et al., 2014). This issue remains an unsolved problem in our understanding of planetesimal formation, with some proposed solutions including pebble pile-up due to radial gas-pressure bumps (Pinilla et al., 2012) or streaming instabilities (Youdin & Goodman, 2005), among other mechanisms. Once meter-to-kilometer-sized bodies have formed, gravitational attraction in what is called "oligarchical" or "runaway" growth (Greenberg et al., 1978) brings the remaining solid bodies together to rapidly reach planetary size. An overview of terrestrial planet formation is presented by Morbidelli et al. (2012), with a review specifically on pebble accretion presented by Johansen & Lambrechts (2017).

### 1.2.2 Volatiles on terrestrial worlds

Even if a terrestrial planet is formed, the prospects for life as we know it are still dim if the terrestrial world does not receive the chemical ingredients for life, especially carbon, hydrogen, oxygen, and nitrogen – the so-called "CHON" materials. These materials, classified as "volatiles" due to their typically low sublimation temperatures, stand in contrast to the "refractory" materials (with high sublimation temperatures) from which the mass of a terrestrial world is formed. Understanding the origins of the volatiles on Earth is thus a key part of understanding how we got here — it is an unexplained bottleneck in the history of Earth, and if the Earth had formed without its volatile content, life as we know it may have been impossible.

More broadly, because we don't know how exactly the Earth received its volatiles, we don't know if volatile-enriched planets are typical among terrestrial worlds or if the Earth is a fantastic outlier. A related issue is the concept of chemical reset

versus interstellar inheritance: did the Solar System's chemical inventory come from the chemistry of the interstellar medium, or was the formation of the Solar System so violent and high-temperature that the original chemical makeup was destroyed (or "reset"), with the Solar System's current chemical inventory arising strictly from chemical reactions that have taken place since the protoplanetary disk phase at the dawn of the Solar System's formation? An inherited chemistry might imply that the ingredients provided to young worlds are common, while a chemical reset might imply that the peculiar circumstances and conditions in each individual system completely determine the chemical inventory available on young terrestrial worlds.

In our own Solar System, evidence exists for both the "reset" and the "inheritance" scenario. The ubiquitous existence of the primitive "chondrite" meteorites, typically composed of spherical "chondrules"[4] which appear to be minerals that have melted at $T > 1400$ K before re-condensing in space as spherical droplets which are finally bound together by a matrix of fine-grained dust, seem to favor a total high-temperature chemical reset. On the other hand, the ice composition of comets (which are CO-rich), as well as the deuterium enhancement seen in many solar system bodies (Geiss & Gloeckler, 1998), as well as the presence of pre-solar grains in many Solar System rocks (Clayton & Nittler, 2004), provide support for an inheritance of interstellar material that formed at extremely cold temperatures and survived into the end of the planet-forming stage. Given these dichotomies, it may be more a question not of whether there was reset or inheritance, but rather, of how much reset versus how much inheritance. A detailed review of volatiles in protoplanetary disks, and throughout the planet formation process, is given by Pontoppidan et al. (2014).

It is currently unknown how the Earth got the chemical ingredients for life, especially water, carbon, and nitrogen. The rocks from which the Earth formed were predominantly volatile-poor. Specifically, rocks which formed precisely at 1 au from

[4]From Ancient Greek χόνδρος, chondros, "grain." Chondrules, chondrites, and their formation are discussed in Alexander et al. (2008).

the Sun are substantially more depleted in volatiles than the Earth itself (as shown in Figure 1.3, reproduced from Morbidelli et al. 2012). This raises an important question: where did the Earth get its volatiles?

Rocks which form further from the Sun, and therefore in colder conditions, have a higher volatile content, as more volatile material (including water and organics) could remain in a solid form during the initial growth of dust into rocks and planetesimals. A rough division of primitive rocks in the Solar System based on composition would identify three categories: (a) the most volatile-poor rocks (enstatite chondrites), (b) intermediately volatile-rich rocks (ordinary and carbonaceous chondrites), and (c) the most volatile-rich bodies of ice and rock, the comets. Those in category (a) formed closest to the Sun (up to 2 au), those in category (b) formed at intermediate distances (in range 2-3 au), and those in category (c) formed at large distances (beyond 3 au), as discussed in depth in Morbidelli et al. (2012).

Work in reconstructing the Solar System's history indicates that gravitational interactions between the giant planets and the rocky planetesimals have caused large rearrangements in the placement of rocks throughout the Solar System, e.g., via the Nice model and the Grand Tack scenario (Walsh et al., 2011; Raymond et al., 2014). In particular, there was significant transport of more volatile-rich bodies from beyond the Earth's orbit into the inner Solar System, where these bodies contributed significantly to the total mass of the Earth and the other terrestrial worlds (Morbidelli et al., 2012; Albarede et al., 2013). Models of the Solar System's assembly which attempt to recreate Earth's accretion history indicate that the Earth received the majority of its volatiles from these bodies. The Earth should have accreted the first 60–70% of its mass from highly reduced and volatile-poor material, followed by a more oxidized and volatile-rich final 30–40% (Wood et al., 2008; Rubie et al., 2011) which are presumed to be of a primarily chondritic (carbonaceous) origin. Comets appear to have contributed a few percent of the Earth's atmosphere at most, as confirmed

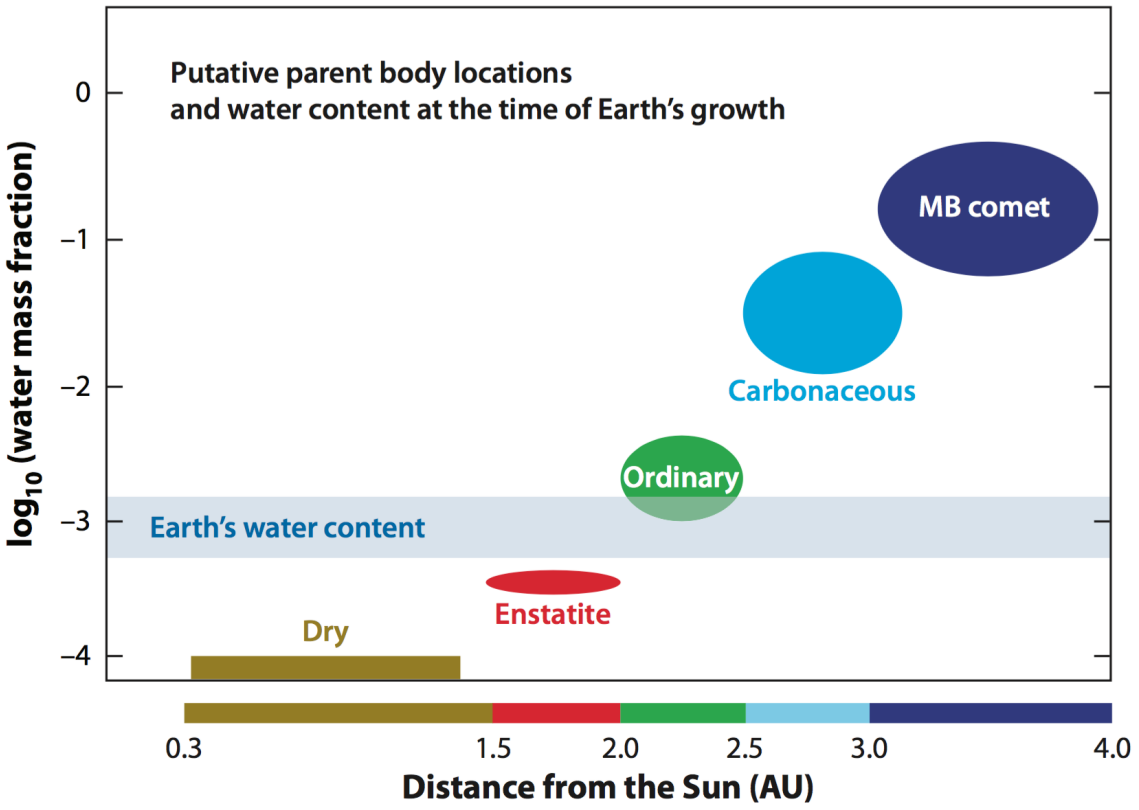


Figure 1.3 Relative proportions of water by mass of different meteorite bodies, as a function of heliocentric distance. Reproduced from Morbidelli et al. (2012), Annual Review of Earth and Planetary Sciences, 40, 251.

by results from the Rosetta spacecraft (Marty et al., 2016), with much of the Earth's noble gases (such up to 22% of Xenon) of likely cometary origin (Marty et al., 2017).

Therefore, prevailing theory suggests that the majority of the Earth's carbon and nitrogen was brought to our still-accreting planet by carbonaceous chondrites. This dissertation focuses on nitrogen. The study of the origins of the Earth's nitrogen, then, is the study of how carbonaceous chondrites received their nitrogen.

## 1.3 Nitrogen

Nitrogen is a key element for life, and is found in all living things. The amino acids necessary for life (in part because they polymerize to form proteins) are so-called because of their *amine* (i.e., $-NH_2$) groups. The nucleic acids such as DNA and RNA are bound together by nitrogenous bases (nucleobases) – which include adenine (A), cytosine (C), guanine (G), thymine (T), and uracil (U), each of which has nitrogen as a primary component (e.g., adenine is $C_5H_5N_5$). The important energy transfer molecule adenosine triphosphate (or ATP) also has nitrogen as a key constituent. By mass, the human body contains is about 3% nitrogen, which is the fourth most abundant element in the body after oxygen, carbon, and hydrogen. Despite both the importance and apparent abundance of nitrogen on the life-giving Earth, the bulk abundance of nitrogen relative to silicon is actually depleted on Earth by 5 orders of magnitude relative to the solar abundance (Pontoppidan et al., 2014; Bergin et al., 2015).

Alexander et al. (2017) describe the insoluble organic matter (IOM) which is a component of the matrix in carbonaceous chondrites. The IOM contains essentially all of the carbon and nitrogen (and much of the hydrogen) in those chondrites, and it is the likely source of carbon and nitrogen to terrestrial worlds. This IOM contains "hot-spots" of enrichment of the isotope nitrogen-15 (written $^{15}N$); van Kooten et al. (2017) study so-called "lithic clasts" inside a carbonaceous chondrite fragment, analyzing how

$^{15}$N enrichment is correlated with mineralogy within these clasts. They comment that the observed variation may be the result of accretion of variable abundances of $NH_3$ and HCN ices. How did nitrogen get into these chondrites?

We are looking at material that, when it was in the interstellar medium and in giant molecular clouds, was in *some* form that has yet to be identified. We know that the bulk carriers of nitrogen in star-forming regions are N I and $N_2$ (van Dishoeck et al., 1993; Schwarz & Bergin, 2014). In the innermost regions of protoplanetary disks (near $\sim$ 1 au), almost none of the expected nitrogen budget is accounted for in observable species (Carr & Najita, 2008, 2011; Salyk et al., 2011; Pontoppidan et al., 2014), in contrast with oxygen and carbon, for which nearly all, and about one-third, respectively, of the elemental budget is accounted for (see Figure 1.4. The implication is that the vast majority of nitrogen is contained in the un-observable $N_2$ in these disk environments. After hydrogen, whose major carrier is $H_2$, nitrogen is the element with the most volatile major carrier ($N_2$); as $N_2$ is consistently more volatile even than CO in a variety of interstellar ice conditions (Fayolle et al., 2016), we expect it to be extremely difficult for any $N_2$-derived nitrogen to end up in rocky materials, even in ice form. Further, disk chemical processes do not appear to facilitate the conversion of $N_2$ into more condensible species: work done by Cleeves et al. (2018) indicates that gas-phase $N_2$ is not efficiently processed into observable forms such as HCN in protoplanetary disks. Further, based on $NH_3$ measurements in the inner few au of disks, species such as $NH_3$ may in fact be back-converted into $N_2$ via warm gas-phase chemistry (Pontoppidan et al., 2019), a process that may be enhanced by cosmic rays (Eistrup et al., 2018). Thus, identifying condensible and refractory nitrogen carriers that could enrich planetesimals and participate in the chemistry that produces N-rich insoluble organic matter is a central concern of theoretical, laboratory, and astronomical studies of the chemistry of planet formation.

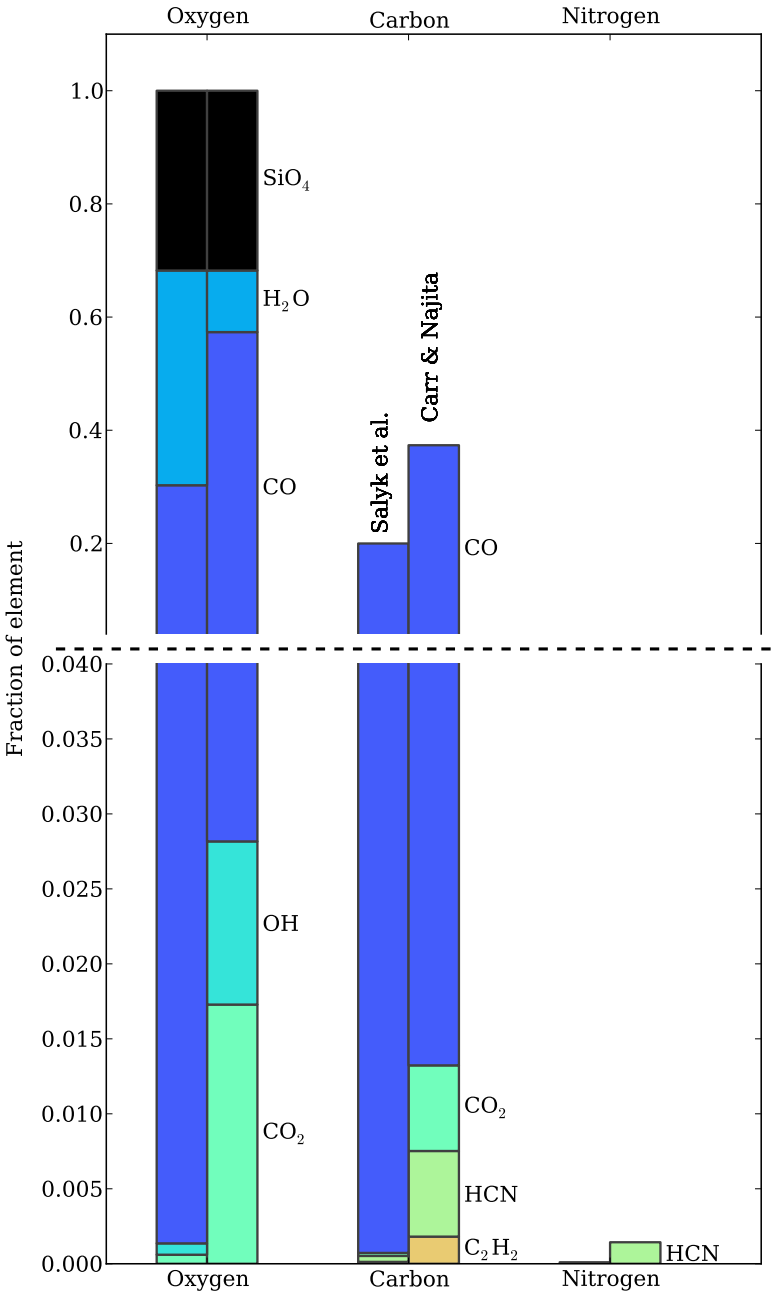


Figure 1.4 Observed elemental abundance budget at $\sim 1$ au in protoplanetary disks. The values retrieved by Salyk et al. (2011), Carr & Najita (2008) and Carr & Najita (2011) are compared side-by-side to provide a rough indication of current uncertainties. All budgets are normalized to the assumption that all oxygen is accounted for in the warm molecular layer (fraction of O= 1). With this assumption, about a 3rd of the carbon is accounted for, and almost none of the nitrogen. The implication is that any missing contribution is located in an as-yet unobserved carrier. Note that the plot has been split into two different y-axis scales to simultaneously show major as well as minor carriers. Reproduced with original caption from Pontoppidan et al. (2014), Protostars and Planets VI.

VOL. LXXXII....No. 27

NEW RADIO WAVES TRACED TO CENTRE OF THE MILKY WAY

Mysterious Static, Reported by K. G. Jansky, Held to Differ From Cosmic Ray.

"Further verification of this direction is required, but the discovery, like that of the cosmic rays and of cosmic radiation, raises many cosmological questions of extreme interest."

There is no indication of any kind, Mr. Jansky replied to a question, that these galactic radio waves constitute some kind of interstellar signalling, or that they are the result of some form of intelligence striving for intra-galactic communication.

Radio Entertains the Children With Crime. Arthur Mann in May Scribner's.—Advt.

Figure 1.5 May 5, 1933 front-page of the *New York Times*, announcing Karl Jansky's discovery of interstellar radio waves, founding the field of radio astronomy (Times, 1933). Right panel: Jansky carefully notes whether these signals are evidence of intelligent life.

## 1.4 Molecular Astrophysics

The history of molecular astrophysics is intimately connected with the history of radio astronomy, which began when Karl Jansky identified a low, persistent radio hiss originating from the Galactic Center (Jansky 1933; see Fig. 1.5; Times 1933). Before radio astronomy was brought to bear upon molecules in interstellar space, early signs of optical absorption by the small molecular species of CN, CH, and $CH^+$ were noted in McKellar (1940); Douglas & Herzberg (1941), but received relatively little notice. The discovery of the 21 cm neutral hydrogen (H I) line by Muller & Oort (1951) and Ewen & Purcell (1951) established the widespread presence of cold clouds of atomic gas in interstellar space. Later that decade, Townes (1957) proposed using radio observations to systematically study atoms and molecules in interstellar space, eventually leading to the first radio detection of a molecular species, OH (Weinreb et al., 1963), via 1.67 GHz absorption against the bright radio source Cassiopeia A.

Emission from interstellar ammonia ($NH_3$) was detected via its 23.6 GHz emission inversion transition by Cheung et al. (1968), bringing attention to the prospect that interstellar space was full of complex and observable molecules. The detection of water ($H_2O$) soon followed (Cheung et al., 1969), as did the first detection of an organic compound, formaldehyde ($H_2CO$) by Snyder et al. (1969). The most abundant detectable[5] interstellar molecule, carbon monoxide (CO), was discovered by Wilson et al. (1970) in Orion. This inaugural period of molecular discoveries was bookended by the discovery of hydrogen cyanide (HCN) by Snyder & Buhl (1971).

The field of astrochemistry – the study of the abundance and reactions of molecules in the Universe, and their interaction with radiation – grew out of these initial radio-astronomical identifications of molecules in interstellar space. An early astrochemical analysis was presented by Herbst & Klemperer (1973), in which a chemical network of over 100 chemical reactions was used to simulate the production and destruction of molecules such as $H_2O$, HCN, $NH_3$, and $H_2CO$, and used to compare against observations. The history of molecular astrophysics since then has yielded the detection of 204 individual molecular species, comprised of 16 different elements, in the interstellar and circumstellar medium by astronomical observations (as of 2018; McGuire). The astrochemical study of star-forming regions, including cold dark clouds, massive embedded protostars, low-mass protostars, a general astrochemical review of gas-grain chemistry in star forming regions, and Earth's astrochemical heritage, are discussed in the following reviews: van Dishoeck & Blake (1998); van der Tak et al. (2000); Ceccarelli et al. (2007); Bergin & Tafalla (2007); Garrod et al. (2008); Caselli & Ceccarelli (2012).

Protostars (young stellar objects still in the process of accreting the bulk of their mass from their natal cloud) are of particular interest to astrochemistry, as they represent an early stage of the star and planet formation process. Following early theoret-

[5]The most abundant molecule in the Universe is $H_2$, but its symmetry and subsequent lack of a dipole moment make it invisible in most practical circumstances.

ical descriptions, the physical structure of protostellar envelopes has been conceived of as following a power-law density profile with $\rho \propto r^{-2}$ or $\rho \propto r^{-1.5}$ (Shu, 1977; Terebey et al., 1984). The modern definition of a so-called "Class 0" protostar was presented by Andre et al. (1993), with the advent of instruments that could perform sub-millimeter mapping of star-forming regions. The joint study of the physical and chemical structure of embedded protostars was developed first with single-dish telescopes (Ceccarelli et al. 2000a,b; Jørgensen et al. 2002; Schöier et al. 2002; Cazaux et al. 2003; Maret et al. 2004, 2005; Jørgensen et al. 2005b; see also Crimier et al. 2010; Caux et al. 2011; Coutens et al. 2012), and then enhanced with interferometric observations (Bottinelli et al., 2004; Jørgensen et al., 2005a, 2007b; Bisschop et al., 2008; Jørgensen et al., 2009; Brinch et al., 2009a). A key use of joint single-dish and interferometric studies is to separate the relative contributions of a large-scale ($\sim$ 10,000 au) envelope from a compact ($\sim$ 100 au) component such as a disk or molecule-bright hot core; single-dish studies are sensitive primarily to large scale material, while interferometers filter this emission out in favor of compact structure, so a comprehensive understanding of the physical and chemical structure of these objects often requires a careful analysis of both types of data. Generally, radiative transfer models such as DUSTY (Ivezic & Elitzur, 1997; Ivezic et al., 1999), Transphere (Dullemond et al., 2002), and RATRAN (Hogerheijde & van der Tak, 2000a) are used to solve the radiation field and molecular level populations within a model protostellar envelope, allowing for accurate comparisons to observational data which account for temperature and density gradients, optical depth effects, and molecular abundance profiles which vary with radius.

### 1.4.1 Recent developments

In the meanwhile, three recent developments have happened in parallel: (a) A realization that many important parts of planet formation happen earlier than the

mature protoplanetary disks now being studied with the Atacama Large Millimeter/submillimeter Array (ALMA), the world's most powerful and sensitive interferometric observatory at millimeter and submillimeter radio wavelengths. (b) With ALMA, we are starting to observe embedded protostellar disks, representing the actual physical and chemical beginnings of planet formation (e.g., Lee et al. 2019; Segura-Cox et al. 2018); (c) Space missions, most notably Rosetta (Fray et al., 2016, 2017), are returning the most sophisticated data ever collected from a comet, a valuable product of planet formation in our solar system that preserves much physical and chemical information of an era in our solar system 4.5 billion years old.

### 1.4.2 Setting the stage for this dissertation

The above pieces of information set the stage for the importance of the following dissertation work, namely:

- An effort to investigate nitrogen-bearing species in interstellar space that would be promising candidates for the precursor to the nitrogen which goes into the IOM in chondrites, ultimately being brought to terrestrial worlds;

- Focusing at the protostellar stage, representing an epoch after simple ice-surface chemistry (e.g., hydrogenation of species such as CO into $CH_3OH$) has chemically enriched the molecules of the cold ISM but before the chemical engine of a protoplanetary disk has substantially processed and altered the molecular inventory inherited from the ISM;

- A program that makes use of the observability boon offered by protostellar hot cores and corinos, which (by virtue of being warm regions near a protostar) are able to sublimate icy molecules into the gas phase where they can be readily seen and characterized by modern mm/submm and FIR spectroscopy.

This thesis, described in the next section, contributes to our understanding of the

origins of Earth's nitrogen, and to the broader questions of the chemical heritage of terrestrial worlds. Ultimately, by inquiring into the likelihood that chemical prerequisites for life are common or rare, it informs our understanding of whether or not we are likely alone in our Universe.

## 1.5 Overview of the Dissertation

In this thesis, I present observational studies of the physical and chemical disposition of nitrogen in protostellar environments, with an eye specifically toward identifying nitrogen that would ultimately become part of terrestrial worlds. For these observational studies, I used archival data from the *Herschel* Space Observatory, and led (as principal investigator) observing campaigns on the European facilities of the Institut de Radioastronomie Millimétrique (IRAM), including the IRAM 30m telescope in Spain and the Northern Extended Millimeter Array (NOEMA)[6] in France, as well as on the Atacama Large Millimeter/submillimeter Array (ALMA) in Chile. My work can be roughly divided into two parts. First (Chapter II), I present an analysis of nitrogen carriers in the best-known protostellar astrochemical laboratories: the high-mass Orion KL Hot Core and the low-mass Class 0 protostar IRAS 16293−2422. I discuss the connections between these results and knowledge obtained from material analyses of our own Solar System. Second (Chapters III and IV), I present an observational effort to extend this study to a broader sample of protostellar environments in order to interrogate whether the conclusions reached in Chapter II hold true, or whether there is widespread chemical diversity observable at this stage.

In Chapter II, we present our analysis of organic nitrogen carriers in protostellar environments. Guided by the work of Hily-Blant et al. (2013) regarding isotopic fractionation of nitrogen in star-forming clouds, we identified organic (carbon-bearing)

[6]NOEMA is an expanded and upgraded version of the interferometric observatory formerly known as the Plateau de Bure Interferometer (PdBI).

molecular carriers of nitrogen as a promising candidate for the nitrogen inherited by carbonaceous chondrites, comets, and ultimately the Earth. Making use of the comprehensive molecular inventory of Orion KL presented by Crockett et al. (2014b), we single out HCN as the organic nitrogen carrier with the highest abundance, containing approximately three-fourths of the nitrogen budget among organic molecules in the high-mass hot core. Taking this analysis to the low-mass protostar IRAS 16293−2422, which also exhibits a rich chemical diversity on small scales (identified as a low-mass hot core or "hot corino"), we reduced and analyzed archival *Herschel* HIFI spectra of a series of HCN, $H^{13}CN$, and $HC^{15}N$ lines which trace molecular states spanning $4 - 273$ K in upper-state energy $E_u/k$. Using a spherically symmetric chemical abundance model, we derive a fractional molecular abundance [HCN/$H_2$] of $X(\mathrm{HCN}) = 6 \pm 1 \times 10^{-8}$ in the hot corino of IRAS 16293−2422. Taking together the organic nitrogen abundances in Orion KL and IRAS 16293−2422, scaled relative to their hot-core $H_2O$ abundances, we connect these astrophysical measurements to N/$H_2O$ ratios in comets, first taking N-bearing ices (including HCN and $NH_3$) into consideration, and then comparing our measurements to the bulk N/$H_2O$ ratio seen in comets. While the measured abundances of nitrogen-bearing organics could account for the N-bearing ices in comets, they are not abundant enough to account for the entirety of the nitrogen seen in a comet (which is dominated by nitrogen in its dust or solid component, rather than nitrogen in ices). We discuss how refractory nitrogen carriers are likely the progenitor of cometary (and, by extension, chondritic) nitrogen, but that molecular ices may still provide an important $^{15}N$ contribution to nitrogen in planetesimals that is ultimately brought to terrestrial worlds.

In Chapter III, we follow up our analysis of IRAS 16293−2422 with single-dish and interferometric line observations of HCN and its isotopologue $H^{13}CN$ towards five additional low-mass embedded protostars. In a series of three IRAM 30m and NOEMA programs which I led as Principal Investigator, we observed the $H^{13}CN$

$3-2$ and $1-0$ lines towards the protostars L1455 IRS1, B1-a, IRAS03235, B5 IRS1, and L1455 IRS4 in Perseus. We also modeled these protostars' physical envelope structure, guided by the methodology of Jørgensen et al. (2005a, 2009), using their spectral energy distributions (SEDs) redward of 50 $\mu$m and continuum interferometric observations. All five protostars have strong $H^{13}CN$ emission on large scales, but we confidently detect bright, compact $H^{13}CN$ emission only towards the brightest protostar in the sample, L1455 IRS1 ($L_{\rm bol} = 5.8 \pm 0.2\ L_{\odot}$). Using a protostellar chemical abundance model similar to that used in Chapter II, we reproduce the single-dish and interferometric $H^{13}CN$ line measurements of L1455 IRS1, deriving a fractional abundance $X({\rm HCN}) = 4 \times 10^{-8}$. We also use this model to place 3-$\sigma$ upper limits on the HCN abundances in the other four protostars, with limits ranging from $4 \times 10^{-8}$ to $3 \times 10^{-7}$. We discuss that the luminosity of the protostar sets the expected size of the sublimation zone in the hot corino, which principally explains the non-detections.

In Chapter IV, we present follow-up measurements of L1455 IRS1, observing its hot core with ALMA at $0\farcs2$ resolution $H^{13}CN$ observations, and with NOEMA at $1\farcs4$ resolution methyl cyanide ($CH_3CN$) observations. We identify differences between these ALMA observations and the chemical abundance model derived in Chapter III, noting that the ALMA observations reveal a more compact, brighter $H^{13}CN$-emitting region than the model had predicted. In the 1.1 mm ALMA continuum map, we also find that L1455 IRS1 is a binary with separation 60 au; essentially all of the $H^{13}CN$ emission is centered on the fainter binary companion. Notably, the partially-resolved $H^{13}CN$ emission shows a velocity gradient consistent with disk rotation, with its resolved size suggesting a disk of $r = 26$ au rotating around a 0.25 $M_{\odot}$ central protostar. Using the sensitive temperature dependence of the $CH_3CN$ spectrum (for which we observe 8 lines spanning $88-442$ K), we infer a temperature of 300 K for the gas in this disk. We discuss what this means for the physical structure of the

innermost part of the envelope.

# CHAPTER II

# Exploring the Origins of Earth's Nitrogen: Astronomical Observations of Nitrogen-bearing Organics in Protostellar Environments

## 2.1 Preface

This work has been adapted by from a paper of the same title in the Astrophysical Journal, Volume 866, page 156 (Rice et al., 2018), with co-authors Edwin A. Bergin, Jes K. Jørgensen, and Susanne Wampfler. The paper is adapted and partially reproduced here under the non-exclusive rights of republication granted by the American Astronomical Society to the paper authors.

## 2.2 Abstract

It is not known whether the original carriers of Earth's nitrogen were molecular ices or refractory dust. To investigate this question, we have used data and results of *Herschel* observations towards two protostellar sources: the high-mass hot core of Orion KL, and the low-mass protostar IRAS 16293−2422. Towards Orion KL, our analysis of the molecular inventory of Crockett et al. (2014b) indicates that HCN is the organic molecule that contains by far the most nitrogen, carrying $74^{+5}_{-9}$% of nitrogen-

in-organics. Following this evidence, we explore HCN towards IRAS 16293−2422, which we consider a solar analog. Towards IRAS 16293−2422, we have reduced and analyzed *Herschel* spectra of HCN, and fit these observations against "jump" abundance models of IRAS 16293−2422's protostellar envelope. We find an inner-envelope HCN abundance $X_{\rm in}= 5.9 \pm 0.7 \times 10^{-8}$ and an outer-envelope HCN abundance $X_{\rm out}= 1.3 \pm 0.1 \times 10^{-9}$. We also find the sublimation temperature of HCN to be $T_{\rm jump}= 71 \pm 3$ K; this measured $T_{\rm jump}$ enables us to predict an HCN binding energy $E_{\rm B}/k = 3840 \pm 140$ K. Based on a comparison of the HCN/$H_2O$ ratio in these protostars to N/$H_2O$ ratios in comets, we find that HCN (and, by extension, other organics) in these protostars is incapable of providing the total bulk N/$H_2O$ in comets. We suggest that refractory dust, not molecular ices, was the bulk provider of nitrogen to comets. However, interstellar dust is not known to have $^{15}$N enrichment, while high $^{15}$N enrichment is seen in both nitrogen-bearing ices and in cometary nitrogen. This may indicate that these $^{15}$N-enriched ices were an important contributor to the nitrogen in planetesimals and likely to the Earth.

## 2.3 Introduction

Earth's nitrogen is a key element for life as well as the primary component of our atmosphere. Because of the high volatility of the key nitrogen carriers in the interstellar medium (atomic N and $N_2$), it is expected that the building blocks of terrestrial worlds would be nitrogen-poor; as a consequence, the origin of Earth's nitrogen is uncertain. The most likely origin scenario is impact delivery by asteroids (probed by meteorites) or icy planetesimals (e.g., comets; Morbidelli et al. 2012). The most recent work suggests an origin in delivery from chondritic meteorites, with a smaller role played by comets (Marty et al., 2016; Alexander et al., 2017, and references therein).

In chondrites (the most primitive meteorites), nitrogen is contained in a macro-

molecular organic form that is insoluble by both acids and solvents, typically known as insoluble organic matter (IOM). As chondrites are the most primitive and most volatile-rich of the meteorites, chondritic IOM is likely the source of the carbon, nitrogen, noble gases, and much of the hydrogen that were delivered to terrestrial planets (Alexander et al., 2012; Marty, 2012; Marty et al., 2013; Alexander et al., 2017). The IOM or its chemical precursors likely formed in the outer solar system and/or the interstellar medium (Charnley & Rodgers, 2008), but it is unknown whether the IOM has a primarily solar or pre-solar origin, or a mix (Alexander et al., 2017, and references therein). Bergin et al. (2014); Bergin et al. (2015) have discussed the astronomical origins of terrestrial carbon, arguing that the initial carriers of terrestrial carbon and nitrogen are organic ices and macromolecular organic material, including dust.

Nitrogen is contained in a variety of molecular and physical carriers in interstellar space, each of which has its own properties – including its volatility (i.e., its sublimation temperature) and its ability to undergo isotopic fractionation (i.e., change its $^{14}N/^{15}N$ ratio). Little is known about which initial carriers could have brought nitrogen into chondritic IOM, but two aspects are relevant. First, while the most volatile forms of nitrogen (atomic N and molecular $N_2$) likely contain the vast majority of nitrogen atoms in the dense interstellar medium (e.g., van Dishoeck et al., 1993; Schwarz & Bergin, 2014), their volatility prevents them from readily incorporating into solid material, so the IOM's nitrogen likely came from carriers with lower volatility. Second, the nitrogen of the IOM is known to be highly enriched $^{15}N$ compared to the ISM standard (Füri & Marty, 2015; Alexander et al., 2017). These factors lead us to consider two families of nitrogen carriers: nitrogen-bearing molecular ices, especially organics, and nitrogen contained in interstellar dust solids (i.e., refractory nitrogen).

Refractory nitrogen has not been directly observed. However, depletion in the

gas-phase atomic nitrogen abundance in the diffuse ISM has been observationally constrained by Knauth et al. (2003) and Jensen et al. (2007). This is generally interpreted as due to nitrogen incorporation into dust grains. Jones (2016) discusses the role of nitrogen in models of interstellar carbonaceous dust.

Some nitrogen-bearing molecular ices, especially including hydrogen cyanide (HCN), exhibit a high $^{15}$N enrichment in interstellar environments (e.g., Hily-Blant et al. 2013; Wampfler et al. 2014; Guzmán et al. 2017) and have a high abundance in the dense ISM (e.g., Crockett et al. 2014b; Zernickel et al. 2012; Schöier et al. 2002, etc.). HCN itself also has a rich chemical reactivity (as noted by, e.g., Noble et al. 2013). Ammonia ($NH_3$) is another very abundant ice constituent, but in the gas does not seem to show the same isotopic signature (Hily-Blant et al., 2013). Motivated by these factors, we here investigate HCN and the family of organic (C-bearing) molecular carriers of nitrogen in their possible role as the initial reservoir of nitrogen that ultimately arrives on terrestrial worlds.

A powerful way to probe the origins of nitrogen in the solar system is through astronomical observations of other forming planetary systems. The success over the past decade of the *Herschel* Space Observatory in submillimeter and far-infrared astronomy has brought a wealth of data and knowledge to the observational astrochemistry community, enabling new frontiers of molecular astrophysics. In this study, we have drawn upon the data and results from these projects, especially the spectral surveys of Orion KL (Bergin et al., 2010; Crockett et al., 2014b) and IRAS 16293−2422 (Ceccarelli et al., 2010; Coutens et al., 2012). The high-mass hot core of Orion KL exhibits a rich molecular spectrum. It represents an environment in which the molecular ices available to planet-forming materials are revealed via sublimation, and hence can be studied astronomically. The molecular abundance inventory presented by Crockett et al. (2014b) of Orion KL enables an investigation of the relative abundances of many molecular species, especially (for our purposes) nitrogen-bearing organics. The

rich HIFI spectrum of IRAS 16293−2422, a solar-type low-mass protostar, is also available in the Herschel Science Archive. This spectrum can extend analyses from ground-based studies (e.g., Schöier et al. 2002; Caux et al. 2011; Wampfler et al. 2014; Jørgensen et al. 2016) and unlock the molecular content of IRAS 16293−2422's envelope, especially in its warm inner regions.

In this project, our goal is to study the distribution of nitrogen among different organic molecules, and to compare the protostellar abundance of HCN, the simplest nitrogen-bearing organic, to nitrogenic abundances in comets relative to water. In Section 2.4, we introduce the observations and data used in this work, which consist of *Herschel* observations towards Orion KL and IRAS 16293−2422. In Section 2.5, we give an accounting of the nitrogen-bearing organic molecules in the Orion KL Hot Core. In Section 2.6, we report on our analysis of *Herschel* HIFI data towards IRAS 16293−2422, and present our derivation of the HCN radial abundance distribution as inferred from a spherically symmetric model. We discuss our results in Section 2.7 in the context of cometary nitrogen abundances, and consider the available evidence pertaining to comets, meteorites, interstellar dust, and interstellar ices. We present our conclusions in Section 2.8.

## 2.4 Data and Observations

We have analyzed the results of Herschel observations towards the protostellar environments of Orion KL and IRAS 16293−2422 (henceforth IRAS 16293). Each of these Herschel observations made use of the Heterodyne Instrument for the Far-Infrared (HIFI) spectrograph, and included a spectral survey with large ($\sim$ 1 THz) bandwidth, fine resolution, and high sensitivity. These observations are part of the HEXOS (Herschel Observations of EXtra-Ordinary Sources; Bergin et al., 2010) and CHESS (Chemical HErschel Surveys of Star forming regions; Ceccarelli et al., 2010) large programs. Additional ground-based observations of IRAS 16293 from Wampfler

et al. (2014) and from the TIMASSS program (Caux et al., 2011) complement the HIFI data in our analysis.

**Orion KL** —

We use observations of Orion KL from the HEXOS program (Bergin et al., 2010); these observations and their reduction were described in detail in Crockett et al. (2014b). The dataset consists of a ∼1.2 THz-wide spectrum from 480 to 1907 GHz at a resolution of 1.1 MHz. These data were previously presented and analyzed in Crockett et al. (2010); Wang et al. (2011); Plume et al. (2012); Neill et al. (2013a,b), and Crockett et al. (2014a,b, 2015). In this paper, we primarily analyze the molecular abundances of the Orion KL Hot Core presented in Crockett et al. (2014b) and Neill et al. (2013b); we additionally use results from the 1.3 cm survey of Orion KL by Gong et al. (2015).

**IRAS 16293−2422** —

We have freshly reduced and analyzed the HIFI observations of IRAS 16293 from the CHESS program (Ceccarelli et al., 2010). This spectrum spans 0.9 THz from 480–1800 GHz, with gaps, and again has a spectral resolution of 1.1 MHz. These data were previously presented and analyzed in Hily-Blant et al. (2010); Bacmann et al. (2010), and Coutens et al. (2012). We obtained the *Herschel* HIFI spectra of IRAS 16293 from the Herschel Science Archive (`http://archives.esac.esa.int/hsa/whsa/`) and downloaded the Level 2.5 products. We averaged the horizontal and vertical polarizations in GILDAS/CLASS to improve the signal-to-noise. Finally, we resampled all lines to a common velocity resolution of 0.7 km $s^{-1}$, the resolution of the lowest-$J$ line, in order to achieve consistency between lines and improve the per-channel signal-to-noise.

We have complemented our HIFI data of IRAS 16293 with two sets of ground-based data covering lower-energy transitions. We have used observations of IRAS 16293 at 260 and 345 GHz from the Atacama Pathfinder EXperiment (APEX) 12-meter

telescope in Chile. These APEX data were previously presented in Wampfler et al. (2014), where a detailed description of these data appears. Finally, for the 86 GHz $J = 1-0$ transition of $H^{13}CN$, we have used the publicly available reduced TIMASSS data (Caux et al., 2011).

## 2.5 Nitrogen-bearing molecules in the Orion KL Hot Core

### 2.5.1 Background

Crockett et al. (2014b) analyzed the HEXOS spectra of Orion KL and identified $\sim 13,000$ lines coming from 39 molecules (79 distinct isotopologues). This study made use of IRAM-30m data (80-280 GHz) to constrain low-energy molecular transitions, and of an ALMA interferometric spectral survey at 214-247 GHz to constrain both the millimeter spectrum and the spatial structure of the continuum and molecular emission. Spatial information is especially important due to the multiple physical components within Orion KL which are not spatially resolved by *Herschel*. Crockett et al. present ALMA maps of various molecules, indicating that, e.g., $CH_3CN$ and $CH_3OH$, fill the Hot Core's spatial extent as traced by its continuum emission.

Crockett et al. modeled the emission from each component individually. Temperature gradients within the Hot Core were approximated using the following approach: A single $10''$ component was fit to the emission of each molecule. If a single-temperature component was not sufficient to reproduce the observed emission, then additional subcomponents were added, either larger and cooler or smaller and hotter, in size steps of factor two. Crockett et al. use two modeling codes: a local thermodynamic equilibrium (LTE) code called XCLASS, and a non-LTE, large velocity gradient (LVG) code called MADEX (Cernicharo, 2012). These emission modeling codes were used to derive column densities and abundances for all observed species. The water abundances, in particular, were derived by Neill et al. (2013b). Among

the physical components of Orion KL, we have focused on the Hot Core as the most relevant astrochemical environment in which ices are evaporating, revealing the total molecular budget available at this stage of star and planet formation; in the other regions, many molecules which are important to planetesimal formation are hidden in ices.

Additional abundances of nitrogen-bearing organics in Orion KL are available in the recent literature. Formamide ($NH_2CHO$) was measured by Adande et al. (2013) towards Orion KL with an abundance of $5 \times 10^{-11}$, but because the Hot Core was not spatially or kinematically resolved in their measurement, we omit formamide from our analysis. Crockett et al. (2014b) identified $NH_2CHO$ emission only towards the compact ridge of Orion KL, and not the Hot Core, further justifying this exclusion. In any case, its abundance appears to be far below that of HCN. Another N-bearing organic, methyl isocyanate ($CH_3NCO$), was measured in Orion KL by Cernicharo et al. (2016), who identified abundances towards distinct spatial positions within Orion KL. They measured the $CH_3NCO$ abundance (relative to $H_2O$) towards a position colocated with the Hot Core. By scaling the fractional abundance of $CH_3NCO$ relative to HCN and $CH_3CN$ found by Cernicharo et al. (2016) to the abundances of HCN and $CH_3CN$ in the Orion KL Hot Core found by Crockett et al. (2014b), we estimate the $CH_3NCO$ abundance relative to $H_2$ in the Hot Core to be in the range $3 \times 10^{-9} - 1 \times 10^{-8}$.

The cyanide radical (CN) is a common molecule in the cool and relatively less-dense molecular ISM, but is not abundant in the Orion KL Hot Core. CN is destroyed rapidly in hot cores via reactions with $H_2$, oxygen (O and $O_2$), and simple hydrocarbons such as $C_2H_2$ and $C_2H_4$ (Tielens & Charnley, 2013; Whittet, 2013). Accordingly, CN is not detected by Crockett et al. (2014b) in either the Hot Core or the compact ridge; they find it only towards the plateau and extended ridge regions of Orion KL, where its low rotation temperature of $\sim 20 - 40$ K indicates that CN emission probes

cool material.

Ammonia ($NH_3$) is another nitrogen carrier of interest. Crockett et al. (2014b) were unable to derive an abundance of $NH_3$ towards Orion KL as the *Herschel* survey did not detect lines spanning a sufficiently large upper-state energy coverage to constrain the abundance and excitation state of the gas. $NH_3$ was studied observationally towards Orion KL by Gong et al. (2015), who performed a 1.3 cm line survey of the region with the Effelsberg-100 m telescope; their results are noted below alongside those of Crockett et al. (2014b).

### 2.5.2 Analysis

In order to study the composition of nitrogen-bearing organic (C-containing) molecules, we have analyzed the molecular abundances presented by Crockett et al. (2014b). To do this, we isolated the abundances ($N(\mathrm{X})/N_{\mathrm{H_2}}$, where $N$ represents a column density in $\mathrm{cm}^{-2}$) of all compounds containing both carbon and nitrogen from Table 8 of Crockett et al. (2014b). We calculate the total amount of organic nitrogen by adding all N atoms contained in organic molecules[1]. Each molecule's fraction of organic nitrogen corresponds to the number of N atoms contained in that molecule, divided by the sum of N in organics. Crockett et al. (2014b) estimate that individual column density measurements have an uncertainty of 25%. We estimate uncertainties on the relative abundances to be 35%, by taking each molecule's column density uncertainty to be independent and adding their uncertainties in quadrature. For $CH_3NCO$, we assign an additional $\sim$50% uncertainty on the higher and lower ends of the abundance range scaled from the measurements in Cernicharo et al. (2016), by adding in quadrature the relative errors on column densities in their measurements to those in Crockett et al. (2014b); this accounts for the differences in observing setups.

[1]In principle, molecules with multiple nitrogen atoms would count multiply to this total, in proportion to the number of N atoms they possessed; however, all N-bearing organics in this table have just one N atom, so this sum is identical to the amount of N-bearing organic molecules.

We show the distribution of N atoms among organic species in Figure 2.1, on a logarithmic percentage scale with appropriate error bars (left) and in a linear pie-chart form (right).

### 2.5.3 Results

The total abundance (relative to $H_2$) of N atoms in organic (C-containing) molecules in Orion KL Hot Core is $8.6 \pm 3.4 \times 10^{-7}$. HCN, with an abundance of $X(\mathrm{HCN}) = 6.4 \pm 2.5 \times 10^{-7}$, is the most abundant N-bearing organic, containing $74^{+5}_{-9}\%$ of all N atoms that are in organic molecules. The next most abundant species are $C_2H_5CN$ (ethyl cyanide), with abundance $8.9 \pm 3.5 \times 10^{-8}$, containing $10 \pm 3\%$ of N atoms within organic molecules; HNCO (isocyanic acid), with abundance $7.8 \pm 3.1 \times 10^{-8}$, containing $9 \pm 3\%$ of organic N atoms; and $CH_3CN$ (methyl cyanide), with abundance $3.0 \pm 1.2 \times 10^{-8}$, containing $3 \pm 1\%$ of organic N atoms. The remaining observed species ($C_2H_3CN$, $HC_3N$, $CH_3NCO$, $CH_2NH$, and HNC) each constitute $\lesssim 1\%$ of the nitrogen budget among organic molecules. Therefore, HCN accounts for more than two-thirds of the organic N budget.

Some abundant N-bearing non-organic species are excluded from the above analysis but have known abundances. As noted above, $NH_3$ was observed by Gong et al. (2015). Their measurements of many $NH_3$, $^{15}NH_3$, and $NH_2D$ lines suggest an $NH_3$ abundance in the range $0.8 - 6 \times 10^{-6}$. This range indicates that the $NH_3$ abundance is at least equal to, and possibly an order of magnitude higher than, the abundance of HCN in the Orion KL Hot Core. The NO abundance derived by Crockett et al. (2014b) is $5.5 \times 10^{-7}$, which is consistent (within the errors) with the HCN abundance. Also, Crockett et al. (2014b) derive an NS abundance of $6.8 \times 10^{-9}$.

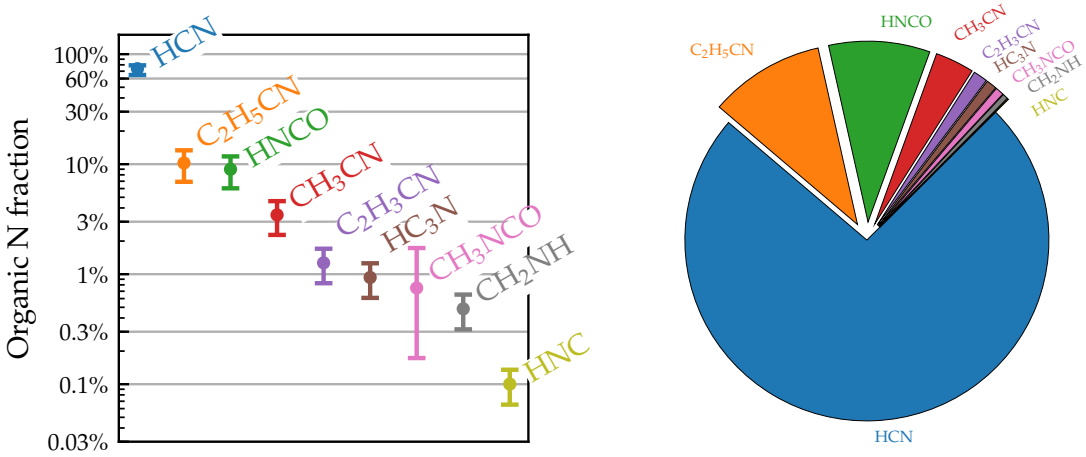


Figure 2.1 Accounting of organic nitrogen-bearing molecules in Orion KL Hot Core, from abundances presented in Crockett et al. (2014b) and (for $CH_3NCO$) Cernicharo et al. (2016). Left: Fraction of total nitrogen found in organic species, per molecule. Right: Pie chart of the mean fraction for each species. The larger errors for $CH_3NCO$ are described in the text.

### 2.5.4 Limitations, caveats, and comments of hot core analysis

The abundance measurements of Crockett et al. (2014b) depend on the accuracy of the $H_2$ column density measured in Plume et al. (2012), which was itself scaled from an empirical measurement of $C^{18}O$ column density using an $H_2$:$C^{18}O$ ratio of $5 \times 10^6$; therefore, any issues in CO:$H_2$ scaling would complicate the abundance measurements. The molecular column densities derived for the Orion KL Hot Core observed by *Herschel*, as presented in Crockett et al. (2014b), depend on assumed source sizes. For Orion KL, Crockett et al. (2014b) and Plume et al. (2012) assume the same source size for the Hot Core, so any errors should cancel out.

One issue that may complicate the interpretation of the *Herschel* molecular abundance inventories is the following ambiguity. As noted in Crockett et al. (2015), there are two ways to account for the increased abundances of many molecules in the Orion KL Hot Core:

1. Grain surface chemistry at cold temperatures that produces icy molecules which are then sublimated (and thus revealed) by the high-temperature environment

of the hot core; or

2. Hot gas chemistry that produces gas molecules in-situ, which only operates in the hot environment.

Our interpretation assumes that the observed molecular populations are dominated by molecules which are formed under the cold conditions of option (1) and are simply *revealed* by the hot environment, as opposed to molecules which *form* due to the hot environment. Crockett et al. (2015) suggested two ways to probe this further. First, to look for spatial gradients in the D/H ratios of complex N-bearing species, as this would be a sign of grain surface chemistry. Second: in the scenario in which the N-bearing organics are desorbing at higher temperatures than O-bearing organics, rather than forming in the hot gas itself, we would expect to see that the emission from N-bearing species is clumpier and has a higher excitation temperature on average.

Among nitrogen-bearing organics, Crockett et al. (2014b) modeled $CH_3CN$, HCN, and HNC with both the XCLASS (simple LTE) and MADEX (non-LTE, large velocity gradient) molecular line spectra modeling codes. The abundances derived for $CH_3CN$ are identical using both methods; compared to XCLASS, the HCN abundance from MADEX is a factor 1.7× higher; and the HNC abundance from MADEX is a factor 6.3× lower. The MADEX modeling is thought to yield more accurate abundances, as it is more sophisticated and can account for both temperature and density gradients, so we preferentially show MADEX results where possible. We note that our results do not change substantially when only XCLASS abundances are used.

Regardless of the above caveats and limitations on the absolute abundance measurements, our results clearly indicate that in a relative comparison, HCN is the dominant N-bearing organic molecule in the Orion KL Hot Core.

## 2.6 The HCN abundance of IRAS 16293−2422

While our analysis of Orion KL is valuable especially due to its rich available spectrum, Orion KL has a higher mass than the region in which the Sun formed, and there may be chemical differences between a high-mass hot core and the birth environment of our Sun. To attempt to control for this difference, we have also studied the low-mass protostar IRAS 16293. IRAS 16293 is a low-mass protostar benchmark, and is among the brightest low-mass protostellar sources in molecular line emission (see Jørgensen et al. 2016 for an extended review of the literature on this source). Motivated by the high abundance of HCN among organic N-bearing molecules towards Orion KL, we have measured the HCN content towards IRAS 16293. In this measurement, we have made use of the ground-based measurements of low-$J$ states presented in Caux et al. (2011) and Wampfler et al. (2014), and space-based high-$J$ states from *Herschel* (Ceccarelli et al., 2010). We have fit a spherically symmetric "jump abundance" model to the observed HCN lines, in order to derive the HCN abundance within and outside the warm sublimation zone.

### 2.6.1 Background

IRAS 16293 is a prototypical Class 0 protostellar system which has been well-characterized physically and chemically. It lies at a distance of $\sim$ 120 pc (Loinard et al., 2008) and has a luminosity of $21 \pm 5$ $L_\odot$ (Jørgensen et al., 2016). It is a protobinary, with two major components (*IRAS16293A* and *IRAS16293B*) that have a separation of $5.1''$ or $\sim$ 620 AU (Looney et al., 2000; Jørgensen et al., 2016). IRAS16293A is itself a possible tight binary with separation $1''$ (Chandler et al., 2005). IRAS 16293 is notable for its rich molecular line spectrum (van Dishoeck et al., 1995; Cazaux et al., 2003) and has been the target of numerous single-dish and interferometric studies, most recently the ALMA-PILS survey (Jørgensen et al., 2016; Lykke et al., 2017; Lig-

terink et al., 2017a). Combined interferometric and single-dish imaging of HCN and $HC^{15}N$ lines was presented by Takakuwa et al. (2007). Within this system, an inner "hot corino" of $\gtrsim$ 100 K gas enriched with evaporated ices is thought to be present, in order to explain molecular abundance jumps and rich organic chemistry (Schöier et al., 2002; Cazaux et al., 2003). Consequently, it is an excellent low-mass protostellar astrochemical benchmark, especially for our interest in studying icy nitrogen materials provided to early planetesimals.

The nitrogen-bearing organics in the hot corino of IRAS 16293 are not as well-constrained as those in Orion KL, so it is difficult to quantify whether nitrogen has major chemical differences in IRAS 16293 versus Orion KL. Nonetheless, unpublished and recently-published results on column densities of nitriles ($-C\equiv N$-bearing organics) are consistent with HCN containing the majority of N in organics in IRAS 16293. Using the PILS data, Calcutt et al. (2018a,c) studied complex nitriles in IRAS 16293 including $CH_3CN$, $C_2H_5CN$, $C_2H_3CN$, $HC_3N$, and $CH_3NC$. Of these, $CH_3CN$ is by far the most abundant; it is an order of magnitude more abundant than the next most abundant species, $C_2H_5CN$. PILS measurements of HCN and its isotopologues are still unpublished; an analysis of the optically-thick (on 0.″5 scales) $HC^{15}N$ $4-3$ line at 344.2 GHz indicates that $HC^{15}N$ is at least 1.6× as abundant as $CH_3C^{15}N$, and therefore (assuming that $^{15}N$ fractionation is comparable between HCN and $CH_3CN$) that HCN is at least 1.6× as abundant as $CH_3CN$, and therefore the dominant organic N carrier in IRAS 16293.

### 2.6.2 Herschel Data Reduction

We fit lines of HCN, $H^{13}CN$ and $HC^{15}N$ from $J = 6-5$ to $10-9$ with Gaussian profiles[2]. Because some of the $H^{13}CN$ and $HC^{15}N$ lines are quite weak, we have used the line widths and velocity centers of the corresponding HCN lines for either (a)

[2]We note that the $HC^{15}N$ $7-6$ line is blended with a stronger adjacent SO $J = 14-13$ line at 602.292 GHz; we fit the two lines simultaneously.

Table 2.1. Lines of $H^{13}CN$ used to fit model.

| Line | Eup (K) | Freq (GHz) | Telescope | Pointing offset | Beamsize HPBW (″) |
|---|---|---|---|---|---|
| $1-0$ | 4.1 | 86.340 | IRAM | 5.0 | 29.1 |
| $3-2$ | 24.9 | 259.012 | APEX | 0.0 | 24.3 |
| $4-3$ | 41.4 | 345.340 | APEX | 0.0 | 18.2 |
| $6-5$ | 87.0 | 517.970 | HIFI | 2.5 | 41.6 |
| $7-6$ | 116.0 | 604.268 | HIFI | 2.5 | 35.7 |
| $8-7$ | 149.2 | 690.552 | HIFI | 2.5 | 31.2 |
| $9-8$ | 186.4 | 776.820 | HIFI | 2.5 | 27.7 |
| $10-9$ | 227.9 | 863.071 | HIFI | 2.5 | 25.0 |
| $11-10$ | 273.4 | 949.301 | HIFI | 2.5 | 22.7 |

[a]Pointing offsets from source A are described in Caux et al. (2011) for the IRAM data, Wampfler et al. (2014) for the APEX data, and Coutens et al. (2012) for the HIFI data.

Note. — Gaussian fits to these lines, and their HCN and $HC^{15}N$ counterparts, appear in Table A.1 in Appendix A.

an initial guess for the Gaussian fit, or (b) a fixed parameter such that only the line intensity was allowed to float in the fit, depending on the strength of the lower-intensity line. Results of this fitting are presented in Appendix A; Figure A.1 shows the lines and their Gaussian fits, and the fitted line parameters are presented in Table A.1.

We have estimated the optical depths from the flux ratios between the standard isotopologue HCN and its rarer isotopologue $H^{13}CN$. By assuming an isotopic ratio between HCN and $H^{13}CN$, we can relate the optical depth of a given rarer isotopologue in the following way (as described by Crockett et al. 2014a):

$$\tau_{\rm iso} = -\ln\left(1 - \frac{T_{\rm iso}}{T_{\rm main}}\right) \tag{2.1}$$

and

$$\tau_{\rm main} = \tau_{\rm iso} \cdot \left(\frac{^{12}{\rm C}}{^{13}{\rm C}}\right). \tag{2.2}$$

In these equations, $T_{\rm main}$ and $T_{\rm iso}$ denote the peak brightness temperatures of the main and rarer isotopologue lines, respectively, and $\tau_{\rm main}$ and $\tau_{\rm iso}$ likewise denote those lines' optical depths. This equation assumes that $\tau_{\rm main} \gg \tau_{\rm iso}$, which is appropriate

for comparing $^{12}$C with $^{13}$C. We adopt a carbon isotopic ratio of $^{12}C/^{13}C = 69 \pm 6$ in the local ISM (Wilson, 1999). The optical depths $\tau$ are given in Table A.2. We found optical depths $\tau_{H^{13}CN} = 0.08 - 0.24$ (corresponding to $\tau_{HCN} = 5.9 - 16.5$). Therefore, we can confirm that none of the H$^{13}$CN lines is optically thick.

### 2.6.3 Nitrogen Isotopic Fractionation

Nitrogen isotopic fractionation seen in a low-mass protostellar system such as IRAS 16293 can be compared to the nitrogen fractionation measured in solar system objects such as meteorites and comets (Hily-Blant et al., 2013; Füri & Marty, 2015). By assuming that H$^{13}$CN and HC$^{15}$N have the same excitation properties in IRAS 16293, and with knowledge (from the HCN lines) that the observed H$^{13}$CN and HC$^{15}$N lines are all optically thin ($\tau \lesssim 0.25$), we can calculate the $^{14}N/^{15}N$ ratio for each rotational state of HCN independently. In the *Herschel* data, the following lines have definite detections for both H$^{13}$CN and HC$^{15}$N: $6-5$, $7-6$, $8-7$, and $9-8$. We find the $^{14}N/^{15}N$ ratio in each line to be $119 \pm 13$, $155 \pm 43$, $151 \pm 89$, and $210 \pm 70$ respectively. In all cases, these are $^{15}$N-enriched relative to the local ISM $^{14}N/^{15}N$ ratio of $388 \pm 38$ and the solar standard of 270 (Wilson, 1999). These results are broadly consistent with the $^{14}N/^{15}N$ ratios measured by Wampfler et al. (2014) for this source, in which the $4-3$ and $3-2$ lines had $190 \pm 38$ and $163 \pm 20$, respectively. The weighted mean of the $^{14}N/^{15}N$ values is $140 \pm 10$.

### 2.6.4 Model

In order to derive the HCN abundance profile around IRAS 16293, we have used spherically symmetric models of the temperature, density, and molecular abundance in order to produce model spectra and compare them with the observed emission from H$^{13}$CN. We focus on this isotopologue, which has a much lower abundance than HCN and therefore fewer issues with optical depth. Aspects of this model fitting are

similar to the approach carried out by Coutens et al. (2012), who use the physical model of IRAS 16293 derived in Crimier et al. (2010). We choose this modeling approach to derive the HCN abundance in a way that is consistent with the previous $H_2O$ abundance modeling performed by Coutens et al. (2012). This facilitates direct comparison of these results and yield HCN/$H_2O$ ratios, though as noted by Visser et al. 2013 and further discussed in Section 2.7.1, the Coutens et al. water abundance of $5 \times 10^{-6}$ is possibly only a lower limit, with theoretical and observational support for a value closer to $10^{-4}$.

We use a model which has two regions of constant HCN abundance: an outer "cold" region with a low gas-phase HCN abundance (because most HCN is frozen onto dust grains), and an inner "warm" region with a high gas-phase HCN abundance due to sublimation of HCN from those grains. This "jump abundance" model has three free parameters: The inner abundance ($X_{\rm in}$), the outer abundance ($X_{\rm out}$), and the temperature at which sublimation rapidly occurs ($T_{\rm jump}$). Jump abundance models have been adopted to interpret observations of protostars in many papers (e.g., Schöier et al. 2002; Maret et al. 2004; Parise et al. 2005; Brinch et al. 2009b; Coutens et al. 2012). The sublimation rate of molecular ices depends exponentially on the local temperature, so a step-function is an appropriate way to model the very steep increase that occurs in gas-phase molecular abundances at specific radii (Rodgers & Charnley, 2003; Jørgensen et al., 2005c).

We present the parameters used in this model in Table 2.2. To enable direct comparison with Coutens et al. (2012), who derived the $H_2O$ abundance using a very similar set of data and methods, we adopt the one-dimensional physical model developed by Crimier et al. (2010). This physical model incorporates (a) submillimeter single-dish emission profiles at 350, 450, and 850 $\mu$m, and (b) the spectral energy distribution (SED) from 23 to 1300 $\mu$m. Crimier et al. (2010) present a model of the density and temperature structure which follows a Shu "inside-out" collapsing enve-

Table 2.2. Parameters for $H^{13}CN$ emission model of IRAS 16293−2422

| Fixed parameters | | |
|---|---|---|
| $L_*$ ($L_\odot$) | 22 | |
| $D$ (pc) | 120 | |
| $r_{\rm min}$ (AU) | 22 | |
| $r_{\rm max}$ (AU) | 6100 | |
| $r_{\rm infall}$ (AU) | 1280 | |
| $\rho$ power law index | $-1.5$ | ($r < r_{\rm infall}$) |
| | $-2$ | ($r > r_{\rm infall}$) |
| $M_{\rm env}$ ($M_\odot$) | 1.9 | |
| $M_*$ ($M_\odot$) | 1.0 | |

| Floating parameters | Best-fit ($\pm$) | Allowed Range |
|---|---|---|
| $X_{\rm in}$ ($H^{13}CN$) | $8.51^{+0.81}_{-0.74} \times 10^{-10}$ | $10^{-12} - 10^{-8}$ |
| $X_{\rm out}$ ($H^{13}CN$) | $1.82^{+0.09}_{-0.09} \times 10^{-11}$ | $10^{-14} - X_{\rm in}$ |
| $T_{\rm jump}$ (K) | $71.2^{+2.4}_{-2.6}$ | $30 - 120$ |

| MCMC parameters | |
|---|---|
| # walkers | 24 |
| # steps | 1776 |
| Autocorrelation time $\tau$ | 34.7 |
| # steps / $\tau$ | 51.2 |

Note. — We adopt fixed physical parameters for our IRAS 16293 model following Crimier et al. (2010) and Coutens et al. (2012).

lope (Shu, 1977; Adams & Shu, 1986), in which the density follows two power laws: $\rho \propto r^{-1.5}$ for $r < r_{\rm infall}$, and $\rho \propto r^{-2}$ for $r > r_{\rm infall}$. Three-dimensional models of the physical structure of IRAS 16293 are under development (e.g., Jacobsen et al. 2017, who model the envelope, disks and dust filament), but for the purposes of this paper, a 1D model is sufficient to derive bulk abundance properties.

In our modeling, we start with the luminosity and density distributions listed in Table 2.2, and first solve for the temperature structure using the radiative transfer code TRANSPHERE (Dullemond et al., 2002)[3]. Following Coutens et al. (2012), we use RATRAN (Hogerheijde & van der Tak, 2000b,a; van der Tak & Hogerheijde, 2007), a spherical Monte Carlo 1D radiative transfer code: RATRAN solves the line radiative problem by iteratively computing the mean radiation field $J_\nu$ in each radial

[3]The TRANSPHERE Fortran code is hosted online at `http://www.ita.uni-heidelberg.de/~dullemond/software/transphere/index.shtml`

shell to derive the level populations of $H^{13}CN$. The HCN collision rate coefficients were derived by Dumouchel et al. (2010) with He as the collision partner. The rates were retrieved in a molecular data file from the LAMDA database[4] (Schöier et al., 2005), where they were scaled by a factor 1.37 to represent collisions with $H_2$. Like Coutens et al. (2012), we use an infalling radial velocity field $v_r = \sqrt{2GM/r}$ for a 1 $M_\odot$ central star; outside of the infall radius $r_{\rm infall}$, the envelope is assumed to be static (i.e., $v_r = 0$). The output of RATRAN is a datacube (dimensions R.A., Decl., and radial velocity) of molecular line emission for each emission line under consideration.

To synthesize the observed single-dish spectra, we use the MIRIAD software package (Sault et al., 1995) to appropriately extract information from the RATRAN-produced datacubes. By convolving with the telescope beam profile at each frequency, and extracting the emission corresponding to the appropriate pointing offset, we produce synthetic spectra that are faithful to what would be observed with the given observational setup. In this step, we carefully observe the different offset pointings of the ground-based TIMASSS data (pointed at IRAS 16293B, located 5″ from source A), the APEX data (pointed directly at source A), and the *Herschel* data (pointed halfway between sources A and B, i.e., 2.5″ from source A). Following Coutens et al. (2012), we assume that our spherical model is centered on source A, the more massive of the two components. Finally, we resample the synthetic spectra to the velocity sampling of the observed data.[5]

[4] `http://home.strw.leidenuniv.nl/~moldata/`

[5] RATRAN does not produce hyperfine structure for the $J = 1 - 0$ line, as collisional rates for the separate hyperfine states of the $J = 1 - 0$ line of $H^{13}CN$ are not available. Therefore, we simulate the hyperfine structure of the $J = 1 - 0$ line by distributing the total flux of the $1 - 0$ line among the three hyperfine states according to their expected flux ratios. This would be inappropriate if the $H^{13}CN$ $J = 1 - 0$ line were highly optically thick, but as the emprical flux ratios of the hyperfine components are very near the ideal LTE case of 1:5:3, this is a reasonable approach.

### 2.6.5 Fitting

Our model fitting procedure uses a Markov chain Monte Carlo (MCMC) method. The specific MCMC implementation we use is the "emcee" package (Foreman-Mackey et al., 2013a,b), a Python implementation of the affine-invariant MCMC sampler proposed by Goodman & Weare (2010). The advantage of this MCMC approach is that it yields a posterior probability distribution of model parameters from which we can estimate uncertainties in the best-fit model parameters. A review of Markov Chain Monte Carlo techniques and their use in astrophysics has been recently presented by Hogg & Foreman-Mackey (2018).

To compare the observed data to the model spectra, we compute the following $\chi^2$ statistic for each set of model parameters $X_{\rm in}$, $X_{\rm out}$, $T_{\rm jump}$:

$$\chi^2 = \sum_{i=1}^{N} \sum_{j=1}^{n_{\rm chan}} \frac{\left(T_{{\rm data},i,j} - T_{{\rm model},i,j}\right)^2}{{\rm rms}_i^2 + \left(Cal_i \times T_{{\rm data},i,j}\right)^2} \tag{2.3}$$

for $N$ lines (each designated $i$), $n_{\rm chan}$ channels per line (each designated $j$). The observed intensity in channel $j$ of line $i$ of the data and model is designated $T_{{\rm data},i,j}$ and $T_{{\rm model},i,j}$, respectively. The per-channel rms for each line $i$ is designated ${\rm rms}_i$. The calibration uncertainty, denoted $Cal_i$, is fixed at 15% for each line.

For the MCMC run, the corresponding log-likelihood function $\ln \mathscr{L}$ is written as:

$$\ln \mathscr{L} = K - \frac{1}{2}\chi^2 \tag{2.4}$$

which is maximized in the MCMC fitting procedure.[6] We constrain the model parameters (via "flat" priors) to the following ranges: $X_{\rm in} : 10^{-12} - 10^{-8}$, $X_{\rm out} : 10^{-14} - X_{\rm in}$, and $T_{\rm jump} : 30 - 120$ K.

[6] As these models are highly nonlinear, we refrain from computing or reporting "reduced chi-squared" values for these model fits, following Andrae et al. (2010).

We ran the MCMC sampler with an ensemble of 24 walkers for 1776 steps.[7] Foreman-Mackey et al. (2013a) discuss ways to assess the robustness of an MCMC run, and recommend:

1. that the "acceptance fraction" fall between $0.2 - 0.5$,

2. that the autocorrelation time $\tau$ be much less than the number of ensemble steps.

We find the mean acceptance fraction for each of the walkers to be 0.633, which is slightly higher than the ideal range, but not enough to raise concern. The maximum autocorrelation time $\tau$ among the three parameters was 34.7 steps; thus, we ran the MCMC chains for a factor $51\times$ longer than $\tau$, indicating that this MCMC run has successfully converged. Finally, we have discarded the first 69 steps (i.e., $2 \times \tau$) of the MCMC chains as "burn-in," to ensure that the initial walker positions do not have an effect on the results presented below.

### 2.6.6 Results of model fitting

We present the following "best-fit" (i.e. median) parameters for the posterior probability distribution of the $H^{13}CN$ emission model:

$$\begin{aligned} X_{\rm in}(H^{13}CN) &= \left(8.51^{+0.81}_{-0.74}\right) \times 10^{-10} \\ X_{\rm out}(H^{13}CN) &= \left(1.82^{+0.09}_{-0.09}\right) \times 10^{-11} \\ T_{\rm jump} &= 71.2^{+2.4}_{-2.6}\ {\rm K} \end{aligned}$$

and our best-fit model is shown in Figure 2.2, overplotted on the data from TIMASSS, APEX, and *Herschel*. Our quoted uncertainties are drawn from the 16th, 50th, and 84th percentile thresholds (i.e., the median value $\pm 34\%$) of the sample distributions on each parameter. (This is roughly analogous to quoting $\pm 1\sigma$ errors from a Gaussian

[7] Using a 2015 model MacBook Pro, this model took roughly 1400 s per MCMC ensemble step; the 1776-step MCMC sampler ran for 690 hours.

distribution.) We show the sample distributions for each model parameter (projected into a "corner plot") in Figure 2.3. From the posterior distributions, it is clear that $X_{\rm in}$ and $T_{\rm jump}$ are somewhat correlated, indicating the importance of varying these two parameters simultaneously, rather than assuming a $T_{\rm jump}$ from the literature. The apparently tight constraints on these parameters likely are due to the wide range of $E_{\rm up}$, from $4 - 273$ K (cf. Table 2.1), sampled in the nine observed lines.

By adopting a $^{12}{\rm C}/^{13}{\rm C}$ ratio of $69 \pm 6$ (Wilson, 1999), and assuming that carbon isotopic fractionation is negligible in HCN, we therefore infer the following HCN abundances:

$$\begin{aligned} X_{\rm in}({\rm HCN}) &= \left(5.87^{+0.72}_{-0.76}\right) \times 10^{-8} \\ X_{\rm out}({\rm HCN}) &= \left(1.26^{+0.13}_{-0.13}\right) \times 10^{-9} \end{aligned}$$

We estimated the uncertainties on these parameters by summing in quadrature the $X({\rm H}^{13}{\rm CN})$ error bars with the uncertainty on the $^{12}{\rm C}/^{13}{\rm C}$ ratio.

### 2.6.7 Comments, limitations, and caveats of IRAS 16293 analysis

The $X_{\rm out}$ which we have derived for the outer envelope closely matches the measurement presented in Schöier et al. (2002). Schöier et al. (2002) use an abundance model, fit to the $J = 4-3$ and $3-2$ lines of HCN and ${\rm H}^{13}{\rm CN}$, to measure $X({\rm H}^{13}{\rm CN}) = 1.8 \times 10^{-11}$. They note that, as they sample only transitions which probe energy states below 90 K, they cannot constrain the existence of a hot core abundance jump for these species, so they limit their analysis to the colder outer envelope. They derive a $X({\rm HCN}) = 1.1 \times 10^{-9}$ (assuming $^{12}{\rm C}/^{13}{\rm C} = 60$). If scaled to our chosen $^{12}{\rm C}/^{13}{\rm C} = 69$ for equivalent comparison, this gives $X({\rm HCN}) = 1.26 \times 10^{-9}$. Their independent measurements of the outer ${\rm H}^{13}{\rm CN}$ and HCN abundances are essentially identical to our measured $X_{\rm out}({\rm H}^{13}{\rm CN}) = \left(1.82^{+0.09}_{-0.09}\right) \times 10^{-11}$, and $X_{\rm out}({\rm HCN}) = \left(1.26^{+0.13}_{-0.13}\right) \times 10^{-9}$.

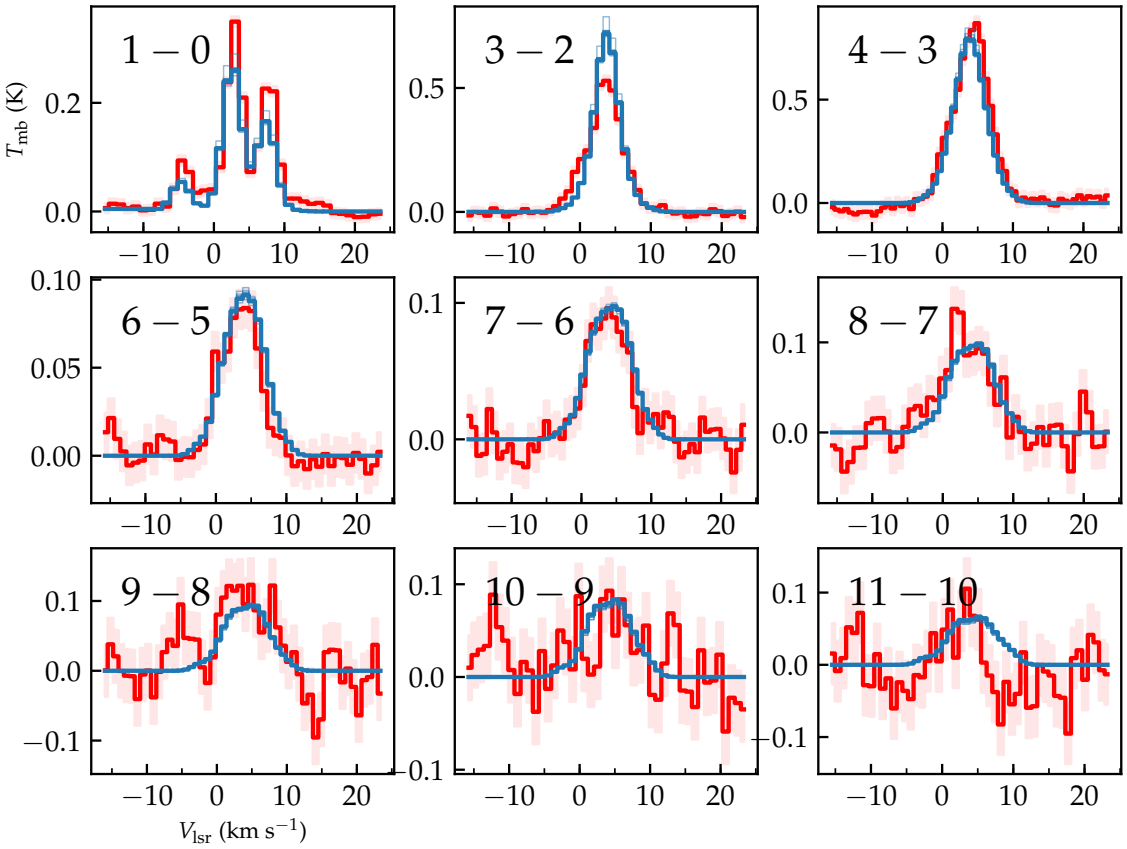


Figure 2.2 Comparison of observed H$^{13}$CN spectra (red, with pink error bars) with ten representative model spectra (light blue lines) drawn from the posterior parameter distribution. The "best-fit" model (i.e., with the median values drawn from each parameter distribution) is shown with the thickest blue line. For most lines, the ten model spectra overlap too closely to distinguish.

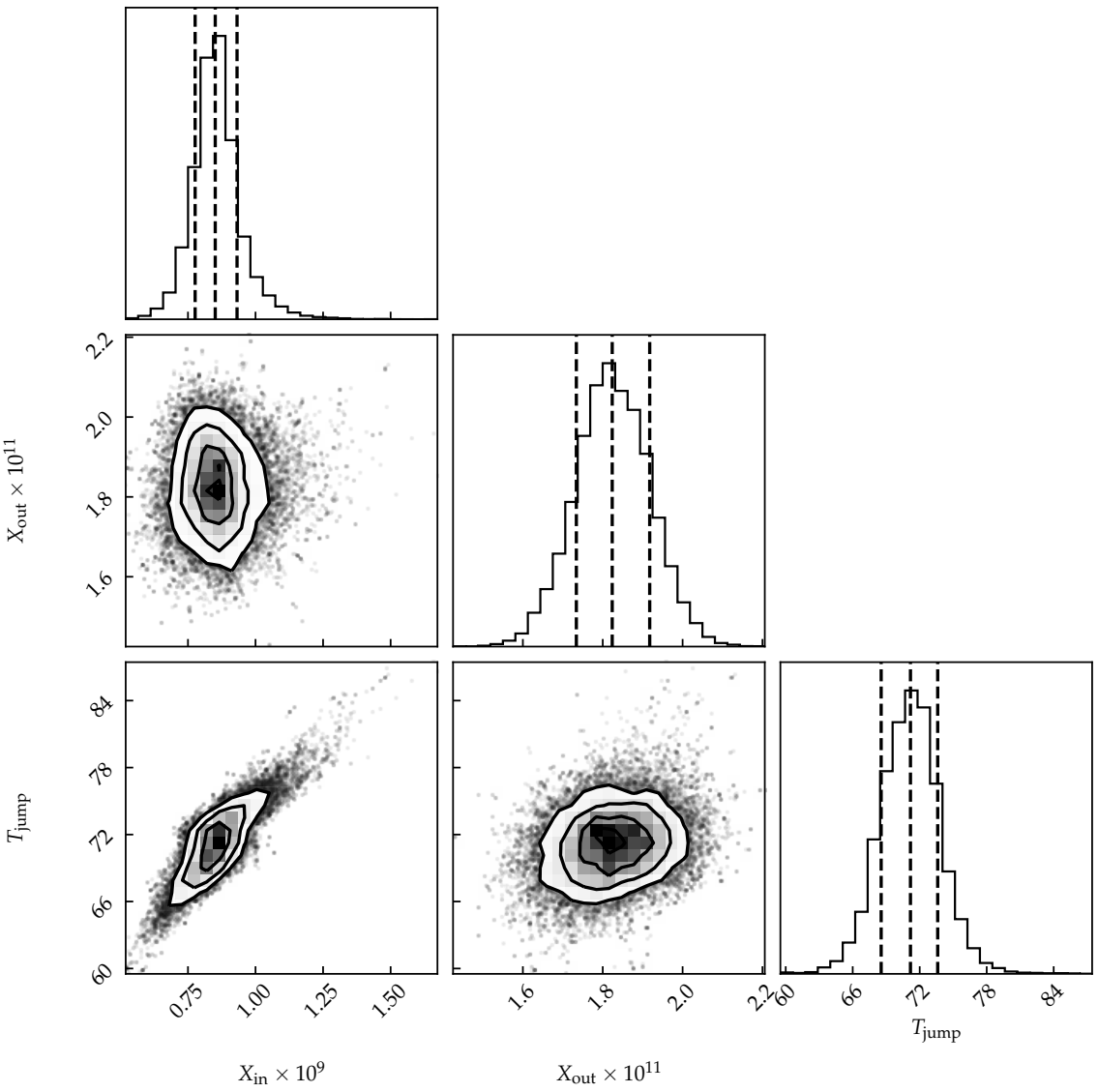


Figure 2.3 Corner plot of the posterior probability distributions projected into one and two dimensions along different parameter axes. Created with "corner.py" (Foreman-Mackey, 2016).

Our analysis, which assumes spherical symmetry of IRAS 16293, has known limitations, but the assumption of spherical symmetry is justifiable for our scientific purposes. Jørgensen et al. (2002, 2005c) discuss how certain systematic effects in protostar models, such as the assumption of spherical symmetry and the uncertainty of assumed dust properties, may cause systematic uncertainties by factors of $2-3$ in absolute abundances. As noted in depth in Jørgensen et al. (2016), IRAS 16293 is a multiple system with a non-trivial morphology on small scales. Because we are only interested in radially averaged bulk properties of the IRAS 16293 system, the spherically symmetric approach that we have taken is sufficient. While there may be systematic issues in the absolute abundance scaling of our HCN measurement, the relative ratios of HCN/$H_2O$ presented in Section 2.7 use $H_2O$ measurements from Coutens et al. (2012) which use the same physical model, allowing some systematic issues to cancel out in the ratio. One additional concern is that the $X(H_2O)$ measurement from Coutens et al. (2012) may only be a lower limit on the water abundance, and that deviation from spherical symmetry on small scales may bias the water abundance measurement from its true value near $10^{-4}$ (Visser et al., 2013). We consider this issue in Section 2.7.1.

We omit the secondary companion, IRAS 16293B, in this model; meanwhile, the ground-based observation of the $J = 1-0$ line from TIMASSS (Caux et al., 2011) is centered on source B. This is not a concern for our analysis, as previous data (especially SMA and ALMA resolved images of HCN from, e.g., Takakuwa et al. 2007; Zapata et al. 2013) reveal that Source A is far brighter in molecular line and continuum emission. For the $1-0$ line, the half-power beam width of $29''$ comprises both sources well; this, combined with the fact that we have properly considered how the flux from source A would be diluted by the pointing offset of $5''$, effectively mitigates any errors that might arise in this analysis.

### 2.6.8 HCN sublimation temperature and binding energy

Our observational coverage of nine $H^{13}CN$ transitions towards IRAS 16293, spanning $4 - 273$ K in upper state energy, removes our need to assume a given $T_{\rm jump}$ and instead allows us to constrain it using the data. In the MCMC posterior distributions shown in Figure 2.3, two results from the $T_{\rm jump}$ posterior probability distribution are apparent: (a) the strong positive correlation between $T_{\rm jump}$ and $X_{\rm in}$, and (b) the relatively tight constraints placed on $T_{\rm jump}$ given our model assumptions and the data. We discuss the consequences of these two results here.

The high positive correlation between $T_{\rm jump}$ and $X_{\rm in}$ (Pearson correlation coefficient $R = 0.82$) is not surprising, as $T_{\rm jump}$ effectively sets the radius of the "jump" abundance zone. For a given column density of high-temperature HCN, a higher $T_{\rm jump}$ (and therefore smaller sublimation region) necessitates a higher density (and therefore abundance) of those hot HCN molecules, and vice versa. Nonetheless, it does speak to the importance of estimating $T_{\rm jump}$ accurately in order to properly measure $X_{\rm in}$. In contrast, neither $X_{\rm in}-X_{\rm out}$ ($R = 0.002$) nor $X_{\rm out}-T_{\rm jump}$ ($R = 0.23$) show meaningful correlation. As $T_{\rm jump}$ and $X_{\rm in}$ are so correlated, a change of only 20 K in the assumed $T_{\rm jump}$ corresponds to a $2\times$ difference in the derived $X_{\rm in}$. Not all observational studies have access to *Herschel* data which constrain so many transitions and energy states of an observed molecule, but when available, using these data to simultaneously constrain $T_{\rm jump}$ alongside the measured abundances offers this significant advantage.

Our measurement of $T_{\rm jump}$ also gives information about the binding of HCN ice onto interstellar dust grains. As noted in Hollenbach et al. (2009), there is a direct connection between the freezing (or sublimation) temperature of a molecule and the value of its binding energy to dust grains. This energy is sometimes referred to as the adsorption or desorption energy, and denoted $E_{\rm B}$, $E_{\rm ads}$, or $E_{\rm D}$. The binding energy of HCN onto dust grains is poorly constrained, as laboratory measurements involving

cyanide molecules (including the temperature programmed desorption experiments used to measure binding energies) are difficult to carry out safely and accurately. Previous estimates of HCN's binding energy range widely: 1760 K (Hasegawa & Herbst, 1993), 1722 K (Bergin et al., 1995), 2050 K (Garrod & Herbst 2006, as listed in the fifth release of the UMIST Database for Astrochemistry, McElroy et al. 2013), $3370-3610$ K (Noble et al., 2013), 4700 K (Szőri & Jedlovszky, 2014), $2460-6974$ K (Bertin et al., 2017), and 3700 K (Wakelam et al. 2017, as listed in KIDA, the Kinetic Database for Astrochemistry, Wakelam et al. 2012). This spread of binding energies corresponds to a $T_{\rm jump}$ range of $30-122$ K under typical conditions.

Our derived $T_{\rm jump}$ allows us to make a prediction for the binding energy of HCN onto astronomical dust grains. By rewriting Equation 5 from Hollenbach et al. (2009), which is itself derived from the Polanyi-Wigner equation (Polanyi & Wigner, 1925), we can express the binding energy in terms of the jump temperature as well as several other terms:

$$\frac{E_{\rm ads}({\rm HCN})}{k} = T_{f,{\rm HCN}} \times \left[57 + \ln\left[\left(\frac{N_{s,{\rm HCN}}}{10^{15}\ {\rm cm}^{-2}}\right)\left(\frac{\nu_{\rm HCN}}{10^{13}\ {\rm s}^{-1}}\right)\left(\frac{1\ {\rm cm}^{-3}}{n_{\rm HCN}}\right)\left(\frac{10^{4}\ {\rm cm\ s}^{-1}}{v_{\rm HCN}}\right)\right]\right] \tag{2.5}$$

with $T_{f,{\rm HCN}}$ standing in for $T_{\rm jump}$, $N_{s,{\rm HCN}}$ the number of adsorption sites per cm$^2$, $n_{\rm HCN}$ the number density of HCN in the gas phase, $v_{\rm HCN}$ its thermal speed. To saturate a single-molecule monolayer of ice, a gas-phase abundance of $\sim 10^{-6}$ relative to $H_2$ is typically needed; as the HCN abundance is roughly an order of magnitude below this, we take $N_{s,{\rm HCN}} = 10^{14}$ cm$^{-2}$, i.e., 10% of available sites. We calculate the vibrational frequency $\nu_{\rm HCN} = 5.27 \times 10^{13}$ s$^{-1}$. At the radius in our model at which $T$=$T_{\rm jump}$, the number density $n_{\rm HCN} = 4.9$ cm$^{-3}$, and the thermal speed $v_{\rm HCN} = 2.37 \times 10^{4}$ cm s$^{-1}$.

We predict a binding energy $E_{\rm ads}({\rm HCN})/k = 3840 \pm 140$ K, given the derived $T_{\rm jump}$= $71.2^{+2.4}_{-2.6}$ K and the physical conditions (density, temperature, and gas-phase HCN abundance) at the corresponding radius in the envelope model. As $E_{\rm ads}$ depends

linearly on $T_{\rm jump}$ but only on the logarithm of the other terms in Equation 2.5, we assume that uncertainties in $T_{\rm jump}$ dominate in contributing to uncertainties in $E_{\rm ads}$.

We note that this modeling experiment was not designed to place firm constraints on the HCN binding energy, and we have not carefully investigated the sensitivity of this prediction on the various model parameters (especially including those which we consider "fixed", such as the stellar luminosity and the physical envelope structure). Careful use of this result should be observed.

## 2.7 Discussion: On the origins of cometary nitrogen

Previous work (e.g. Bergin et al. 2015; Füri & Marty 2015; Alexander et al. 2017) has suggested that refractory carbonaceous grains and molecular ices are the precursors to the nitrogen seen in the Earth's cometary and meteoritic building blocks. In this study we have measured the nitrogen content in organic ices towards protostars at an early stage of planet formation, which offers an opportunity to compare these measurements to a late stage of planet formation. Specifically, we can compare to the ice and refractory contents of solar system comets, which are considered a relatively pristine reservoir of the materials available to the young solar system during planetary assembly (e.g., Charnley & Rodgers 2008). Through this comparison, we can explore whether we can identify (or rule out) the original source(s) of nitrogen provided to these bodies. In this section, we make use of two ratios to explore this topic: the $N/H_2O$ ratio (to trace the bulk nitrogen), and the $^{14}N/^{15}N$ ratio (to discern between different origin populations).

The nature of nitrogen in cometary matter, as revealed by studies of material from comets Halley (Kissel & Krueger, 1987), 81P/Wild 2 (Sandford et al. 2006, and other references compiled in Alexander et al. 2017), and 67P/Churyumov-Gerasimenko (Fray et al., 2016), indicates that the nitrogen-bearing organic and refractory matter in comets has close isotopic and mineralogical similarities to that seen in interplan-

Table 2.3. Comparisons of $N/H_2O$ ratios between protostars, comets, and ISM dust

| | **Protostellar sources**[a] | | **Cometary sources**[b] | **ISM dust**[c] |
|---|---|---|---|---|
| | IRAS 16293 | Orion KL | | |
| $HCN/H_2O$ | $0.05 - 2.0\%$ | $0.10 \pm 0.06$ % | $0.1 - 0.6$ % | ... |
| organic $N/H_2O$ | ... | $0.13 \pm 0.07$ % | $0.1 - 0.9$ % | ... |
| $NH_3/H_2O$ | ... | $0.12 - 0.92$ % | $0.4 - 1.8$ % | ... |
| total N ices | ... | ... | $0.5 - 2.7$ % | ... |
| $N/H_2O$ (dust) | ... | ... | $5 - 24$ % | $\lesssim 19 \pm 12$ % |

Note. — All values given as percentages (%) relative to $H_2O$.

etary dust particles (IDPs) and the insoluble organic matter (IOM) in carbonaceous chondrites (Alexander et al., 2007). Further, these similarities suggest a genetic relationship between chondritic, IDP, and cometary organic matter (Füri & Marty, 2015; Alexander et al., 2017).

### 2.7.1 Bulk nitrogen

Central to this investigation is the question of which primordial sources of nitrogen has a high enough abundance to account for the nitrogen content of solar system planetesimals. Here we consider either molecular ices or refractory dust as these primordial nitrogen reservoirs. To compare the bulk nitrogen content of various bodies (protostars, comets, and interstellar dust), we use water ($H_2O$) as a standard. As the most abundant interstellar and cometary volatile species, $H_2O$ is measurable in all of these systems. Comparing against an $H_2O$ standard allows us to explore the connections among each of these stages. In this work we have identified $N/H_2O$ ratios in protostars, in comets, and in interstellar dust. These are compiled in Table 2.3. While molecular ratios are commonly reported relative to $H_2O$ in cometary ices, this work represents the first use of $N/H_2O$ ratios to trace the bulk nitrogen content across protostars, comets, and interstellar dust.

Water abundances have been measured in these protostellar environments by Neill

et al. (2013b) for Orion KL, and Coutens et al. (2012) for IRAS 16293; in each case, measured using nearly identical data and techniques as those used to derive HCN abundances in this work. We focus our attention on the warm and hot "inner" environments of each protostellar system. As summarized in Table 2.3, the $HCN/H_2O$ abundance in Orion KL is $0.10 \pm 0.06$ %, while all organic N carriers together yield an $N/H_2O$ ratio of $0.13 \pm 0.07$ %. For $NH_3$, the wide abundance range allowed by Gong et al. (2015) gives a range of $NH_3/H_2O$ values of $0.12 - 0.92\%$.

In IRAS 16293, we derive an $HCN/H_2O$ ratio in the inner envelope of $1.2 \pm 0.8\%$ when considering the $H_2O$ abundance from Coutens et al. (2012) at face value. However, water abundances measured in the inner envelopes of protostars may suffer from systematic issues related to the assumption of spherical symmetry, as noted in depth by Visser et al. (2013), who studied $H_2O$ in the Class 0 protostar NGC1333 IRAS2A. Visser et al. find that a spherically symmetric model for the inner 100 AU fails to reproduce the observed emission from many lines, and that a disk or proto-disk is needed to account for the discrepancy; one implication of this geometric modification is a substantially higher water abundance, likely near $10^{-4}$ relative to $H_2$, as predicted by some theoretical studies such as Rodgers & Charnley (2003). The comparison of ALMA data between NGC1333-IRAS2A and IRAS 16293 indicates that IRAS 16293 itself has a 30-times-higher $H_2O$ column density on scales revealed by ALMA (Persson et al., 2013; Visser et al., 2013), indicating that its abundances are also likely affected by this issue. These geometric effects are most severe at the smallest scales, where the sublimation zone of $H_2O$ lies, so $H_2O$ is more affected by this issue than HCN. We therefore consider the warm inner $H_2O$ abundance of IRAS 16293 to be somewhere in the range of $5 \times 10^{-6} - 10^{-4}$; when uncertainties in the HCN abundance are folded in, this yields an $HCN/H_2O$ ratio $0.05 - 2.0\%$, with some preference for the lower end of this range.

The cometary abundances of many molecular species are compiled in Mumma

& Charnley (2011) relative to $H_2O$. The most abundant and second-most-abundant nitrogen-bearing ices in comets are $NH_3$ and HCN, respectively (Mumma & Charnley, 2011). Cometary $NH_3$ ice has an abundance of $\sim 0.4 - 1.8\%$ relative to $H_2O$ ice. HCN, the next largest contributor, has an abundance of $0.1 - 0.6\%$ relative to $H_2O$. Other, less-abundant species sum to at most 0.3%, giving a total N abundance in ices of $0.5 - 2.7\%$. We find that the protostellar abundances for molecular N-bearing ices are of roughly the same order of magnitude as the cometary ice abundances. This suggests that the nitrogen-bearing molecular ices already present on dust grain surfaces in the protostellar stage may be the direct progenitors to the nitrogenic molecular ices found in comets, as suggested previously by numerous other studies (cf. Mumma & Charnley, 2011, and references therein).

Only a small portion of cometary nitrogen is contained in molecular ices, however. Wyckoff et al. (1991) measured the ratio of nitrogen in the dust to gas in Comet 1P/Halley to be 90:10, i.e., only 10% of Halley's nitrogen is in the gas, with the vast majority in dust. Measurements by the Rosetta probe indicate that Comet 67P also has much more N in dust: results from COSAC and Philae (Goesmann et al., 2015; Wright et al., 2015), COSIMA (Fray et al., 2017), and ROSINA (Le Roy et al., 2015) all confirm that the dust of 67P is more N-rich than the gas. Based on these studies of comets Halley and 67P, we therefore estimate the total nitrogen content in the typical comet as compiled by Mumma & Charnley (2011), by multiplying the range of N-ices/$H_2O$ abundances by $10\times$. We estimate that the N/$H_2O$ in dust in comets is $5 - 24\%$, and the bulk N/$H_2O$ ratio in comets is $5 - 27\%$. Therefore, the nitrogen in molecular ices measured in protostars is an order of magnitude or more too low to account for the total nitrogen content of comets.

In principle, the most volatile forms of nitrogen (especially $N_2$) should contain the majority of interstellar nitrogen at the beginning of the planet formation process (see, e.g., Schwarz & Bergin 2014). However, we can exclude these more volatile forms

Table 2.4. Binding energies and sublimation temperatures for simple N-bearing species

| Species | $E_B/k$ (K) | $T_{jump}$ (K) |
|---|---|---|
| N | $720 \pm 216$ | $13 \pm 4$ |
| $N_2$ | $1100 \pm 330$ | $19 \pm 6$ |
| NO | $1600 \pm 480$ | $28 \pm 8$ |
| NS | 1900 [a] | 33 |
| HCN | $3700 \pm 1100$ | $65 \pm 19$ |
| | or $3840 \pm 140$[b] | or $70 \pm 2$ |
| $NH_3$ | $5500 \pm 1650$ | $96 \pm 29$ |

[a]Garrod & Herbst (2006), as listed in the KIDA database (Wakelam et al., 2012)

[b]This work; see §2.6.8

Note. — Sublimation temperatures $T_{jump}$ calculated using typical ISM conditions following Hollenbach et al. (2009). All binding energies from Wakelam et al. (2017), as listed in the KIDA database (Wakelam et al., 2012), unless otherwise noted. In all cases, the binding surface is assumed to be $H_2O$ ice.

of nitrogen as contributors to cometary nitrogen, based on chemical and physical principles. It would be very surprising if these species were able to undergo solid-state chemistry and contribute to chemical complexity, given their low sublimation temperatures and binding energies (as shown in Table 2.4) and the slow rates at which gas-phase chemistry proceeds. The molecular species NO and NS also likely have binding energies too low to permit freeze-out and its subsequent chemical enrichment.

An additional source of nitrogen for comets may exist: refractory nitrogen within interstellar dust. Nitrogen has not been detected directly in ISM dust, and it is difficult to observationally constrain the presence of nitrogen in carbon-rich dust via spectroscopic observations (Jones, 2016). Nonetheless, an upper limit on nitrogen's abundance can be inferred from measurements of N in interstellar gas, specifically via the depletion of N in diffuse ISM gas relative to the cosmic abundance of nitrogen atoms. Nieva & Przybilla (2012) measure the present-day cosmic abundance of nitrogen (relative to hydrogen) in the local Universe to be $N/H = 62 \pm 6$ ppm.

Jensen et al. (2007) measure the abundance of N I gas along multiple sight lines of the diffuse ISM to be $51 \pm 4$ ppm. Based on these numbers, the nitrogen depletion in the diffuse ISM is $11 \pm 7$ ppm. This number may represent depletion into different types of nitrogen sinks, such as formation of $N_2$ molecules or other species, but this depletion is measured in low-extinction (low $A_V$) environments where molecular $N_2$ would be rapidly destroyed by interstellar ultraviolet radiation. Therefore, the most likely interpretation is nitrogen depletion into refractory dust grains. In any case, the $11 \pm 7$ ppm is an upper limit on the available nitrogen in interstellar refractory dust. Whittet (2010) and Whittet et al. (2013) show that the abundance of oxygen atoms within ices on interstellar dust grains is 116 ppm (relative to H), and the solar O/H abundance is 457 ppm. Of this, about 50−60% of the oxygen atoms are in $H_2O$, with the rest in CO, and $CO_2$). Taking 50% of the 116 ppm as $H_2O$ ice yields an $H_2O$ ice-on-dust abundance of 58 ppm versus H in the ISM. Dividing the refractory N value by this $H_2O$ on dust, we present an upper limit of $19 \pm 12\%$ on refractory nitrogen in the ISM relative to water. This upper limit is comparable to the bulk nitrogen abundance in comets. Because there are no other apparent sources of nitrogen to comets with high enough abundance, we suggest that interstellar dust is the likely origin of the majority of cometary nitrogen.

### 2.7.2 $^{15}$N enrichment

In the previous subsection we suggested that the bulk of cometary nitrogen may be inherited from interstellar dust, as molecular ices do not have a high enough abundance relative to water to provide the majority of cometary nitrogen. To further explore the origins of cometary nitrogen, we turn to the isotopic signature of $^{15}$N. Isotopic ratios such as the $^{14}N/^{15}N$ ratio are commonly used to trace populations of material, as the isotopic ratio can be robust to physical processes and persist through time. In the solar system, the nitrogen in planetesimals is significantly more $^{15}$N-rich

than the Sun and the local interstellar medium: the solar value $^{14}N/^{15}N$ ratio is 441, while planetesimals have values ranging from 200, 50, or 140 (Füri & Marty, 2015, for bulk chondrites, chondrite hot spots, and comets, respectively). Direct measurements of $^{14}N/^{15}N$ in the dust particles of Comet 81P/Wild 2 show a range of $^{14}N/^{15}N$ values from $\sim 180-270$ (McKeegan et al., 2006). The present-day Earth itself has a sub-solar $^{14}N/^{15}N$ ratio of 272 (Anders & Grevesse, 1989).

The common interpretation of the $^{15}N$ enrichment in comets and other bodies is that it originates in the low-temperature molecular chemistry that occurs in either interstellar clouds or the early phases of star and planet formation (Charnley & Rodgers, 2008; Wirström et al., 2012; Hily-Blant et al., 2013; Füri & Marty, 2015; Bockelée-Morvan et al., 2015; Alexander et al., 2017). $^{15}N$ fractionation is consistently observed in N-bearing molecular ices (amines & nitriles) in dense star-forming gas (Hily-Blant et al., 2013; Wampfler et al., 2014, as well as this study). Hily-Blant et al. (2017) present evidence for multiple nitrogen reservoirs within forming solar systems, with distinct isotopic signatures. The similar $N/H_2O$ abundances for N-bearing molecules around protostars derived in this work, and in cometary ices, further lends support to the interpretation that ices are the $^{15}N$ donor to comets. However, recent work by Roueff et al. (2015) and Wirström & Charnley (2018) indicates that, when updated reaction rates and more sophisticated quantum-chemical computations are included, the current chemical networks cannot reproduce the observed $^{15}N$ enrichments in several N-bearing molecules, leaving room for exploration of the origins of $^{15}N$ in the dense ISM. Regardless, observations clearly indicate that ISM chemistry can produce $^{15}N$ enrichments in distinct chemical families (e.g. nitriles).

Thus, while substantial evidence supports a molecular ice origin for $^{15}N$ in comets, we ask whether a dust origin be ruled out entirely. This question is especially important to resolve given the large contribution of N from dust, as a small $^{15}N$ contribution from dust would matter more than a large $^{15}N$ contribution from ices. Unfortunately,

the $^{15}$N content of ISM dust is both unknown and totally unconstrained by observation; this requires us to rely on indirect evidence to investigate where cometary $^{15}$N originates. Most of the nitrogen in interstellar dust would be expected to be contained in carbonaceous (rather than silicate) grains. The formation of carbonaceous dust, discussed by Chiar et al. (2013), occurs in $\sim$ 1000 K environments that do not encourage chemical fractionation of nitrogen. The incorporation of nitrogen into hydrocarbon dust, discussed by Jones (2016), also would not be expected to enrich $^{15}$N over $^{14}$N. The cores of interstellar dust grains consist of presolar stardust that form directly from stellar ejecta (Clayton & Nittler, 2004; Chiar et al., 2013). While the $^{14}$N/$^{15}$N ratio of interstellar dust is unknown, individual presolar stardust grains can survive planetesimal formation intact and are amenable to isotopic study. These stardust grains, by virtue of their localized formation, inherit isotopic ratios directly from the nucleosynthetic and stellar evolutionary processes in their parent star. Presolar stardust grains, particularly SiC-X, graphite, and $Si_3N_4$, were studied by Clayton & Nittler (2004). Graphite grains typically have the same nitrogen isotopic ratio as the Sun, but SiC-X and $Si_3N_4$ grains are $^{15}$N-rich, with $^{14}$N/$^{15}$N values as low as 20 in some cases. Clayton & Nittler (2004) discuss how these high $^{15}$N values may be linked to the dust formation and nucleosynthesis processes in supernovae. In a related process, nova eruptions may be partly responsible for the gradual rise of $^{15}$N enrichment in a galaxy over time (Romano et al., 2017).

Additional evidence comes from analysis of organic matter within carbonaceous chondrites. Notably, the $^{15}$N hotspots in chondrites are not typically correlated with mineral rims or individual silicate grains (Alexander et al., 2017), although an instance of $^{15}$N enrichment near a supernova silicate grain in an IDP was noted by Messenger et al. (2005). The variable $^{15}$N enrichment (concentrated in $^{15}$N-rich "hotspots") might be consistent with an origin in diverse, heterogeneous stardust grains which each carry a different degree of $^{15}$N enrichment. This may also be consistent with

how D and $^{15}$N hotspots do not exactly correlate: $^{15}$N hotspots are often associated with $^{13}$C isotopic anomalies, while D hotspots do not co-vary with $^{13}$C (Alexander et al., 2017). These isotopic co-variations may also just be the result of chemistry: Wirström et al. (2012) note that for HCN and HNC, the reactions that lead to $^{15}$N enrichment do not correlate with the most extreme D enrichment.

If there exist thermal, aqueous, or chemical processes that can transport $^{15}$N out of stardust grains and into organic matter during the formation of comets and other bodies, then we may not yet be able to rule out a dust origin for $^{15}$N in these planetesimal bodies. Otherwise, most of the available evidence is in favor of a molecular ice origin, although recent work in chemical models indicates that further theoretical and laboratory work is needed to understand the precise reactions that lead to $^{15}$N enrichment. In this framework, molecular ices are the donor of $^{15}$N to protoplanetary solid bodies — and ultimately to the Earth. Thus, following these molecular ices allows us to astronomically trace a meaningful component of the nitrogen that later becomes a part of terrestrial worlds.

## 2.8 Conclusions

From our analysis of the nitrogen-bearing organic molecular inventories in a high-mass hot core, the HCN lines towards a low-mass protostar, and through scaling molecular abundances relative to $H_2O$, we present the following conclusions:

1. HCN is by far the most abundant nitrogen-bearing organic in the Orion KL Hot Core, carrying $74^{+5}_{-9}$% of nitrogen-in-organics.

2. The HCN abundance in the envelope of IRAS 16293−2422 exhibits a jump profile, with $X_{\rm in} = 5.9 \pm 0.7 \times 10^{-8}$ and an outer HCN abundance $X_{\rm out} = 1.26 \pm 0.13 \times 10^{-9}$.

3. We derive an HCN sublimation temperature $T_{\rm jump} = 71 \pm 3$ K, from which

we make an astronomically-motivated prediction that the HCN binding energy $E_B/k = 3840 \pm 140$ K.

4. The $N/H_2O$ ratio in molecular ices seen in the inner protostellar envelopes is similar to $N/H_2O$ in cometary ices. However, it is not high enough to account for the total $N/H_2O$ seen in comets. While the refractory nitrogen content in interstellar dust has not been measured, its upper limit is permissive enough to account for the bulk of cometary N. Therefore, we suggest that the nitrogen contained in interstellar dust is the likely precursor to most of the N in comets.

5. The high $^{15}N$ enrichment seen in cometary and meteoritic bodies has an unknown origin. Most evidence indicates that it is donated by molecular ices that underwent chemical fractionation of nitrogen isotopes, but the reactions responsible for this process are unclear. A dust origin of $^{15}N$ enrichment appears unlikely but cannot be ruled out.

# CHAPTER III

# Hunting for Hot Cores: Small-scale HCN Measurements Towards Five Low-mass Protostars

## 3.1 Preface

This work is planned to be submitted for publication, with co-authors Edwin A. Bergin, Jes K. Jørgensen, and Lars E. Kristensen.

## 3.2 Abstract

In young protostellar envelopes, observations of a "hot core" of evaporated molecular ices can provide critical information about the initial chemical conditions of terrestrial planet formation. However, bright low-mass protostellar hot cores are rare, and a widespread, high-resolution census of organic nitrogen carriers in low-mass protostellar hot cores has not yet been carried out. Here, we present results from one IRAM 30m program and two NOEMA campaigns observing $H^{13}CN$ $J = 1 - 0$ and $J = 3 - 2$ emission on large ($10'' - 30''$) and small ($\sim 1''$) scales towards five low-mass embedded protostars in Perseus ($d = 235$ pc). For each protostar, we fit a physical model to the observed spectral energy distribution and interferometric dust continuum measurements. We report a strong detection of compact hot core $H^{13}CN$ $3 - 2$ flux from L1455 IRS1, with peak intensity 200 mJy. We report 3-$\sigma$ flux upper limits

on the other four protostars ranging from $28-64$ mJy. A chemical abundance model fit to L1455 IRS1's emission gives a hot core abundance $X_{\rm in}({\rm HCN}) = 4 \times 10^{-8}$, a measurement within 50% of that seen at IRAS 16293−2422, a low-mass protostellar astrochemical benchmark. The non-detections towards the other four protostars imply upper limits of $X({\rm HCN})$ ranging from $4 \times 10^{-8}$ to $3 \times 10^{-7}$. Our work paves the way forward for a broad census of small-scale emission measurements of organic nitrogen carriers at low-mass protostars, while confirming that single-dish measurements of low-energy lines ($E_{\rm u}/k \lesssim 50$ K) cannot be extrapolated to small scales without supplementary interferometric observations.

## 3.3 Introduction

The origins of the Earth's nitrogen, a chemical element necessary for life as well as the primary constituent of our atmosphere, are unknown. The vast majority of nitrogen in the interstellar medium and star forming environments is N and $N_2$ (van Dishoeck et al., 1993; Schwarz & Bergin, 2014). In order to become part of terrestrial worlds, nitrogen must first become put into less volatile (i.e., vaporizable) forms, through chemical evolution or some other means of sequestration. Current work in protoplanetary disk chemical observations and modeling does not indicate that volatile species of nitrogen (N and $N_2$) experience substantial chemical processing into more condensible forms (Cleeves et al., 2018). In fact, for some nitrogen carriers such as $NH_3$, the opposite may occur, with $NH_3$ being converted back into $N_2$ in an inner disk (Pontoppidan et al., 2019). Thus, identifying which less-volatile carriers of nitrogen are already present at the dawn of the planet formation process is critical for understanding the origins of nitrogen in planetesimals such as chondrites and comets, and ultimately to terrestrial worlds like the Earth.

Bergin et al. (2014, 2015) have identified carbonaceous dust and molecular ices as promising reservoirs for the carbon and nitrogen that would arrive ultimately to

Earth, but this remains unconfirmed. In Rice et al. (2018, Chapter II), we investigated this question further by studying nitrogen-bearing organics in Orion KL, a high-mass protostellar environment, and IRAS 16293−2422, a low-mass protostar (hereafter IRAS 16293). In that work, we identified nitrogen sequestered into refractory forms (e.g., dust) as the likely progenitor of the majority of cometary nitrogen, while a still substantial minority of nitrogen may have been contributed by $^{15}$N-rich molecular ices such as HCN and other organic nitrogen carriers. However, with only two sources under consideration, these results would be made more robust by the inclusion of measurements of nitrogen-bearing species towards many more protostellar sources.

Deeply embedded protostars can provide an important laboratory to study the chemistry of star formation, forming a key link between the chemistry of the interstellar medium and the chemistry of the protoplanetary disks in which planets are born (Jørgensen, 2011). Low-mass hot cores, known sometimes as "hot corinos" (Cazaux et al., 2003; Maret et al., 2004, 2005), have been identified around low-mass protostars and are typically characterized by a one- to two-order-of-magnitude jump in the abundance of molecular species such as $H_2CO$, $CH_3OH$, and other complex organic molecules (van Dishoeck et al., 1995), a boosted HCN abundance (Brinch et al., 2009a; Rice et al., 2018), and the presence of complex molecules not often seen in the interstellar medium such as glycoaldehyde ($HCOCH_2OH$; Jørgensen et al., 2012). Measurements of chemical enrichment in both high-mass and low-mass hot cores are common, but (especially in low-mass hot cores) nitrogen chemistry has few observational constraints. For example, accurate measurements of the hot-core abundance of HCN (as traced by the optically thin isotopologue H$^{13}$CN) in low-mass protostars are restricted to NGC 1333−IRAS2A (Jørgensen et al., 2005a; Brinch et al., 2009a, as seen by the SMA) and IRAS 16293 (Rice et al., 2018, using *Herschel* observations). Measurements of HCN and its isotopologues have been noted to be useful probes of the inner envelope and/or disk, due to their high abundances, strong transitions, and

minimal affectedness by outflows (Jørgensen et al., 2005a); hence, they are sometimes used as tracers of kinematics, without a view towards abundance determinations and nitrogen chemistry (e.g., Takakuwa et al., 2007; Jørgensen et al., 2009). The one low-mass protostar for which the nitrogen chemistry is particularly well-constrained on sub-arcsecond scales is IRAS 16293, the target of the ALMA program "Protostellar Interferometric Line Survey" (PILS; Jørgensen et al. 2016), for which detailed measurements exist of $CH_3NCO$, $NH_2CN$, $CH_3CN$, $C_2H_5CN$, $C_2H_3CN$, $HC_3N$, $CH_3NC$, $N_2O$, $CH_2NH$, NO, $H_2NCN$, and HONO, with upper limits published for $NH_2OH$ and $CH_3NH_2$ (Ligterink et al., 2017b, 2018; Coutens et al., 2018, 2019a,b; Calcutt et al., 2018b,d). HNCO was also measured towards IRAS 16293 by Bisschop et al. (2008). Considering the evolutionary stages before and after the protostar, a number of observations of $H^{13}CN$ in prestellar cores have been carried out (see, for example, Hily-Blant et al. 2013; Magalhães et al. 2018), and ALMA has made possible measurements and surveys of HCN and its isotopologues in a number of protoplanetary disks (Guzmán et al., 2015, 2017; Hily-Blant et al., 2017; Bergner et al., 2019), facilitating an enhanced understanding of nitrogen chemistry in these disks (e.g., Cleeves et al., 2018).

To fill the gap between prestellar cores and protoplanetary disks in our observational knowledge of HCN abundances, we have carried out an observational program using the IRAM 30m and NOEMA observatories. This set of observing campaigns has targeted a modest pilot sample of low-mass embedded protostars with the goal of isolating the hot core's HCN emission from the readily-observable HCN emission from the broad envelope. In this chapter, we combine continuum and line observations of this sample of embedded protostars to first constrain their physical structure, and then measure their HCN abundances on small scales. We present IRAM 30m single-dish and NOEMA interferometric observations of five Class 0 and I young stellar objects. Using continuum data and dust radiative transfer models, we constrain the

physical structure of these sources. Given this physical structure, we then interpret our measurements of $H^{13}CN$ and attempt to isolate the hot core in each source. This chapter is laid out as follows: Section 3.4 introduces the selected sample of five Class 0 and I protostars. In Section 3.5, we introduce the IRAM 30m line observations, the NOEMA interferometric continuum and line observations, and the SED data, including some *Herschel* Gould Belt Survey photometric data from $70 - 500$ $\mu$m that has not been previously published. Section 3.6 discusses the constraints on the envelope and disk properties from the continuum data inferred from radiative transfer models of dust in protostellar envelopes. Section 3.7 discusses the results of the chemical abundance modeling of the $H^{13}CN$ lines, both towards L1455 IRS1, which is detected strongly on small scales by NOEMA, and the other four protostars, for which we only measure upper limits. Finally, we discuss the connection between our work and other observations of protostars in Section 3.8. In Section 3.9, we summarize the main conclusions of the chapter.

## 3.4 Source Selection

We selected a handful of sources which overlapped in the *Spitzer c2d* (cores to disks) survey (Evans et al., 2003; Boogert et al., 2004, 2008) of circumstellar ices and dust from mid-IR spectroscopic measurements, and the the James Clerk Maxwell Telescope (JCMT) survey of sub-mm cores in Perseus (Kirk et al., 2006, 2007; Jørgensen et al., 2007a) which was part of the Coordinated Molecular-Probe line Extinction Thermal Emission (COMPLETE) program (Goodman, 2004; Ridge et al., 2006). The five protostars L1455 IRS 1, B1-a, IRAS 03235, B5 IRS1, and L1455 IRS4 are low-mass, young embedded protostars that lie in the Perseus star-forming region. We optimized for the sources with (a) deep 9.7$\mu$m absorption seen in the Spitzer IRS spectra, (b) bright 850$\mu$m flux $S_{\nu,850}$ as observed by SCUBA (Kirk et al., 2007), and (c) that would span a range of luminosities. The combination of criteria (a) and (b)

Table 3.1. Observed protostars' coordinates and identifiers

| Source Name | R.A. (J2000) | Decl. (J2000) | $v_{\rm LSR}$ (km s$^{-1}$) | Alternate IDs |
|---|---|---|---|---|
| L1455 IRS1 | 03:27:39.11 | +30:13:02.8 | 5.0 | IRAS 03245+3002, E09 130, RNO 15-FIR, Per-emb 17 |
| B1-a | 03:33:16.67 | +31:07:55.1 | 6.3 | IRAS 03301+3057, B1-IRS, E09 296, Per-emb 40 |
| IRAS 03235 | 03:26:37.46 | +30:15:28.2 | 5.0 | IRAS 03235+3004, E09 127, Per 04, Per-emb 25 |
| B5 IRS1 | 03:47:41.61 | +32:51:43.9 | 10.0 | E09 505, Per-emb 53 |
| L1455 IRS4 | 03:27:43.25 | +30:12:28.9 | 5.0 | L1455 SMM1, E09 132, Per-emb 20 |

Note. — Per-emb designations reference the catalog of Enoch et al. (2009), while E09 designations reference Evans et al. (2009).

ensured that all sources would have substantial envelopes suitable for molecular line observations. The sources B1-a, IRAS 03235, L1455 IRS4, B5 IRS1, and L1455 IRS1 have previously-estimated luminosities (respectively) of 1.3, 1.9, 3.1, 4.7, and 7.0 $L_\odot$ as estimated by (Hatchell et al., 2007) from piecewise SED integration of spectral energy distributions spanning $1 - 1100$ $\mu$m. We find some differences in these sources' luminosities in our physical modeling, which we discuss in Section 3.6.

Table 3.1 lists the five low-mass protostars we observed with their coordinates, velocities, and alternate identifications. By coincidence, this sample of five protostars overlaps completely with the 16 protostars observed and studied in IRAM 30m observations by Graninger et al. (2016), Bergner et al. (2017), and Law et al. (2018). Three of our sources (B1-a, IRAS 03235, and B5 IRS1) also appear in that program's pilot study (Öberg et al., 2014). Our sample of protostars have also been the targets of various *Herschel* programmes: B1-a and L1455 IRS1 were observed in the *Herschel* "CO in ProtostarS" (COPS, P.I.: J. Green) and "Dust, Ice, and Gas in Time" (DIGIT, P.I.: N. Evans) programmes (Green et al., 2016), while IRAS03235 was observed as part of the "*William Herschel* Line Legacy" (WILL, P.I.: E. F. van Dishoeck) survey (Karska et al., 2014). Also, all five protostars were observed in the *Herschel* Gould Belt Survey (André et al., 2010; Sadavoy et al., 2014); our use of photometric data

from this survey (Pezzuto et al., in prep.; Private Communication) is described in Section 3.5.3. Finally, all five of these protostars have been observed as part of the VLA Nascent Disk and Multiplicity (VANDAM) survey (Segura-Cox et al., 2016; Tobin et al., 2016a, 2018), a systematic high-resolution VLA survey of 94 protostars in Perseus at $\lambda = 0.8 - 6.4$ cm to investigate protostellar multiplicity. Of these five sources, two were identified as close ($< 100$ au) binaries: L1455 IRS1 and B1-a, both of which received ALMA followup at 1.3 mm (Tobin et al., 2018). Another source, B5 IRS1, was resolved (size $120 \times 83$ mas) in the VANDAM observations, but was not well-described by a disk model and was ruled out as a disk candidate (Segura-Cox et al., 2018).

The selected sample thus represents a small yet diverse group of well-characterized low-mass protostars which spans an informative range in evolutionary class, luminosity, and multiplicity. We adopt a distance $d = 235$ pc to Perseus, following parallax measurements of $H_2O$ masers in NGC 1333 (Hirota et al., 2008).

## 3.5 Data and Observations

We have carried out combined observations designed to measure $H^{13}CN$ emission arising from a protostellar hot core; these observations include single-dish measurements designed to disentangle large-scale emission from that seen on smaller scales. In this paper, we present observations from three observing programs: the IRAM 30m program 169-14 (P.I.: T. Rice) and the NOEMA programs W15AI and W16AN (P.I.: T. Rice). These three programs together performed measurements of the $H^{13}CN$ $1-0$ and $3-2$ lines (at 86.340 and 259.012 GHz, respectively) of our sample of five protostars described in Section 3.4. The IRAM 30m beam size varied from $10''$–$30''$, while the resolution of the NOEMA maps was $\sim 1''$ at 260 GHz and $\sim 2''$ at 86 GHz. Both $H^{13}CN$ lines are detected towards all five sources in the IRAM 30m program. In the NOEMA data, only the $H^{13}CN$ $3-2$ line towards L1455 IRS1 is clearly detected,

with upper limits placed on the flux measurements towards the other four sources.

We have also made use of broadband photometric measurements in order to construct spectral energy distributions (SEDs). We describe the *Herschel* Gould Belt Survey photometry, which forms the core of these SEDs, below, alongside other photometric continuum measurements made at the James Clerk Maxwell Telescope (JCMT) and the Caltech Submillimeter Array (CSO).

### 3.5.1 IRAM 30m observations

We observed these five protostars using the IRAM 30-m telescope from 2014 December 26-28 in program 169-14 (P.I.: Rice). This project consisted of single-pointing measurements of the $H^{13}CN$ and $HC^{15}N$ $(1-0,\ 3-2)$, $C^{17}O$ and $C^{18}O$ $(1-0,\ 2-1)$ and DCN $(2-1)$ line emission towards 5 protostars in Perseus. We used the Eight-Mixer Receiver (EMIR) heterodyne receivers in bands E090, E150 and E330, together with the Versatile SPectrometer Array (VESPA) and Fourier Transform Spectrometer (FTS) backends. VESPA provided high-resolution spectra with resolution 6.5 kHz in a targeted band 18 MHz wide, while FTS provided broad spectra at 50 kHz resolution in two simultaneous non-contiguous frequency windows, each 1.8 GHz wide. Scans were carried out at 86, 111, 145, 222, and 259 GHz; the 86 and 145 GHz scans were observed simultaneously. We observed each source at the 86+145 GHz combined setting for 20 minutes; the 111 and 222 GHz settings, each for 12 minutes. In the 259 GHz setting, on-source integration times varied from 72 minutes (L1455 IRS1, B5 IRS1, L1455 IRS4) to 88 minutes (IRAS 03235) and 140 minutes (B1-a) in order to reach a more consistent signal-to-noise ratio. The angular resolution of the telescope beam varied from $9\farcs7$ (at 259 GHz / 1.2mm) to $29\farcs2$ (at 86 GHz / 3.5mm). The pointing and focus were calibrated at the beginning of the run and after any receiver tuning. Pointing was checked every hour during the observations, and focus was repeated after sunset or sunrise. Focus and pointing calibrators included Uranus

and the quasars 0316+413 and 0234+285.

We reduced these spectra using the CLASS program from the GILDAS suite of radio astronomy tools[1]. Individual spectral scans from VESPA were averaged together and baseline-subtracted with a first-order baseline, fit to emission-free channels on both sides of each line. We converted antenna temperature ($T_a^*$) to main beam temperature, $T_{\rm mb}$, by applying efficiencies from Kramer (1997)[2] such that $T_{\rm mb} = T_a^* \times \frac{F_{\rm eff}}{B_{\rm eff}}$. At 260 GHz, the forward efficiency is 0.877 and the beam efficiency is 0.46; at 86 GHz, the forward and beam efficiencies are 0.950 and 0.76, respectively.

### 3.5.2 NOEMA observations

To follow up our IRAM-30m program with finer spatial resolution, we observed the sample of five protostars in NOEMA project W16AN and W15AI (P.I.: T. Rice). In W16AN, NOEMA Band 1 (3 mm) observations were carried out on 2016 December 09 in "C" (compact) configuration, and NOEMA Band 3 (1 mm) observations on 2017 January 23 in "D" (sub-compact) configuration. Each track included eight antennas. Both tracks utilized track-sharing to interleave observations of all science targets with their calibrators, minimizing overhead and maximizing $u, v$ coverage. In the Band 1 track, the projected baseline lengths range from a minimum of 23.6 m (6.9 k$\lambda$) to a maximum of $239.4 - 254.9$ m ($69.9 - 74.4$ k$\lambda$). In the Band 3 track, the projected baselines cover 17 to 175 m ($15 - 151$ k$\lambda$). The Band 1 observations covered all five sources with an equal on-source integration time of 12 minutes each. Band 3 covered all targets except for L1455 IRS1; B1-a was observed for 42 min, IRAS03235 for 36 min, LIRS4 for 30 min, and B5-IRS1 for 60 min.

Band 3 observations of L1455 IRS1 were separately observed in the much deeper program NOEMA W15AI (P.I.: T. Rice; described in depth in Chapter III). In brief, L1455 IRS1 was observed on 2015 December 03, 21, and 23 in NOEMA Band 3

[1]http://www.iram.fr/IRAMFR/GILDAS

[2]Also available at http://iram.fr/IRAMFR/ARN/aug05/node6.html

as part of NOEMA project W15AI. All three tracks included seven antennas; these observations in "C" and "D" configurations covered projected baseline lengths between 14.9 and 239.5 m ($13 - 207$ k$\lambda$). The total integration time on-source was 8.1 h; the correlator settings were identical to those described for the NOEMA Band 3 observations described below for project W16AN.

The Band 1 spectral configuration included four narrow-band spectral windows, plus the wide-band WideX correlator. The narrow-band windows covered lines of $H^{13}CN$ and $HC^{15}N$, $NH_2D$, $CH_3OH$, SO, and $SO_2$. These windows had resolution 0.078 MHz (0.27 km s$^{-1}$) to 0.156 MHz (0.538 km s$^{-1}$). The WideX correlator captured a contiguous 3.6 GHz spectral band from 85703 to 89300 MHz at 2 MHz (6.9 km s$^{-1}$) resolution. Calibrators included 3C454.3, MWC349, J0324+341, and 0333+321.

The Band 3 spectral configuration included four narrow-band spectral windows, plus the wide-band WideX correlator. Three narrow-band windows were centered on the $H^{13}CN$ and $HC^{15}N$ transitions and one centered on an SiO-v1 shocked gas tracer. These windows had resolution 0.078 MHz (0.09 km s$^{-1}$) to 0.3 MHz (0.36 km s$^{-1}$). The WideX correlator captured a contiguous 3.6 GHz spectral band from 257285 to 260884 MHz at 2 MHz (2.3 km s$^{-1}$) resolution. Calibrators included 3C454.3, MWC349, J0324+341, 0333+321, 3C84, and LKHA101.

In each NOEMA Band, the narrow-band correlator could only process data from six antennas, so two antennas' data were excluded from all narrow-band data products. Data were simultaneously fed into the WideX correlator, which could handle all eight antennas. The WideX data products have subsequently higher signal-to-noise; however, the lower spectral resolution (2 MHz) can dilute narrow lines, most notably at Band 1 where the velocity resolution is 6.9 km s$^{-1}$. NOEMA's most recent wide-bandwidth correlator, PolyFIX, was not yet operational when these observations were taken.

We calibrated and reduced these interferometric data using the CLIC and MAPPING programs, also from the GILDAS suite of radio astronomy tools. Continuum $u, v$ tables at 1 mm and 3 mm were extracted from the WideX (3.6 GHz-wide) data products by averaging all line-free channels in visibility space. Emission line $u, v$ tables were then created by subtracting the appropriate averaged continuum. We then created continuum maps and spectral line datacubes using CLEAN. The beam size at 3.4 mm is $2\farcs3$, while the beam size at 1.1 mm is $1\farcs3$.

### 3.5.3 Spectral Energy Distributions

We have compiled spectral energy distributions (SEDs) of each protostar to facilitate our fitting of physical models to these sources. Because our physical modeling approach (described in Section 3.6) is focused on the protostellar envelope, we have restricted our wavelength coverage to wavelengths longer than 50$\mu$m. Far-infrared photometry is known to be essential for accurately modeling protostellar properties (Furlan et al., 2016). We therefore have ensured that the far-IR to submillimeter wavelength range is well-sampled with high signal-to-noise photometric measurements, by including *Herschel* Gould Belt Survey (HGBS) photometry alongside ground-based measurements from the Submillimetre High Angular Resolution Camera (SHARC) at 350$\mu$m on CSO (Wu et al., 2007), the Submillimetre Common-User Bolometer Array 2 (SCUBA) 850 $\mu$m at JCMT (Kirk, Johnstone, & Tafalla, 2007) and Bolocam on CSO at 1.1 mm (Enoch et al., 2006).

*Herschel* photometry at 70, 160, 250, 350, and 500 $\mu$m was obtained from the *Herschel* Gould Belt Survey, (André et al., 2010; Pezzuto et al., 2017; Sadavoy et al., 2014), (Pezzuto et al., in prep.; Private Communication). These data were created from simultaneous PACS and SPIRE scans. The *Herschel* beam size ranges from $5''$ at 70$\mu$m to $36''$ at 500$\mu$m; it is diffraction-limited over its whole energy range[3].

[3]PACS Observers' Manual: `http://herschel.esac.esa.int/Docs/PACS/pdf/pacs_om.pdf` and SPIRE Observers' Manual: `http://herschel.esac.esa.int/Docs/SPIRE/pdf/spire_om_`

The photometric catalog includes both peak and total fluxes for extended sources; for our SED fitting, we make use of the summed extended source flux, as emission from many of these protostars extends beyond the beam at some or all wavelengths. To properly account for calibration uncertainties in the photometry, we added 5% in quadrature to the estimated statistical errors on the datapoints per the published on-line documentation for PACS and SPIRE *Herschel* instruments[4].

We used measurements at 350, 850, and 1100 $\mu$m from SHARC, SCUBA, and BOLOCAM (Wu et al., 2007; Kirk et al., 2007; Enoch et al., 2006) to supplement the HGBS photometry. For the SCUBA and BOLOCAM measurements, we also took the total flux enclosed by a given source's associated "clump" identified in the CLUMPFIND procedure. We assigned a 33% uncertainty to these 850$\mu$m and 1.1 mm flux measurements to account for difficulties in comparing extended sources' fluxes given the sometimes-crowded environments, different source extraction profiles, and other systematic issues.

### 3.5.4 Observational Results

Both $H^{13}CN$ lines ($3-2$ and $1-0$) are detected in the IRAM 30m data towards all five sources. The three hyperfine components of the $1-0$ line are all present, and show flux ratios consistent with optically thin emission. In Figure 3.1, we show the IRAM 30 m detections of $H^{13}CN$ $1-0$ and $3-2$ emission towards our five protostars. Faintly shown in red are the NOEMA central-pixel spectra, shown on the same absolute flux scale. In Figure 3.2, we again show the $H^{13}CN$ $1-0$ and $3-2$ emission, but re-scaled to highlight the NOEMA spectral measurements. Faintly shown in gray are the same IRAM 30 m spectra. Only one $H^{13}CN$ line towards

v24.pdf

[4]"Quick-Start Guide to the *Herschel*-PACS: The Photometer": https://www.cosmos.esa.int/documents/12133/996891/PACS+Photometer+Quick+Start+Guide/68bc6d96-df8a-c97f-fdee-a910d419c865, and the SpireCalibrationWeb wiki entry: http://herschel.esac.esa.int/twiki/bin/view/Public/SpireCalibrationWeb#Photometer_data_reduction

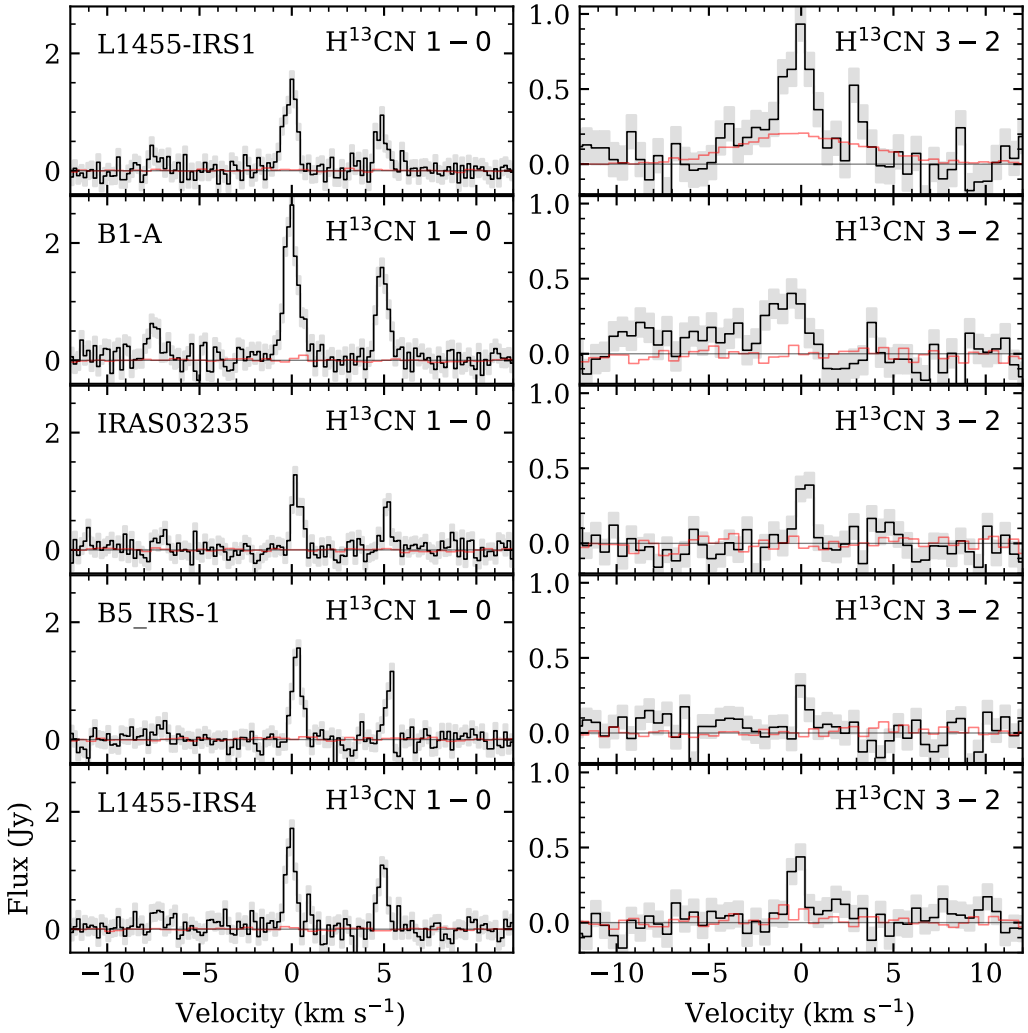


Figure 3.1 Spectra of all 5 sources, showing the $H^{13}CN$ 1−0 and 3−2 lines as observed (in black) by the IRAM 30m telescope, and (in red) by NOEMA. The IRAM 30m beam is 30″ at 3 mm and 10″ at 1 mm. The NOEMA interferometer filters out all emission larger than 16.″1 at 3 mm, and 7.″3 at 1 mm.

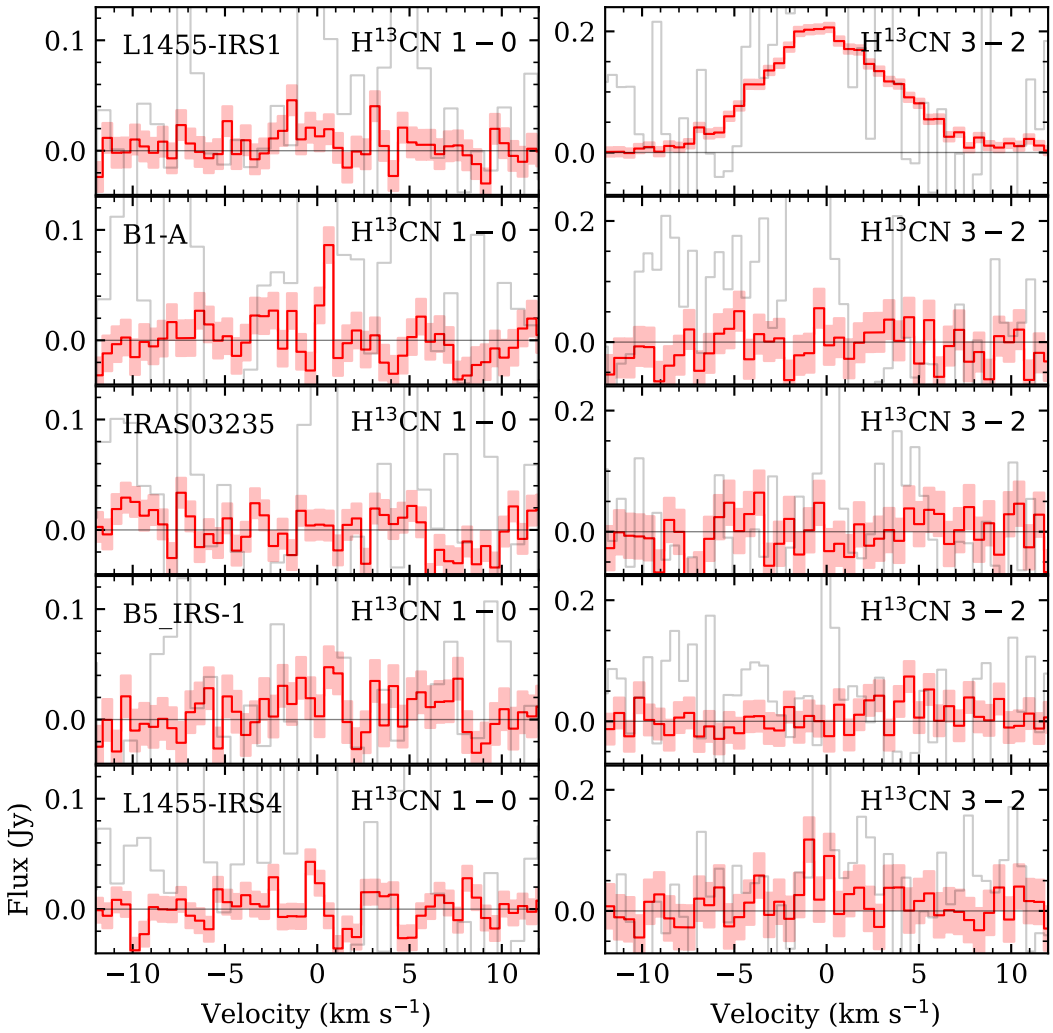


Figure 3.2 Same as Fig. 1, but with the focus on the NOEMA spectra in red. Spectra of all 5 sources, showing the $H^{13}CN$ $1-0$ and $3-2$ lines as observed (in black) by the IRAM 30m telescope, and (in red) by NOEMA. The NOEMA interferometer filters out all emission larger than 16.″1 at 3 mm, and 7.″3 at 1 mm.

one protostar is firmly detected with NOEMA; in some channels of the other lines and sources, hints of emission at the $1-3\sigma$ level are sometimes present at the same velocities that emission is seen in the IRAM spectra.

In Figure 3.3, we show the CLEAN maps from NOEMA of the 3.4 and 1.1 mm continuum emission, as well as the moment-zero map of the HCN $1-0$ emission line. In Figure 3.4, we show the moment-zero maps of the $H^{13}CN$ $3-2$ emission, as well as the azimuthally averaged visibilities as a function of projected baseline. For the moment-zero maps and the integrated-flux visibility plots, we show data from the WideX correlator as it has higher signal-to-noise, as it utilized all available antennas rather than being restricted to six as the narrow-band correlator was.

The disparities in these IRAM 30m and NOEMA spectra show decisively that essentially all of the narrow $H^{13}CN$ $1-0$ and $3-2$ emission arises from a large-scale ($\sim$ 1000s of au) envelope rather than a compact ($\sim$ 100s of au) central component such as a disk or hot core. Given the upper-state energies of the $1-0$ and $3-2$ lines of 4.1 and 24.9 K, respectively, it is perhaps unsurprising that the majority of the emission would reside in a cold extended envelope containing much more molecular material, in an absolute sense, than the inner few hundreds of au of the hot core or disk. Nonetheless, given that all five sources have comparable flux in each line in the IRAM 30m observations, the unique presence of bright and broad $H^{13}CN$ $3-2$ emission on small scales *only* at L1455 IRS1 (and absent, to a high degree of confidence, towards the other four observable sources) merits investigation into the origin of this compact emission, in part to identify what sets L1455 IRS1 apart. To further investigate this, we fit physical and chemical abundance models to these five protostars in the next two sections.

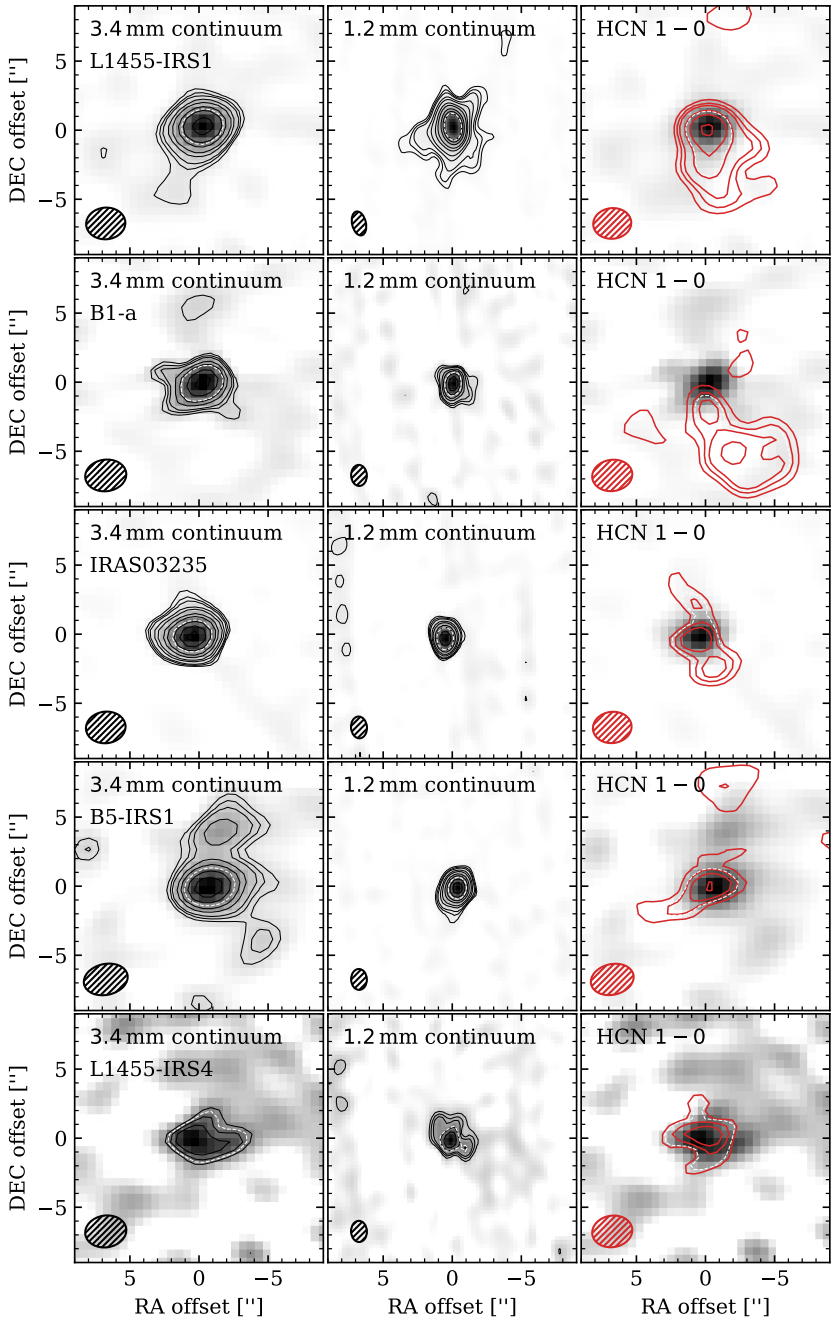


Figure 3.3 Maps of all five sources from NOEMA. Left column: 3 mm continuum. Middle column: 1 mm continuum. Right column: HCN $1-0$ line at 88.631 GHz (in red) over-plotted on the 3.4 mm continuum (in filled gray).

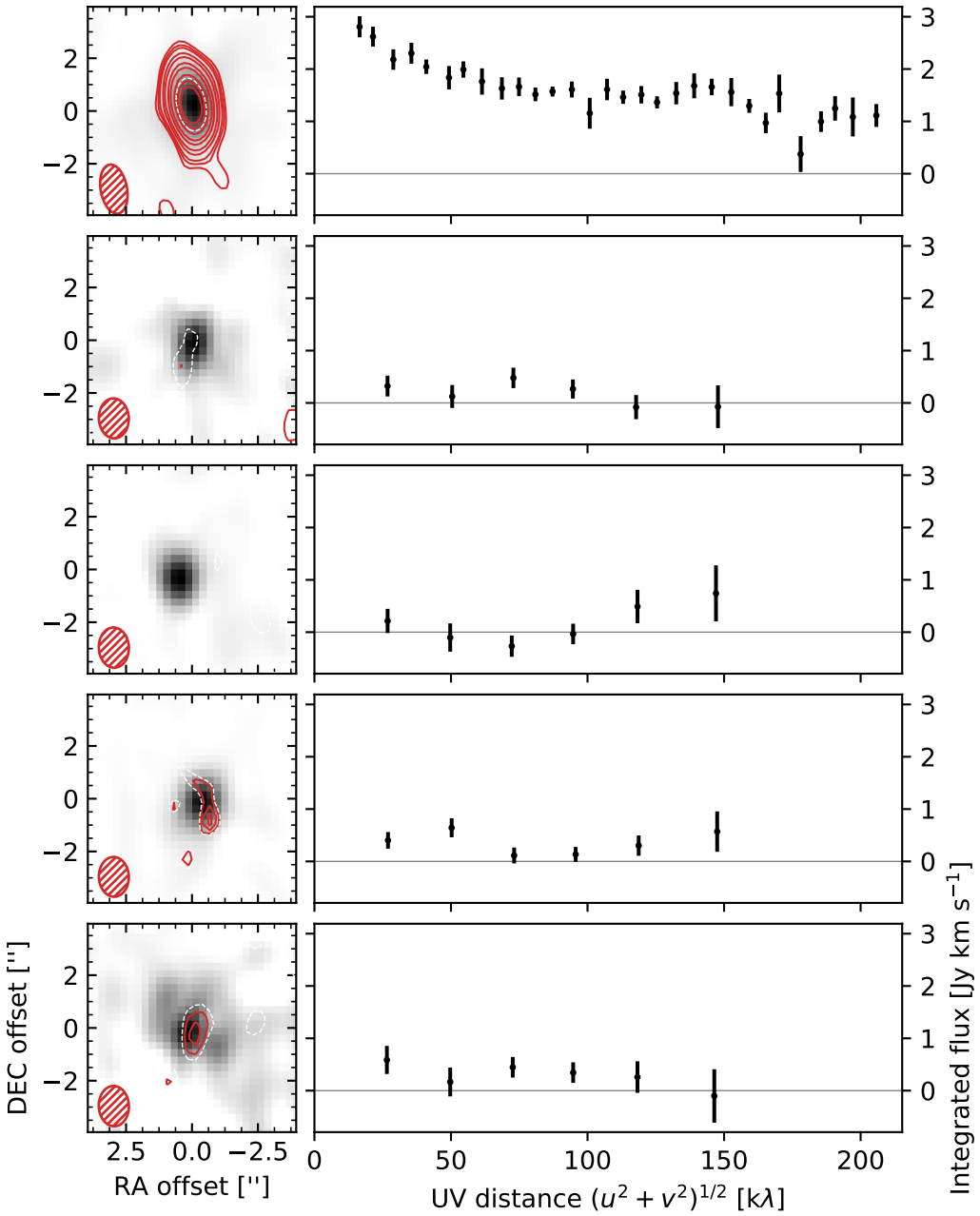


Figure 3.4 Maps and visibility plots of the $H^{13}CN$ $3-2$ line, which was firmly detected only towards L1455 IRS1 using NOEMA. Left column: map. Right column: azimuthally averaged visibility flux, taking the real part only.

## 3.6 Physical structure model

Our ultimate goal in this analysis is to identify emission arising from the protostellar hot core. To do this, we must understand the temperature and density structure in the protostellar envelope so that we can accurately interpret the molecular line emission, which depends sensitively on these physical properties. To constrain this temperature and density structure, we make use of a model with two physical components: (1) a one-dimensional (i.e., spherically symmetric) protostellar envelope in which a central luminous source heats a dusty envelope with a power-law density profile; and (2) a point-like "compact component" (e.g., a disk) with arbitrary flux at 1 mm and 3 mm. We fit this two-component model simultaneously to both the SED and the azimuthally-averaged interferometric visibility amplitudes in $u, v$ space measured by the NOEMA interferometer at 3.4 and 1.1 mm. We use a Markov chain Monte Carlo (MCMC) method to fit each protostar's model parameters to its data, which gives us both a "best-fit" set of model parameters as well as a posterior probability distribution on each parameter.

### 3.6.1 Model description

This combined physical model makes use of five floating parameters: the bolometric luminosity, $L_{\rm bol}$; the envelope mass within 10,000 au, $M_{\rm env}$; the density profile power-law exponent, $p$ (such that $\rho \propto r^p$, $p < 0$); and the compact fluxes at 1 mm and 3 mm, $F_{\rm c,1mm}$ and $F_{\rm c,3mm}$. The SED principally constrains $L_{\rm bol}$ and $M_{\rm env}$; $p$ is jointly constrained by the SED and the visibility profiles, while $F_{\rm c,1mm}$ and $F_{\rm c,3mm}$ are only constrained by the interferometer. Because our model is focused principally on constraining the envelope properties needed to reproduce the SED at wavelengths $\lambda > 50$ $\mu$m, we do not attempt to self-consistently model a disk component of the SED; rather, we include $F_{\rm c,1mm}$ and $F_{\rm c,3mm}$ as arbitrary corrections which help reproduce the 1 mm and 3 mm visibility amplitudes at long baselines (i.e., small physical

scales), where the envelope contribution should decline to zero in absence of a distinctly emitting compact component such as a disk.

We use the radiative transfer code Transphere (Dullemond et al., 2002) and RATRAN (Hogerheijde & van der Tak, 2000b,a)[5] to generate model SEDs and sky images. Transphere self-consistently solves the temperature in each radial shell and solves the SED; RATRAN creates model "sky" images given the dust temperature, density, and radiation field at given continuum wavelengths (i.e., 1 mm and 3 mm). We use dust opacities from Ossenkopf & Henning (1994). We create Fourier-transformed model images (in $u, v$ space) from the model sky images using Miriad (Sault et al., 1995) to allow direct, convolution-free comparisons with the data. We compare these modeled data products to the observed SED and the continuum fluxes measured by the interferometer in $u, v$ (visibility) space. This general approach was pioneered by Schöier et al. (2002); Jørgensen et al. (2005c, 2009), and Bisschop et al. (2008).

We fix the following physical parameters of the envelope model: the outer radius of the envelope, $r_{\rm out} = 10,000$ au; the inner radius of the envelope, $r_{\rm in} = 10$ au; the protostellar surface temperature, $T_* = 1000$ K; and the protostellar radius, $R_* = \sqrt{L_{\rm bol}}/\left(\frac{T}{5785}\right)^2 \times R_\odot$. In addition, we set the following computational parameters of the model: Number of logarithmically-spaced radial grid cells, $n_r = 20$; refinement radius, $r_{\rm ref} = 300$ au; number of grid cells within a refinement radius, $r_{\rm ref} = 10$; and convergence criterion, `convcrit` $= 10^{-5}$.

### 3.6.2 $u, v$ data handling

To best compare our interferometric visibility data to the spherically-symmetric envelope-plus-disk model, we take the following steps: phase recentering of the visibility data, averaging into azimuthal bins, and then using the real part, not the summed amplitude.

[5] `https://personal.sron.nl/~vdtak/ratran/frames.html`

*Phase recentering*: the initial phase center of these observations was misaligned from the actual continuum peak brightness position by up to $0\farcs84$; while this did not affect our ability to CLEAN these images, it is a significant issue in $u, v$ fitting. We therefore corrected for this misalignment by recentering the phase center in all $u, v$ tables. We calculated the required phase offsets for each source in each band by fitting a point-source using the MAPPING task "UV_FIT" in GILDAS. We applied the phase recentering to the visibilities using the following equations:

$$\phi = -2\pi \left( u \cdot \delta\theta_{\mathrm{R.A.}} + v \cdot \delta\theta_{\mathrm{Decl.}} \right) \tag{3.1}$$

$$\Re' = \Re \cdot \cos(\phi) - \Im \cdot \sin(\phi) \tag{3.2}$$

$$\Im' = \Re \cdot \sin(\phi) + \Im \cdot \cos(\phi) \tag{3.3}$$

in which $\phi$ is the phase offset, $\delta\theta$ is the angular offset on the sky (in radians, with components $\delta\theta_{\mathrm{R.A.}}$ and $\delta\theta_{\mathrm{Decl.}}$), $\Re$ and $\Im$ are the real and imaginary components of the original visibilities, and $\Re'$ and $\Im'$ are their reprojected counterparts.

*Azimuthal binning*: we averaged visbilities in bins of equal size in projected baseline $(u^2 + v^2)^{1/2}$. For the highest signal-to-noise data, we chose 40 bins at 1 mm and 20 bins at 3 mm; we chose fewer bins for protostars with lower signal-to-noise, in order to reach a consistent level of signal-to-noise, always using twice as many bins at 1 mm as at 3 mm.

*Using the real part*: After the above phase recentering step, and confirming that there was not significant extended or asymmetric emission seen in the CLEAN maps, we discarded the imaginary component of the complex visibilities so that only the real part was used. In some interferometric studies, data is fit to models using the combined amplitude of the real and imaginary parts of the visibilities; one downside to this approach is that the mean amplitude in any given bin will always be positive (greater than zero) even in the absence of on-sky signal, as the noise in the real and

imaginary parts would be squared, added, and square-rooted – leading to a positive bias in the high-noise, low-signal limit that makes comparisons to models difficult to accurately quantify. In the present case, the models are by their nature spherically symmetric, so their imaginary part in visibility space will be zero by construction; an apples-to-apples comparison would be skewed by using a biased metric.

### 3.6.3 Fitting

We evaluate our two-component physical model by computing a $\chi^2$ as follows:

$$\chi^2 = \sum_{\nu}^{\mathrm{SED}} \frac{\left(S_{\nu,\mathrm{obs}} - S_{\nu,\mathrm{model}}\right)^2}{\sigma_{S_\nu}} + \sum_{\nu}^{\mathrm{bands}} \sum_{uv-\mathrm{dist}}^{\mathrm{bins}} \frac{\left(\bar{I}_{\nu,\mathrm{obs}}(uv) - I_{\nu,\mathrm{model}}(uv)\right)^2}{\sigma_{I_\nu}} \tag{3.4}$$

where $S_\nu$ is the integrated flux density (Jy) at a given frequency $\nu$, $\bar{I}_\nu(uv)$ is the flux density (Jy) within a given azimuthally-averaged bin in $u, v$ space, and $\sigma_{S_\nu}$ and $\sigma_{I_\nu}$ are the uncertainties on those measurements. The SED part of the $\chi^2$ is summed over all observed wavelengths, while the visibility part is summed over all $u, v$ bins in each observed wavelength band (1 mm and 3 mm).

To sample the posterior probability distribution for these five model parameters, we use `emcee` (Foreman-Mackey et al., 2013a,b), a Python-language implementation of the affine-invariant MCMC sampler designed by Goodman & Weare (2010). We use a log-likelihood function $\ln \mathscr{L}$ in the MCMC fitting:

$$\ln \mathscr{L} = K - \frac{1}{2}\chi^2 \tag{3.5}$$

which is maximized by the MCMC procedure.

For each protostar, we ran 20 MCMC walkers in chains of length $\sim 500 - 800$, leading to $> 10,000$ model evaluations per protostar. The typical autocorrelation time $\tau$ for each parameter ranged from 25–65 steps. We discarded the first 50–200

Table 3.2. Derived protostar source properties

| Source Name | $L_*$ ($L_\odot$) | $M_{\rm env}$ ($M_\odot$) | $p$ ($\rho \propto r^p$) | $F_{\rm c,3mm}$ (mJy) | $F_{\rm c,1mm}$ (mJy) |
|---|---|---|---|---|---|
| L1455 IRS1 | $5.75^{+0.22}_{-0.23}$ | $0.78^{+0.05}_{-0.06}$ | $-1.82^{+0.03}_{-0.03}$ | $2.47^{+0.21}_{-0.20}$ | $14.01^{+2.46}_{-2.36}$ |
| B1-a | $0.77^{+0.18}_{-0.14}$ | $0.42^{+0.09}_{-0.11}$ | $-1.55^{+0.11}_{-0.17}$ | $1.94^{+0.17}_{-0.15}$ | $14.37^{+1.44}_{-2.02}$ |
| IRAS 03235 | $0.73^{+0.02}_{-0.02}$ | $1.25^{+0.10}_{-0.10}$ | $-1.69^{+0.03}_{-0.03}$ | $7.20^{+0.25}_{-0.26}$ | $102.37^{+2.60}_{-2.22}$ |
| B5 IRS1 | $1.70^{+0.17}_{-0.11}$ | $1.02^{+0.09}_{-0.10}$ | $-1.46^{+0.05}_{-0.05}$ | $1.21^{+0.18}_{-0.16}$ | $23.79^{+1.71}_{-1.69}$ |
| L1455 IRS4 | $1.16^{+0.06}_{-0.06}$ | $1.51^{+0.11}_{-0.13}$ | $-1.35^{+0.03}_{-0.03}$ | $0.14^{+0.11}_{-0.09}$ | $0.37^{+0.54}_{-0.26}$ |

Note. — Best-fit parameters and their quoted plus/minus uncertainties are drawn from the 50th, 84th, and 16th percentiles, respectively, of the MCMC posterior probability distributions.

steps as "burn-in", depending on how quickly the chains for each protostellar model converged. Foreman-Mackey et al. (2013a) discuss various ways to assess convergence in MCMC chains. A general overview of MCMC methods in astrophysics is given by Hogg & Foreman-Mackey (2018).

### 3.6.4 Results

In Table 3.2, we report the results of our physical model fitting using the MCMC method. In Figure 3.5, we show the SEDs and continuum visibilities of each of our five sources, with the best-fit physical source models overplotted. In Figure 3.6, we show an example corner plot showing projections of the posterior probability distribution. It was calculated from the MCMC fitting of the source model to L1455 IRS1's SED and continuum visibility measurements. The additional corner plots are shown in the Appendix.

We derive luminosities of 5.75, 0.77, 0.73, 1.73, and 1.16 $L_\odot$, respectively, for the protostars L1455 IRS1, B1-a, IRAS 03235, B5 IRS1, and L1455 IRS4. Compared to some previously-published luminosity measurements (e.g., Hatchell et al. 2007), these estimates are significantly lower – by nearly a factor 3×, in the case of B5 IRS1. We place the difference in the fact that we use sensitive HGBS photometry

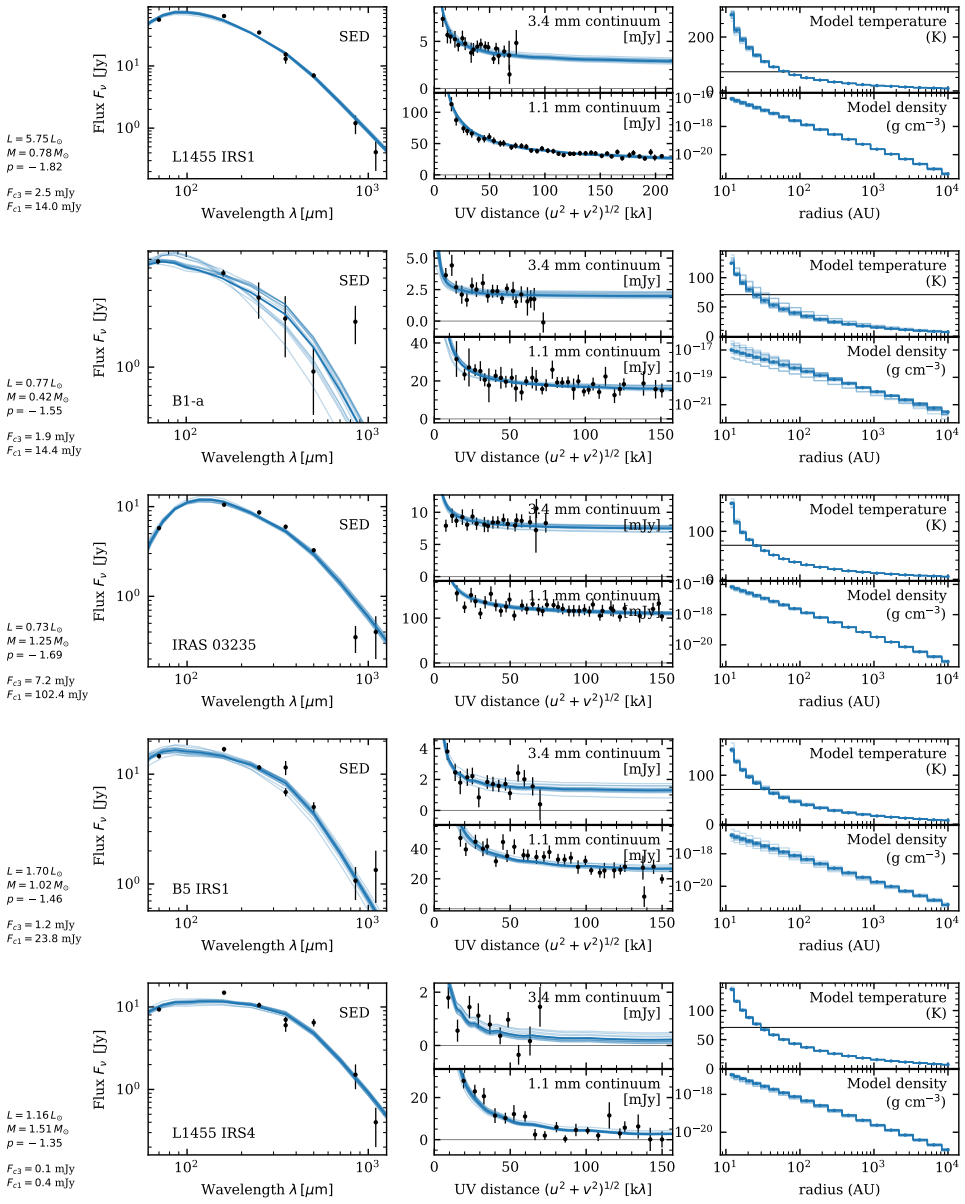


Figure 3.5 Results from physical model fitting. A "best-fit" model is shown for each source (solid blue), plus fifteen representative models (translucent blue) with their parameters randomly drawn from the MCMC posterior probability distribution, to illustrate the range of models consistent with the data.

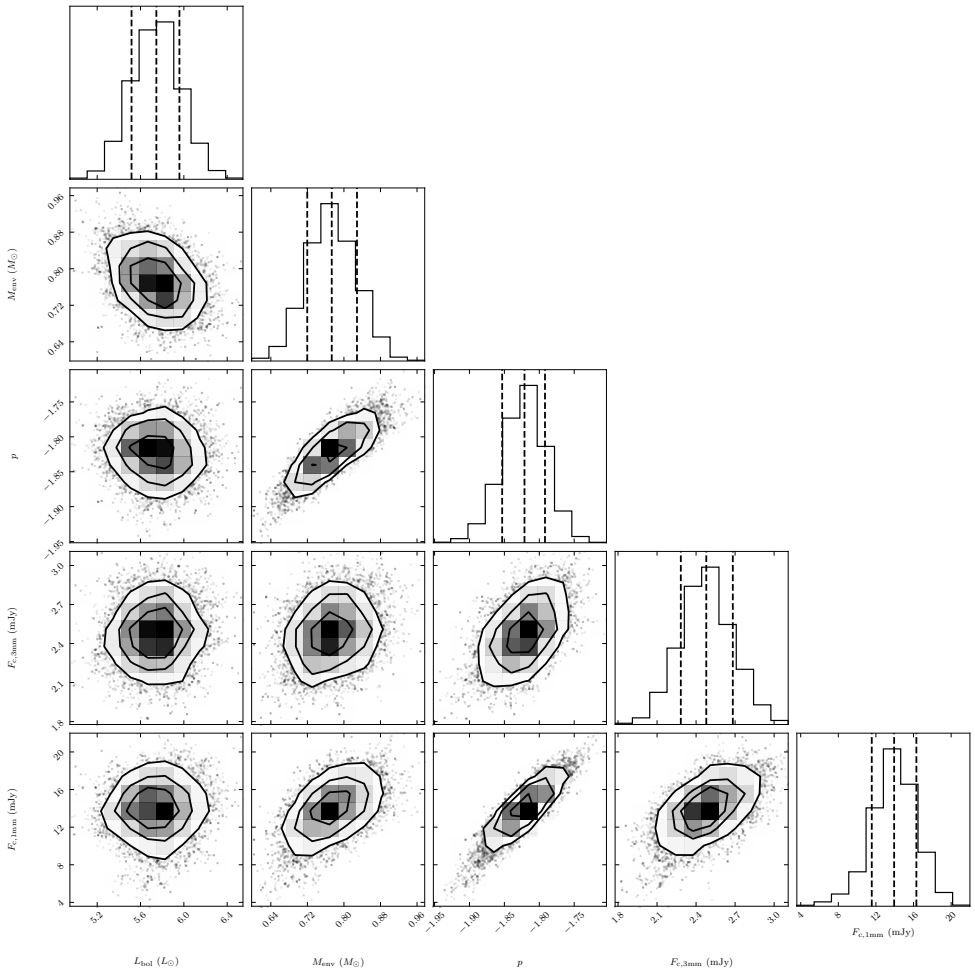


Figure 3.6 An example "corner plot" showing projections of the posterior probability distribution. It was calculated from the MCMC fitting of the source model to L1455 IRS1's SED and continuum visibility measurements. The additional corner plots are shown in the Appendix.

spanning 70–500 $\mu$m; many previous observations in this wavelength regime (e.g., IRAS) could only provide upper limits at some of these wavelengths, and so these other studies were principally constrained by submillimter and millimeter photometric measurements with $\lambda > 450$ $\mu$m. The SED of protostars peaks in this far-infrared regime, and accurate determination of protostellar physical parameters depends on these measurements (as noted by, e.g., Furlan et al. 2016).

We derive envelope masses which range from $0.4 - 1.6$ $M_{\odot}$, with density profiles which have power law exponent $-1.3 < p < -1.85$. These masses are somewhat lower than literature estimates; the envelope mass estimates presented e.g., in Hatchell et al. (2007) are often extrapolated from submillimeter measurements and assume a dust temperature of e.g., 10 K, whereas we use a full radiative transfer model. Additionally, our modeled envelope masses may be lower if the actual envelopes extend beyond 10,000 au, the maximum distance $r_{\rm out}$ we consider in our model.

Our MCMC approach allows us to examine covariances between parameters in the fit. $M_{\rm env}$ co-varies strongly with $p$ for most protostars, which is understandable as a less concentrated (higher $p$) envelope will require more mass overall (higher $M_{\rm env}$). $L_{\rm bol}$ has an anticorrelation with $M_{\rm env}$ which is stronger for some sources than others. This makes sense, as a less-luminous star will be surrounded by cooler dust, which must be increased in number to compensate for the observed flux. We observe covariance between $p$ and each of the $F_{\rm c}$ parameters. A more centrally-concentrated envelope model will require less of a "compact flux component" correction in order to reproduce an observed continuum visibility profile.

For most sources, the parameters are constrained quite well in the MCMC, with uncertainty estimates well below 10%. B1-a, however, stands out; its corner plots (shown in Appendix B) are less well-behaved than the others'. This arises due to a few related issues: as the protostar is fainter than the rest of its cohort, the data in its SED have lower signal-to-noise. Additionally, there is a surprising mismatch between

the 500 $\mu$m and 850 $\mu$m flux, in which the 850 $\mu$m datapoint is nominally much brighter, despite this being impossible in the protostellar model. Possibly relatedly, B1-a is part of the densely packed B1 cluster of protostars, immediately adjacent to sibling sources B1-b, B1-c, and B1-d; therefore, flux extraction is more fraught towards this source than the other sources observed in this study – especially at long wavelengths where the envelopes' emission may begin to blend, requiring careful use of cloud decompositions like CLUMPFIND. As a consequence of these issues, B1-a's nominal SED is less well-behaved, which directly affects the estimated uncertainties in the MCMC model fit. Nonetheless, its inferred model parameters remain informative for the purposes of interpreting our molecular line emission.

## 3.7 Chemical abundance model

We make use of a chemical abundance model, coupled to the physical model derived for each protostar in Section 3.6, to disentangle large-scale line emission from that arising from the hot core. HCN and H$^{13}$CN emission in protostars is typically inconsistent with a constant fractional abundance model (see e.g., Jørgensen et al. 2005a), often requiring both a "drop" abundance going from the outermost envelope to a denser intermediate zone, and a "jump" abundance (analogous to a snowline or iceline) going from the intermediate zone to the warmest parts of the protostellar interior. We make use of such a "drop-jump" abundance model here; in our previous work (Rice et al., 2018), a "jump" abundance explained well many lines of H$^{13}$CN emission at IRAS 16293. From this "drop-jump" chemical abundance profile, combined with the physical model we derived, we solve the molecular level populations and generate sky image cubes, from which we then compute synthetic observations to compare against the IRAM 30m and NOEMA line emission data. The H$^{13}$CN emission from protostar L1455 IRS1 is well-fit by such a model (Fig. 3.7); for the other protostars without NOEMA H$^{13}$CN detections, we use the chemical abundance

model to derive upper limits on the possible hot core HCN abundance.

As a first step, we note that the size of the HCN "jump" abundance region depends only on the temperature profile of each protostellar envelope, which we derived in the previous section. When we adopt a sublimation temperature $T_{\rm jump}$(HCN) = 70 K following Rice et al. (2018), we obtain hot core radii which vary from $20 - 65$ au. This will be critical in interpreting the H$^{13}$CN emission seen at each protostar.

### 3.7.1 Model description

The "drop-jump" chemical abundance model makes use of five parameters, three of which we allow to float. The three floating parameters are the abundances[6]: $X_0$, the "initial" gas-phase abundance, presumed to be typical of the ISM; $X_{\rm D}$, the depleted abundance within the freeze-out zone applicable when $n > n_{\rm de}$ but $T < T_{\rm jump}$; and $X_{\rm in}$, the hot core chemical abundance where $T > T_{\rm jump}$. We fix the following parameters: $n_{\rm de}$, the number density at which the majority of molecules desorb (freeze) onto dust grain surfaces; and $T_{\rm jump}$, the sublimation temperature of the molecule. Jørgensen et al. (2005c) and others discuss the connection between $n_{\rm de}$, the freeze-out timescale of a core, and the lifetime of that core. We fix $n_{\rm de} = 8 \times 10^5$ cm$^{-3}$. $T_{\rm jump}$ is related to the binding energy of the molecule such that $T_{\rm jump} \simeq \frac{E_{\rm B}/k}{57}$ under typical molecular cloud conditions; see Hollenbach et al. (2009) and Rice et al. (2018, Chapter II) for further discussion. We fix $T_{\rm jump} = 70$ K following Rice et al. (2018, Chapter II).

To solve the molecular energy level populations given a non-LTE, radiation-rich environment, we use RATRAN (van der Tak & Hogerheijde, 2007), which considers spherical shells of independent temperature, density, molecular abundance, and radial velocity. RATRAN implements an Accelerated Monte Carlo technique for solving these level populations, making use of HCN collisional rates from Dumouchel et al.

[6]Here we use the conventional definition of $X$ as a fractional number abundance relative to $H_2$.

(2010) which are available via the Leiden Atomic and Molecular Database (LAMDA; Schöier et al. 2005). We adopt HCN's rates for $H^{13}CN$. RATRAN also performs ray-tracing to create a datacube of the observed emission, with dimensions (R.A., Decl., $v_{\rm LSR}$).

To compare the model "sky emission" datacubes to our observed data, we use Miriad to perform the necessary transformations that simulate a real observation. For comparison to IRAM 30m spectra, we convolve the model datacube with the appropriate beam, extract the central pixel spectrum, then subtract the continuum. For comparison to NOEMA visibility amplitudes, we subtract the continuum from each velocity channel of the sky datacube, integrate over the velocity axis to create a moment-zero map, multiply the moment map by the primary beam response of NOEMA at the appropriate frequency, compute a 2D Fourier transform of the primary beam-corrected moment-zero map, and finally extract a radial profile from the 2D Fourier transform map.

### 3.7.2 L1455 IRS1 molecular abundance model

As L1455 IRS1 has a strong NOEMA detection, we fit a full chemical model to its data. For the velocity field, we impose a stepwise velocity field in which the velocity dispersion of the hot core $\Delta v_{\rm hotcore}$ matches the NOEMA $H^{13}CN$ $3-2$ line width, the outer envelope velocity dispersion $\Delta v_{\rm outer}$ matches the IRAM 30m $1-0$ line width, and an intermediate value is adopted in the depletion zone where $X = X_{\rm D}$. The chemical abundance model to L1455 IRS1 was fit using `scipy.optimize`.

Below we present the model parameter fits:

$$\begin{aligned} X_{\rm in}(H^{13}CN) &= 5.9 \times 10^{-10} \\ X_{\rm D}(H^{13}CN) &= 1.4 \times 10^{-11} \\ X_{0}(H^{13}CN) &= 2.5 \times 10^{-10} \end{aligned}$$

which correspond to HCN abundances (assuming $^{12}C/^{13}C = 68$; Wilson 1999):

$$\begin{aligned} X_{\rm in}({\rm HCN}) &= 4.0 \times 10^{-8} \\ X_{\rm D}({\rm HCN}) &= 9.5 \times 10^{-10} \\ X_{0}({\rm HCN}) &= 1.7 \times 10^{-8} \end{aligned}$$

In Figure 3.7, we show the result of fitting a chemical abundance model to the H$^{13}$CN line measurements from IRAM 30 m and NOEMA. In this Figure, we also compare the observed HCN $1-0$ visibilities to those which are in the model, but note that the actual fit is only calculated for the H$^{13}$CN lines – the HCN emission is both likely optically thick and not centered on the continuum peak (see Fig. 3.3), unlike the H$^{13}$CN emission.

It can be observed that in this fit, the model under-predicts the flux of the three hyperfine components of H$^{13}$CN $1-0$, while slightly over-predicting the $3-2$ flux. The same phenomenon was seen in Rice et al. (2018) in the analysis of the H$^{13}$CN $1-0$ and $3-2$ lines at IRAS 16293. This likely reflects the presence of extended cloud material beyond the nominal outer radius of 10,000 au which contributes to the observed $1-0$ flux, given that $\theta_{3.4mm} = 29\farcs2$ and the upper-state energy of the $1-0$ transition is only $E_{\rm u} = 4.1$ K. It can also be noted in this fit that the same model which reproduces the compact $3-2$ emission also predicts essentially zero compact $1-0$ emission, consistent with the non-detection of H$^{13}$CN $1-0$ emission in the NOEMA data for this source.

### 3.7.3 Upper limits for the remaining protostars

The remaining four protostars B1-a, IRAS 03235, B5 IRS1, and L1455 IRS4 do not have strongly detected H$^{13}$CN lines with NOEMA. Therefore, we use the physical-chemical model to place upper limits on $X_{\rm in}$(HCN). To do this, we first performed

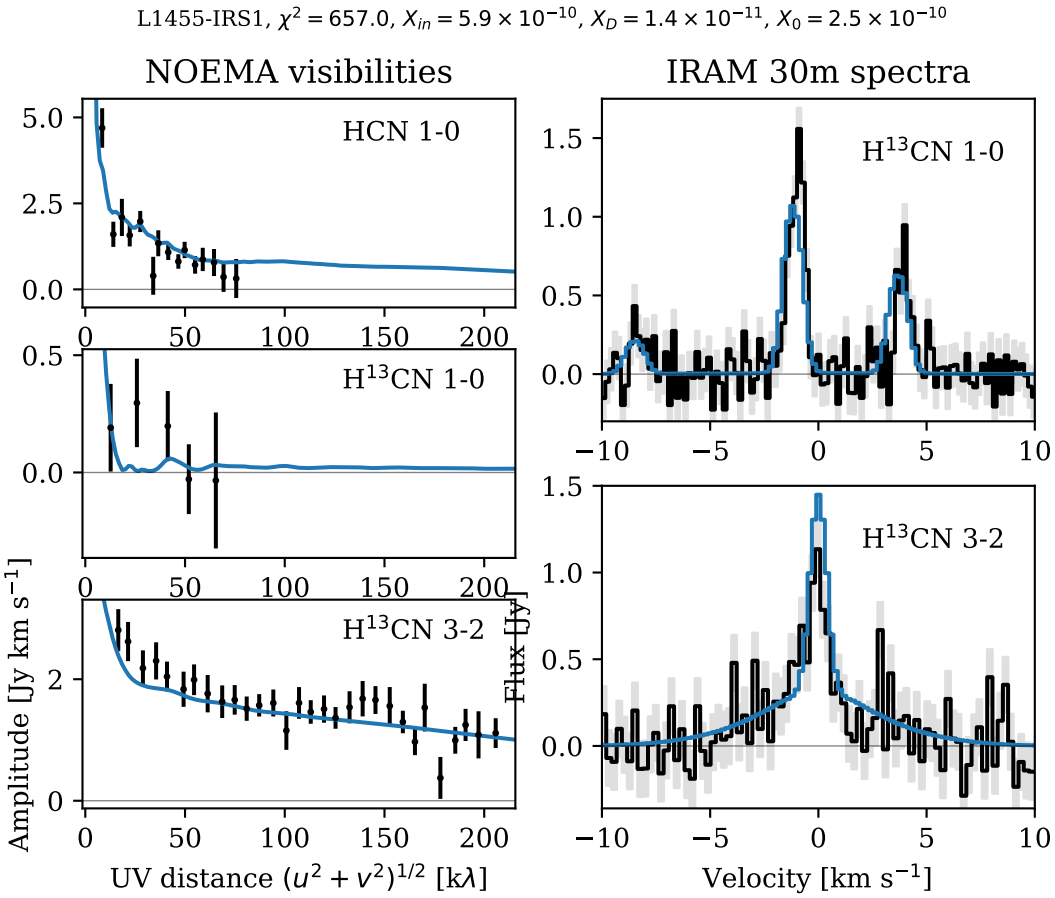


Figure 3.7 The chemical abundance model fit to L1455 IRS1's H$^{13}$CN line measurements.

Table 3.3. Upper limits for flux and $X_{\rm in}$ derived from NOEMA central-pixel spectra

| Source Name | Flux fit $\pm$ 1-$\sigma$ (mJy) | 3-$\sigma$ upper limit (mJy) | Hot corino diameter (AU) | $X$(H$^{13}$CN) upper limit | $X$(HCN)$^b$ upper limit |
|---|---|---|---|---|---|
| L1455 IRS1 | $198.1 \pm 2.1$ | 204.4 | $126 \pm 3$ AU | — | — |
| B1-a | $0.2 \pm 9.2$ | 27.7 | $50 \pm 8$ AU | 4.9(−9) | 3.3(−7) |
| IRAS 03235 | $-3.8 \pm 10.5$ | 28.2 | $51 \pm 1$ AU | 5.0(−9) | 3.4(−7) |
| B5 IRS1 | $8.5 \pm 7.2$ | 30.1 | $70 \pm 4$ AU | 5.8(−10) | 3.9(−8) |
| L1455 IRS4 | $32.7 \pm 10.5^a$ | 64.4 | $60 \pm 1$ AU | 6.7(−10) | 4.6(−8) |

Note. — Flux upper limits were derived by using MCMC to fit a Gaussian with the same linewidth as L1455 IRS1 to each protostar's spectrum. The number in parentheses is the order of magnitude, i.e., 2.0(−5) denotes $2.0 \times 10^{-5}$. $^a$ — the flux at L1455 IRS4 is not bright enough to constrain both its intensity and its linewidth with confidence, so we do not treat it as a confident detection. $^b$ — We assume a standard $^{12}$C/$^{13}$C ratio of 68 (Wilson, 1999).

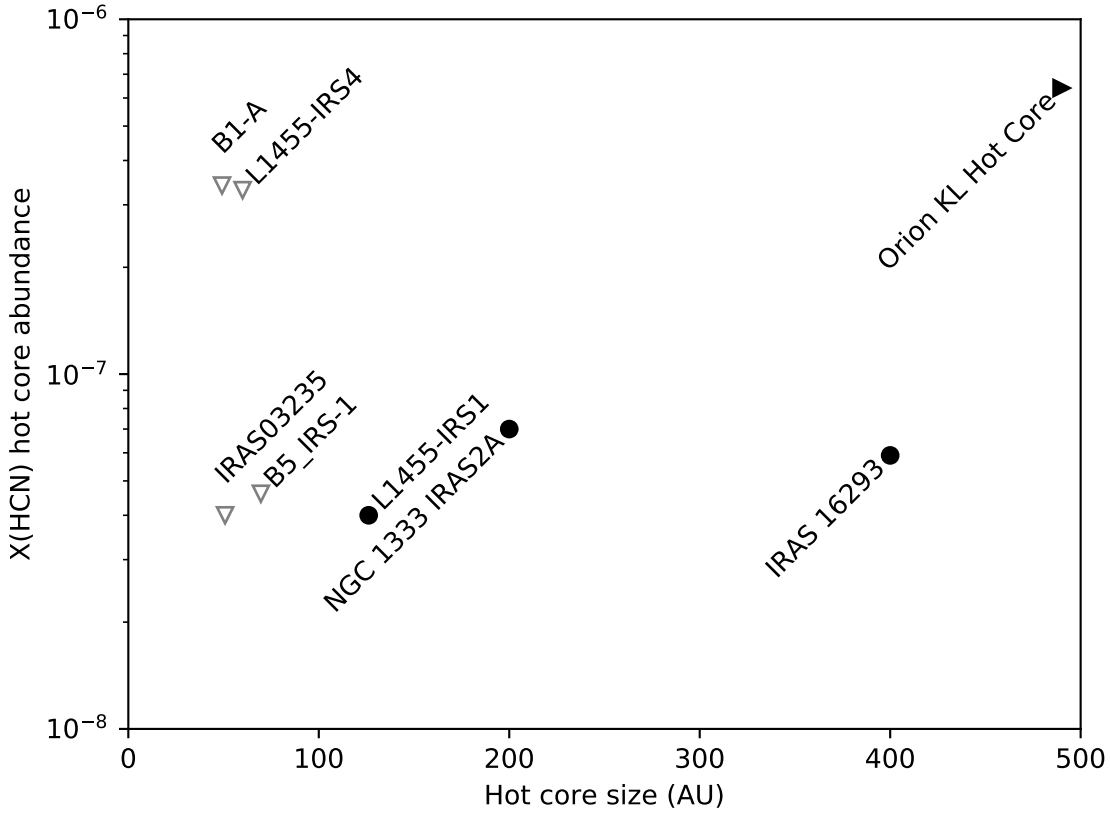


Figure 3.8 The X(HCN) measurements and upper limits presented in this paper. Upper limits are denoted with a downward-pointing triangle (▽). Also shown are X(HCN) measurements from NGC1333-IRAS2A (Brinch et al., 2009a), IRAS 16293-2422(Rice et al., 2018), and Orion KL (Crockett et al., 2014b). The rightward-pointing triangle (▶) of Orion KL indicates that its diameter is much higher (4200 au) than can be shown on the plot.

a simple Gaussian fit to the $3-2$ line seen at L1455IRS1, to derive its line center and FWHM line width. Then, to answer the question "how bright could a hot core be and still remain un-detected in this data?", we fit each protostar's $3-2$ line with a simple Gaussian, obtaining a posterior probability distribution from MCMC fitting. Using `emcee`, we ran 10 walkers $\times$ 12,000 steps to explore the posterior parameter distribution for a single parameter: the flux of this Gaussian line. A 3-$\sigma$ upper limit on that flux was achieved by taking the 99.865th percentile of the posterior probability distribution. We then fit a hot-core-only abundance model to the Gaussian with that flux value, in order to derive the 3-$\sigma$ upper limit on the hot core $X_{\rm in}(\rm H^{13}CN)$ abundance. This abundance model uses that star's particular physical structure (density and temperature profile) model derived here in Section 3.6.

The flux upper limits for these four protostars range from 28–64 mJy. These flux upper limits, when interpreted in the context of each protostar's unique physical model, correspond to $X_{\rm in}(\rm H^{13}CN)$ values from $5.8\times10^{-10}$ to $5.0\times10^{-9}$, or $X_{\rm in}$(HCN) values from $3.9\times10^{-8}$ to $3.4\times10^{-7}$ In Table 3.3, we report the upper limits on fluxes from the NOEMA $\rm H^{13}CN$ $3-2$ central-pixel spectrum, as well as the corresponding hot core HCN abundances. The upper limits on $X_{\rm in}$(HCN) for the two faintest protostars, B1-a and IRAS 03235 (each $L_{\rm bol}\sim0.75\ L_\odot$), are an order of magnitude above $X_{\rm in}$ we measure for L1455 IRS1, and so are unfortunately un-informative. The upper limits on the remaining two protostars, B5 IRS1 and L1455 IRS4, though, are approximately equal to L1455 IRS1's hot core abundance. This weakly suggests that fainter and/or more evolved protostars do not have HCN hot core abundances that exceed moderately bright Class 0 protostars, but this is not a strongly supported statement given the small number of sources under consideration.

## 3.8 Discussion

### 3.8.1 Connections between single-dish and interferometric line measurements

The five protostars in this study have similar single-dish fluxes of the $H^{13}CN$ $3-2$ and $1-0$ lines, yet only L1455 IRS1 shows bright or even modest $H^{13}CN$ emission on small scales as probed by the NOEMA interferometer. To probe whether *any* single-dish observations could be used to identify a low-mass hot core, we have compared our results to the following single-dish studies.

Our sample of five sources was also observed at IRAM 30m by Graninger et al. (2016), Bergner et al. (2017), and Law et al. (2018) alongside 11 other protostars in their sample. In these studies, the authors made measurements of a variety of transitions (typically with upper-state energy $E_u/k < 40$ K) of complex organic molecules including the simple carbon chains butadiynyl ($C_4H$) and propynylidyne ($l-C_3H$), methanol ($CH_3OH$), ketene ($CH_2CO$), acetaldehyde ($CH_3CHO$), dimethyl ether ($CH_3OCH_3$), methyl formate ($CH_3OCHO$), the sulfur-bearing species dicarbon monosulfide (CCS) and tricarbon monosulfide (CCCS), and the nitrogen-bearing species methyl cyanide ($CH_3CN$), isocyanic acid (HNCO), cyanoacetylene ($HC_3N$), and cyanobutadiyne ($HC_5N$). When considering the measurements of these molecules, L1455 IRS1 does not stand out in any way among the sixteen observed sources. Bergner et al. (2017) rank the sources in terms of line richness, ranking B1-a, B5 IRS1, L1455 IRS4, L1455 IRS1, and IRAS 03235 first, sixth, seventh, eighth, and 11th (respectively) in line richness among the 16-protostar sample. These comparisons indicate that single-dish measurements of low-$E_u$ lines cannot reveal the presence of a hot corino, no matter how complex the organic species are: cold and lukewarm chemistry in interstellar clouds and the circumstellar envelope are sufficient to produce many of these species (such as carbon chains and complex organic molecules) without the

presence of a hot corino.

In contrast, a more promising approach to single-dish hot corino detection is surveys which sensitively probe many lines with $E_u/k \gtrsim 100$ K (as originally noted by Schöier et al. 2002 when introducing the jump abundance model) and which are able to distinguish between narrow and broad lines. A good example is the study of Cep E-mm, a newly identified intermediate-mass protostellar hot core, carried out by Ospina-Zamudio et al. (2018) using IRAM 30m and NOEMA. Ospina-Zamudio et al. identified three kinematic components in their data towards Cep E-mm, with the "broad-line" component consisting of (a) emission which peaks at the source systemic velocity, (b) line width which varies little with $E_u$, and (c) it is detected in the high excitation lines of methanol and other species, with $E_u$ in the 100–500 K range. Their interferometric maps confirmed that the broad-line component was indeed from a hot core, with NOEMA capturing essentially all the flux from high-$E_u$ methanol transitions seen in the single-dish spectrum. They also noted that emission from the complex organic nitrogen carriers $CH_3CN$ and $C_2H_5CN$ was particularly associated with this broad-line/hot core component. This mirrors conclusions from Crockett et al. (2015)'s study of the high-mass hot core at Orion KL, in which complex organic nitrogen carriers (especially $CH_3CN$, HNC, $C_2H_3CN$, $H^{13}CN$, $HC_3N$, $HN^{13}CO$, and $C_2H_5CN$) selectively traced hot gas, with a significant fraction of emission ($\sim 5-20\%$) arising from states $E_u > 800$ K, a situation not seen for the nitrogen-free organics, including the oxygen-bearing species $CH_3OH$ and $CH_3OCH_3$.

A similar scenario was observed at IRAS 16293: interferometric measurements by Bisschop et al. (2008) identified small-scale HNCO and $CH_3CN$ emission from the brighter binary member IRAS 16293-A, with rotational temperatures in excess of 200 K. Bisschop et al. note in particular the importance of a combined single-dish plus interferometric $u, v$ analysis of line emission to disentangle small, hot emission from broad, cold emission, pointing out, for example, that cold HNCO emission would

have been missed without a $u, v$ analysis. Also towards IRAS 16293, Caux et al. (2011) divided lines into 4 kinematical behavior categories; their "Type II" kinematic behavior included N- and S- bearing species (including nitrogen carriers HCN, $HC_3N$, and HNC) which showed broad line widths (up to 8 km $s^{-1}$) and energies $E_u/k$ up to 250 K; they associated these species with the brighter hot corino source IRAS 16293-A. Thus, high-$E_u$ observations of complex nitrogen-bearing species may prove particularly fruitful in identifying hot cores from single-dish and interferometric data; it remains to be seen whether nitrogen species show this behavior systematically in low-mass hot cores.

In the context of the present work, it bears noting that of the five protostars studied, only L1455 IRS1 appears to have a broad component in its $H^{13}CN$ $3-2$ emission, in addition to the narrow component all five protostars share; while their peak $T_{\rm mb}$ fluxes are all comparable, L1455 IRS1's $3-2$ flux integrated over its entire velocity extent is much brighter than in the other four targets.

### 3.8.2 HCN emission in hot cores

In this work, we have presented one strong detection of compact $H^{13}CN$ $3-2$ emission arising from a protostellar hot core, and four non-detections of that same emission line towards other protostars. An immediate question that emerges from this result: is HCN emission from protostellar hot cores so rare that this result could have been expected? Jørgensen et al. (2007b), in the PROSAC survey, completed a similar interferometric molecular line survey of low-mass protostars; among eight studied objects, only one showed clear signs of $CH_3OH$ hot core emission, with $CH_3OH$ and $H_2CO$ emission from the other seven protostars arising only from collimated and shocked outflows, infalling motion, and the larger envelope. That hot core, NGC 1333-IRAS2A, is indeed one of the few other low-mass protostars with a small-scale $X$(HCN) abundance measurement (Brinch et al., 2009a).

In this study, our physical structure model gives us the ability to connect the detection or non-detection of a hot core with the radius of the warm $T > 70$ K region. These sizes are presented in Table 3.3, with radii 25–63 au, i.e., diameters 50–126 au. The detected hot core of L1455 IRS1 has a nominal diameter of 126 au in this model, while the other four protostars have diameters $50 - 70$ au. This relationship arises from L1455 IRS1's notably higher luminosity $L_{\rm bol} = 5.8 \pm 0.2\ L_{\odot}$, with the other protostars' luminosities in the range $0.7 - 1.7\ L_{\odot}$. In Figure 3.8, we show our $X$(HCN) measurements and upper limits in context with other protostellar HCN measurements from NGC1333-IRAS2A, IRAS 16293-2422, and Orion KL (Brinch et al., 2009a; Crockett et al., 2014b; Rice et al., 2018). The primary trend visible in this is that our ability to detect a hot core is strongly dependent on the size of that hot core, which is itself principally a function of the protostellar luminosity. Given this, we cannot state with certainty whether there are variations in the hot-corino HCN abundance, and thus the HCN ice abundance on dust grains. This trend of hot core size (and therefore, ease of detection) versus protostellar luminosity was noted as early as Maret et al. (2004), who presented a nearly identical analysis of predicted hot corino sizes for a sample of Class 0 low-mass protostars, calculated at $T = 100$ K and 50 K, noting radii from 13–133 au for $T = 100$ K and from 50–266 au for $T = 50$ K.

Finally, another important parameter is the choice of sublimation temperature $T_{\rm jump}$ chosen for the molecular species in question. This parameter depends on the binding energy, $E_{\rm B}$, of the molecule to astrophysical dust grain surfaces (Hollenbach et al., 2009), and is moderated by other layers of ice already present on those grains (Viti et al., 2004); due to this, and the fact that not all molecular binding energies are easy to measure in laboratory settings (HCN being a difficult example), the choice of $T_{\rm jump}$ can introduce further uncertainty to this picture. In Rice et al. 2018 (Chapter II), we investigated this issue for HCN and measured $T_{\rm jump} = 71 \pm 3$ K, though noting that uncertainties in the physical structure of IRAS 16293 could bias these

results.

### 3.8.3 Hot core geometry

Subsequent investigations into physical and chemical structure of protostars have continued to call into question the usefulness of the hot core model for the majority of low-mass protostars; for example, Visser et al. (2013) find that even at NGC 1333-IRAS2A, a spherically symmetric emission model cannot reproduce water abundances. Kristensen et al. (2017), in an investigation of water emission towards 24 low-mass protostars, invoke a number of physical components such as cavity shocks, outflows, a disk wind, and spot shocks to reproduce observed warm $H_2O$ emission, none of which align with a simple hot core evaporation model.

Young, embedded disks – the immediate precursors to the protoplanetary disks seen around Class II objects – may be an alternative source for the observed compact molecular emission, instead of a roughly spherical hot core. These disks are becoming more common to detect in high-resolution continuum observations of protostars (see, e.g., Segura-Cox et al. 2016, 2018; Lee et al. 2019; Sakai et al. 2019). In a sample of five Class 0 low-mass protostars, Persson et al. (2016) note that spherically symmetric envelope models fail to reproduce observed single-dish and interferometric emission, and discuss the necessity of a disk component in interpreting such data. van 't Hoff et al. (2018) present an in-depth analysis of disk midplane molecular emission at L1527, a borderline Class 0/I object. They were able to separate disk emission from envelope emission kinematically, and using a 3D model were able to interpret CO isotopologue observations.

Nonetheless, while we include compact (disk-like) continuum emission in our physical models (Section 3.6), the molecular line data presented in this chapter themselves do not rule out a simple hot core or require a molecule-bright disk. Further observations (e.g., with ALMA) will prove useful in resolving this confusion.

## 3.9 Conclusions

From our analysis of IRAM 30m and NOEMA observations of $H^{13}CN$ emission on large and small scales towards five low-mass protostars, and the physical and chemical modeling we performed to interpret these observations, we present the following conclusions:

1. In our sample of five protostars, all have comparable $H^{13}CN$ $1-0$ and $3-2$ flux as seen by IRAM 30m, but only L1455 IRS1 had strong detectable $3-2$ emission at NOEMA.

2. We have constrained the physical structure of the envelopes of these protostars through modeling their SEDs and continuum visibilities, and constrained the flux that could arise from a compact disk component towards each of them.

3. The hot core abundance of L1455 IRS1, derived using the above-described physical model as well as a three-component chemical abundance model, is $4.0\times10^{-8}$, a value within 50% of IRAS 16293.

4. Given the non-detections of small-scale $H^{13}CN$ emission at the other four protostars, we have inferred upper limits on their HCN abundances on small scales.

5. The detectability of small-scale hot corino emission from low-mass protostars depends much more strongly on their luminosity and the size of their hot corino than it does the flux of those lines as seen by single-dish telescopes, confirming that single-dish measurements of low-energy lines ($E_u/k \lesssim 50$ K) cannot be extrapolated to small scales without supplementary interferometric observations.

6. Finally, we discuss complications with the "hot core" model of small-scale warm molecular emission, and outline a path forward for future observations probing organic nitrogen chemistry towards low-mass protostellar hot cores.

# CHAPTER IV

# L1455-IRS1: A Class 0 Protostellar Binary with a Tentative Disk that is Warm and Rich in Organics

## 4.1 Preface

This work is planned to be submitted for publication, with co-authors Edwin A. Bergin and Jes K. Jørgensen.

## 4.2 Abstract

The physical conditions of embedded protostars are highly uncertain on small ($\lesssim$ 200 au) scales, which complicates the retrieval and analysis of chemical abundances. We have obtained high resolution ($0\farcs19 \times 0\farcs24$, or $\sim$50 au) ALMA observations towards L1455 IRS1, a low-mass protostar with a hot core. In the ALMA Band 6 ($\sim$ 250 GHz) data, the CS $5-4$ line shows both large and small-scale structure and kinematics, including the presence of a $\gtrsim$ 100 au compact rotating component. Small-scale $CH_3OH$ and $H^{13}CN$ emission shows rotation in the same sense; meanwhile, ALMA measurements of SiO and SO indicate an outflow which runs perpendicular to this rotation, suggesting that CS, $CH_3OH$, and $H^{13}CN$ trace a tentative disk in Keplerian orbit around a 0.5 $M_\odot$ central mass. Our data confirm L1455 IRS1's binarity and add to the evidence for a protostellar disk, with the tentative disk centered

on the fainter binary companion L1455-IRS1 B. Complementing the ALMA data is a 1.″4 NOEMA observation of 8 lines of methyl cyanide ($CH_3CN$) with energy states spanning $E_u/k = 92 - 442$ K, as well as a large number of transitions arising from other complex organics. Using an LTE, MCMC model of the $CH_3CN$ spectrum, we constrain the temperature of its hot gas ($T_{\rm rot} = 165 \pm 10$ K). We discuss the implications of these measurements, which suggest the presence of a warm, still-accreting disk orbiting a low-mass protostar instead of (or in addition to) a classic spherical "hot core."

## 4.3 Introduction

The chemistry in low-mass protostars may hold the key to understanding the connections between protoplanetary disk chemical processing and the chemical heritage of the interstellar medium. Protostars thus offer valuable information on the initial chemical conditions of planet formation. Spherically-symmetric protostellar physical and chemical models are very helpful in interpreting continuum and line emission from protostellar envelopes, especially from their hot cores (Cazaux et al., 2003) which serve as a key link between the chemistry of the interstellar medium and of protoplanetary disks (Jørgensen, 2011). This modeling approach typically uses the continuum SED to constrain the physical structure of the $r \gtrsim 10{,}000$ au protostellar envelope, which is then used to model the molecular excitation conditions and perform radiative transfer. This approach has been fruitfully applied in many studies to unlock the chemical abundances seen in low-mass protostellar envelopes (e.g., Schöier et al., 2002; Cazaux et al., 2003; Maret et al., 2004; Jørgensen et al., 2005c; Coutens et al., 2012). On small scales ($\sim$ 100s of au), however, the accuracy of these 1-D models seems to break down both for line and continuum measurements, and the physical and chemical structure becomes uncertain (Visser et al., 2013; Persson et al., 2016).

One way to deal with this issue directly is to acquire high-resolution data and reduce the need for inference from models. In recent years this has been increasingly possible with the Atacama Large Millimeter/submillimeter Array (ALMA). A number of observational programs have been carried out to probe the chemistry and physics of the youngest protostellar envelopes and disks, greatly increasing our knowledge of these chemically-rich, still-forming systems, including IRAS 16293 (Jørgensen et al., 2016), HH 212 (Codella et al., 2016; Lee et al., 2019), L1527 (Sakai et al., 2014; van 't Hoff et al., 2018), and L483 (Oya et al., 2017; Agúndez et al., 2019), among others. These high-resolution studies also allow for validation and correction to the 1-D modeling approach where high resolution is not always available; e.g., by serving as a template to interpret emission towards other sources.

In the absence of high spatial resolution, another way to manage the uncertainty of models is to observe a large number of transitions which sample hundreds of K in temperature. Very hot ($T > 150$ K) gas can only exist close to the star; by studying molecular emission originating from this gas, we can reveal gas properties that are otherwise hidden in the SED due to the dust optical depth at $\lambda \sim 1 - 60$ $\mu$m. Prototypical examples of this approach include *Herschel* studies of bright, chemically rich star-forming regions such as Orion KL (Bergin et al., 2010), Sgr B2 (Neill et al., 2014), and the various targets of the CHESS program (Ceccarelli et al., 2010). Ground-based studies such as the IRAM-30m TIMASSS (Caux et al., 2011) also fruitfully deployed this approach. Typically, this approach requires large investments in observing time, and can suffer from issues of different beam sizes across the large span of wavelengths observed, which thus do not necessarily probe the same material, as well as calibration issues in making the different observed bands consistent. One class of molecule allows us to avoid these issues: the symmetric tops, best represented by ammonia ($NH_3$), propyne or methyl acetylene ($CH_3CCH$), and acetonitrile or methyl cyanide ($CH_3CN$). These molecules not only have a large number of transitions of different

upper-state energy $E_u/k$ packed tightly in frequency space (maximizing use of observing time and resources, as well as minimizing calibration issues), but also, because of quantum selection rules, they allow for direct kinetic temperature determinations even outside of LTE (Ho & Townes, 1983; Loren & Mundy, 1984; Askne et al., 1984; Bergin et al., 1994). They are thus regarded as the gold standard of temperature probes in the molecular interstellar medium.

$CH_3CN$, in particular, has enjoyed long use as a temperature probe for hot cores, especially the classic high-mass hot cores in Orion (Loren & Mundy, 1984; Crockett et al., 2014b, 2015). More recently, it has seen common use as a temperature probe in protoplanetary disks (Bergner et al., 2018; Loomis et al., 2018), and has been studied towards the protostar IRAS 16293 (van Dishoeck et al., 1995; Andron et al., 2018; Calcutt et al., 2018a).

Here, we bring both methods — sub-arcsecond direct observations, and $CH_3CN$ as a temperature probe — to the study of the physical structure and conditions of the low-mass protostar L1455 IRS1. L1455 IRS1 is a low-mass Class 0 protostar in the L1455 cloud in the Perseus star-forming region (Tobin et al., 2016b), which lies at a distance of 235 pc (Hirota et al., 2008). This source has been noted as a close binary with separation $0\farcs28$, or 66 au (Tobin et al., 2016b, 2018) as noted in 8 mm VLA observations and 1.3 mm ALMA observations. The molecular emission and kinematics of L1455-IRS1 were studied in depth by Chou et al. (2016), who noted that the source appears to drive a roughly east-west bi-lobed outflow traced by $^{12}CO$. The source appears to be connected to a filamentary structure to its southwest, through which combined IRAM 30m+SMA observations suggest the protostar may be accreting material from its surrounding cloud. Finally, Chou et al. also noted that on small scales, a north-south velocity gradient in $C^{18}O$ emission appears to trace rotation of a compact $\lesssim 200$ au component which they tentatively label as a disk, though their SMA observations (beam FWHM: $4\farcs54 \times 2\farcs74$) did not have sufficient

resolution to resolve this tentative disk component.

Towards L1455 IRS1, we have obtained high-resolution ($0\farcs2$) measurements of its 1.2 mm continuum as well as a number of molecular lines arising from CS, $CH_3OH$, $H^{13}CN$, SiO, and SO, using ALMA. Using NOEMA, we have also obtained $\sim 1''$ spatial resolution spectral observations covering 8 lines of $CH_3CN$, with detections of lines spanning upper state energies $E_u/k = 92 - 442$ K; a large number of lines from additional complex organics were observed as well. In this paper, we bring both these datasets to bear on better understanding the physical and chemical structure of L1455 IRS1 on small scales. In Section 4.4, we introduce the ALMA and NOEMA data. In Section 4.5.1, we present our analysis of the ALMA data, comparing the structure and kinematics of different carriers to gain physical insight into the system. In Section 4.5.2, we analyze the $CH_3CN$ spectrum using non-LTE and LTE modeling, and derive a temperature and column density. In Section 4.7, we present our conclusions.

## 4.4 Data and Observations

### 4.4.1 Description of ALMA program 2016.1.01387.S

L1455 IRS1 was observed in Band 6 as part of the ALMA project 2016.1.01387.S (P.I.: T. Rice) in Cycle 4. Observations were taken in four execution blocks: once on 2016 November 07, twice on 2017 July 11, and once on 2017 July 12. All four execution blocks included 40 antennas. In the first execution block, the projected baseline lengths were between 18 and 1110 m (15.5−959 k$\lambda$). In the second, third, and fourth execution blocks, the projected baseline lengths were between 16 and 2647 m (14−2289 k$\lambda$). The on-source integration times were between 53.5−55.3 minutes, for a total on-source integration time of 217 minutes. All execution blocks used an identical correlator setup. In three different basebands, lines of $H^{13}CN$, $HC^{15}N$,

$HCO^+$, $CH_3OH$, CS, SiO, and SO were covered, with rest frequencies ranging from $\sim 243-262$ GHz. These spectral windows had bandwidths of 58.59 MHz and resolution of either 61 kHz ($\sim$0.07 km s$^{-1}$) or 122 kHz ($\sim$0.15 km s$^{-1}$). In a fourth baseband, we measured a wide window of continuum emission 1.875 GHz wide, centered at 260 GHz, with resolution 31 MHz per channel. In all four executions, the quasar J0237+2848 was used for bandpass calibration, the quasar J0238+1636 was used for flux calibration, and the quasar J0336+3218 was used for phase calibration.

We made use of the science-ready images and data cubes produced by the ALMA pipeline (Kepley et al., 2016), which were of high signal-to-noise and free from artifacts. The data were delivered by Pipeline Version r39732 (Pipeline-Cycle4-R2-B), using Version 4.7.2 (r39762) of the Common Astronomy Software Applications (CASA) program (McMullin et al., 2007). The final beam was $0\farcs19 \times 0\farcs24$, with a position angle $-20°$.

### 4.4.2 Description of NOEMA program W15AI

L1455 IRS1 was observed on 2015 December 03, 21, and 23 in NOEMA Band 3 as part of NOEMA project W15AI (P.I.: T. Rice). All three tracks included seven antennas. The first track, in "C" configuration, had projected baseline lengths between 14.9 and 239.5 m ($13-207$ k$\lambda$). The second track, in "D" configuration, had projected baseline lengths between 21 and 144 m ($18-124$ k$\lambda$). The third track, in "D" configuration, had projected baseline lengths between 16 and 144 m ($14-124$ k$\lambda$). On-source integration time for the three tracks was 3.8 h, 2.6 h, and 1.9 h, respectively, for a total on-source time of 8.3 h. The spectral configuration included four narrow-band spectral windows, plus the wide-band WideX correlator. Three narrow-band windows were centered on the $H^{13}CN$ and $HC^{15}N$ transitions and one centered on an SiO-v1 shocked gas tracer. These windows had resolution 0.078 MHz (0.09 km s$^{-1}$) to 0.3 MHz (0.36 km s$^{-1}$). The WideX correlator captured a contiguous

3.6 GHz spectral band from 257285 to 260884 MHz at 2 MHz (2.3 km $s^{-1}$) resolution. Calibrators included 0322+222, 0507+179, 3C84, MWC349, LKHA101, 3C454.3, and 0333+321.

The narrow-band correlator could only process data from six antennas, so one antenna's data were excluded from all narrow-band data products. Data were simultaneously fed into the WideX correlator, which could handle all seven antennas. The WideX data products have subsequently higher signal-to-noise; however, the lower spectral resolution (2 MHz, or 2.3 km $s^{-1}$) can dilute narrow lines. NOEMA's most recent wide-bandwidth correlator, PolyFIX, was not yet operational when these observations were taken.

Calibration of these NOEMA tracks was performed at IRAM Grenoble on 2016 April 26−28. We calibrated and reduced these interferometric data using the CLIC and MAPPING programs, also from the GILDAS suite of radio astronomy tools. Continuum $u, v$ tables at 1 mm were extracted from the WideX (3.6 GHz-wide) data products by averaging all line-free channels in visibility space. Emission line $u, v$ tables were then created by subtracting the appropriate averaged continuum. We then created a continuum map and spectral line datacubes using CLEAN. The final beam size was $1\farcs87 \times 0\farcs99$, with a position angle of 11°.

## 4.5 Analysis

### 4.5.1 ALMA data

The ALMA data (shown in Figures 4.1, 4.2, 4.3, and 4.4) show an interesting physical and kinematic structure, with a notable marginally-resolved compact object that shows a north-south velocity gradient. There is not an obviously resolved Keplerian disk present in these data, but the following circumstantial evidence gives support for a tentative interpretation of the compact object as an embedded Keplerian

protostellar disk.

Figure 4.1 shows a large-scale view of the CS $5-4$ line at 244.936 GHz. CS is a traditional tracer of dense gas. In these four panels (created in part using `bettermoments`, a software package developed by Teague & Foreman-Mackey 2018 for the analysis of spectral line maps), the integrated emission, peak flux, line width, and velocity center are shown. In this CS map, a number of physical and kinematic components are seen: the central protostar and its surrounding filamentary envelope are clearly identifiable, with a notable filament extending to the southwest. In kinematic space, the signature of the a large-scale northeast-to-southwest outflow (as seen by Chou et al. 2016) is also seen in the CS velocity field, extending nearly $10''$ in each direction from the central protostar. Another medium-scale velocity gradient runs nearly perpendicular to this outflow-related gradient and is discussed further in the next paragraph.

Figure 4.2 zooms-in on ALMA maps, including the 1.2 mm continuum (top panel). In the continuum map, L1455-IRS1 is clearly resolved as a binary protostar, as previously seen by Tobin et al. (2016b, 2018). The following panels show again the CS $5-4$ line, as well as the $CH_3OH$ $5_{1,4}-4_{1,3}$ line at 243.916 GHz and the $H^{13}CN$ $3-2$ line at 259.012 GHz. The CS velocity field shows an intermediate-scale ($3-5''$) velocity gradient which is aligned with the binary axis, and can be interpreted as the circumbinary rotation of the envelope core. Finally, a north-south velocity gradient in CS is seen centered on Source B. The molecules $CH_3OH$ and $H^{13}CN$, whose emission profiles are highly concentrated around Source B, also show this north-south velocity gradient, which is discussed in following paragraphs.

We also observed the SiO $6-5$ transition at 260.518 GHz, and the SO $7_6-6_5$ transition at 261.844 GHz. Figure 4.3 zooms-in on ALMA maps of SiO and SO, both of which appear to trace an eastbound outflow. This outflow appears to arise primarily from Source B. It does not have an extreme velocity shift (relative to the

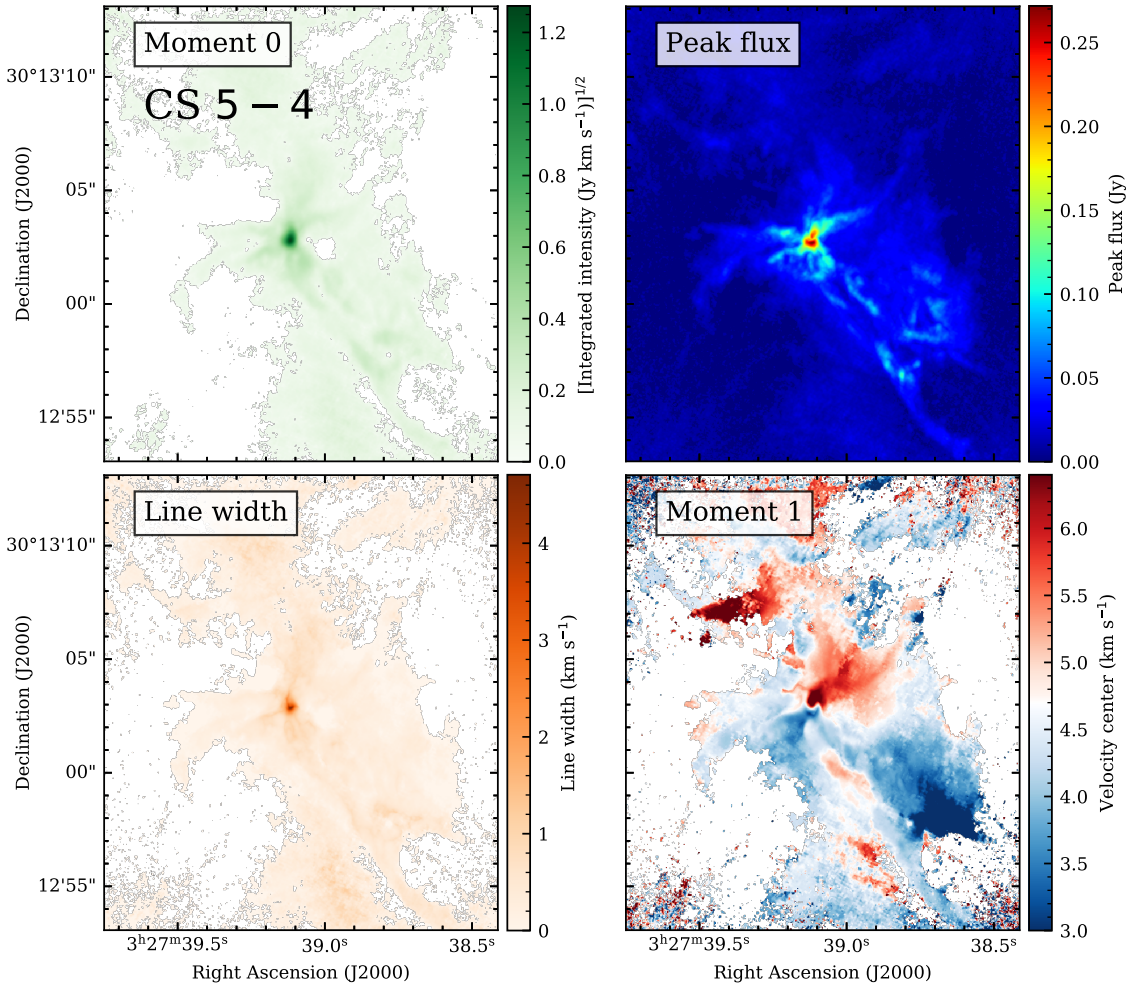


Figure 4.1 ALMA maps of the CS $5-4$ line at 244.936 GHz towards L1445-IRS1. Moments and related maps are computed using the `bettermoments` package (Teague & Foreman-Mackey, 2018). The map size is $20'' \times 20''$, roughly the size of the ALMA primary beam in Band 6 ($\sim 24'' - 25''$) and the maximum recoverable scale of the observations ($18'' - 19''$). Top left: moment-zero integrated emission, displayed with square-root scaling. Top right: Flux of brightest velocity channel along any given line of sight. Bottom left: Line width, computed using the quadratic method of Teague & Foreman-Mackey (2018). Bottom right: First-moment velocity center.

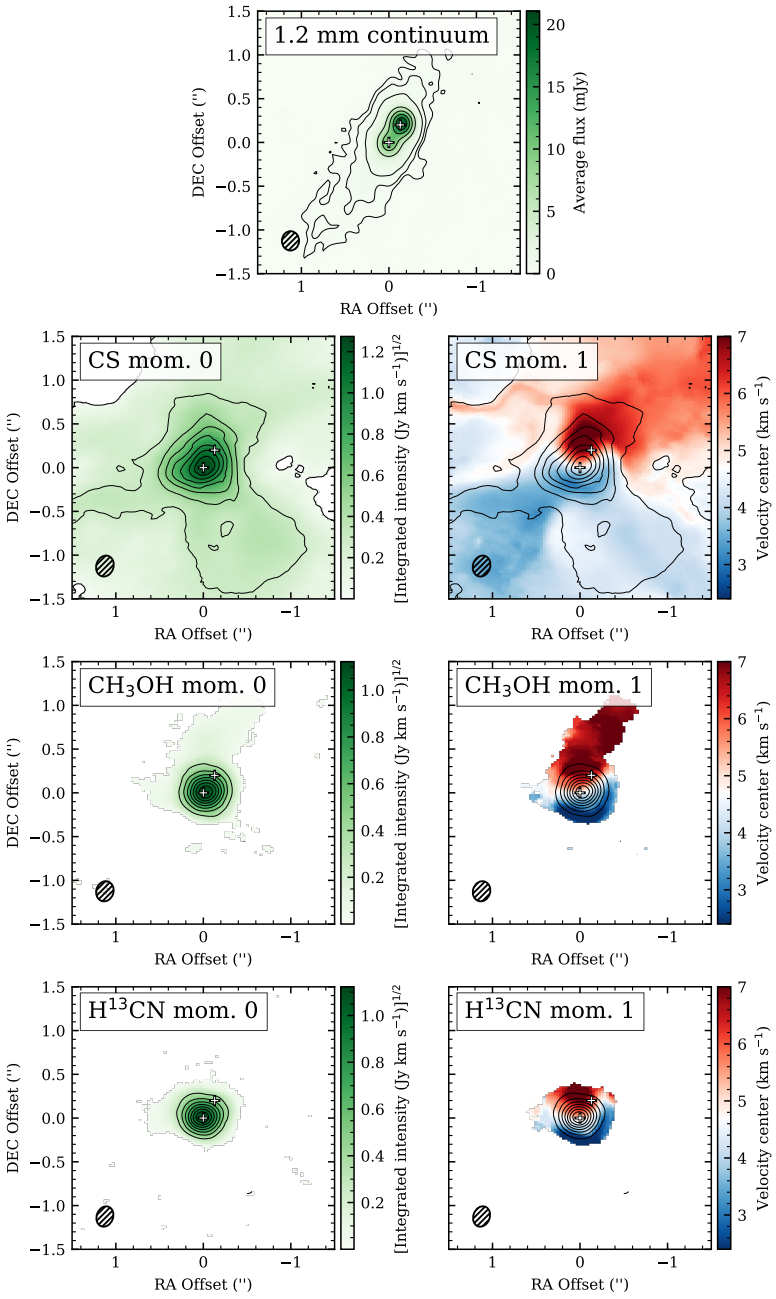


Figure 4.2 Top panel: ALMA map of continuum emission at 1.2 mm. Contours are drawn at 3, 5, 10, 50, 92, 140, and 185 times the noise level. Next six panels: zoomed-in ALMA maps of CS, $CH_3OH$, and $H^{13}CN$. Each map is masked such that emission below 4 times the noise level is hidden. Contours are drawn in increments of 0.125 times the maximum intensity level in the moment-zero map. In all panels, white crosses denote the positions of the two binary members, resolved in the continuum emission. Molecular emission is predominantly centered on Source B, especially for $CH_3OH$ and $H^{13}CN$. In CS, both the circumbinary envelope rotation and the small-scale rotation of a tentative disk are visible; this tentative disk rotation is misaligned from the larger circumbinary rotation. $CH_3OH$ and $H^{13}CN$ show only the small-scale rotation of the tentative disk.

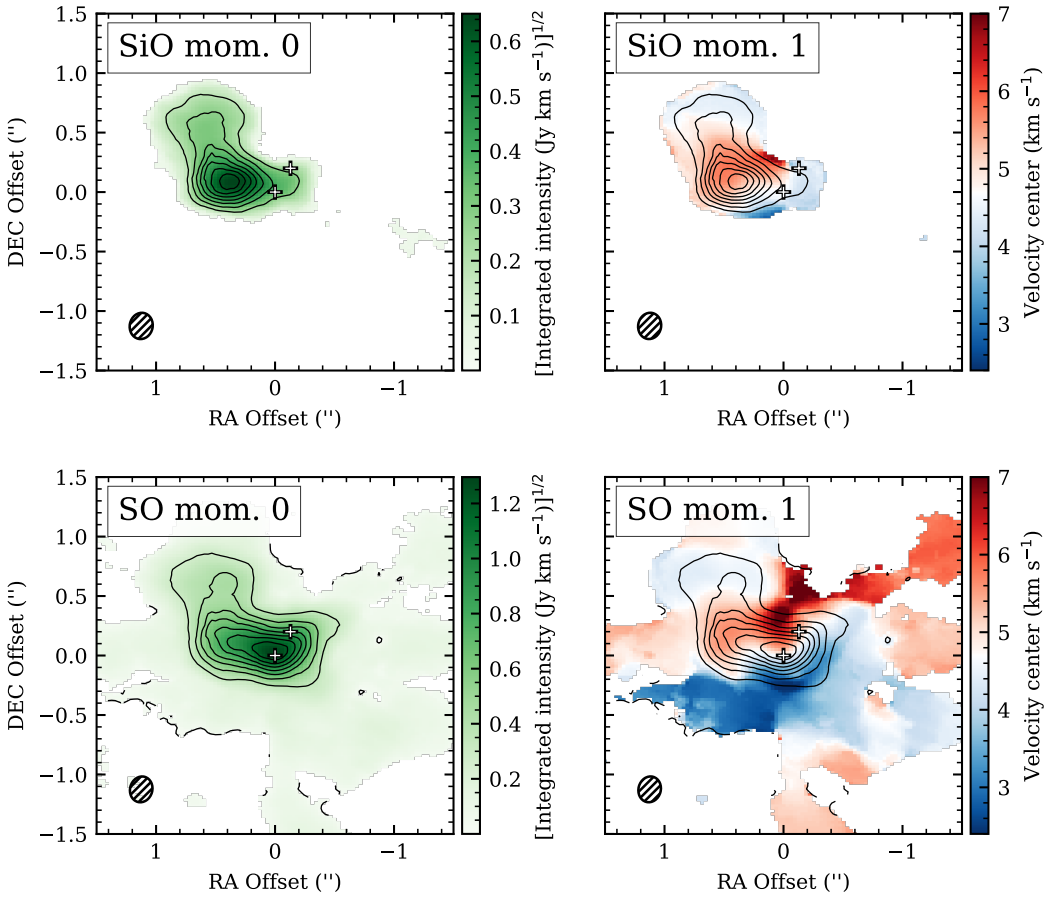


Figure 4.3 Same as Fig. 2, with SiO and SO. Each map is masked such that emission below 4 times the noise level is hidden. Contours are drawn in increments of 0.125 times the maximum intensity level in the moment-zero map. In all panels, white crosses denote the positions of the two binary members, resolved in the continuum emission. Both of these molecules trace an apparent east-west outflow which runs perpendicular to the inferred rotation direction of the tentative disk around Source B.

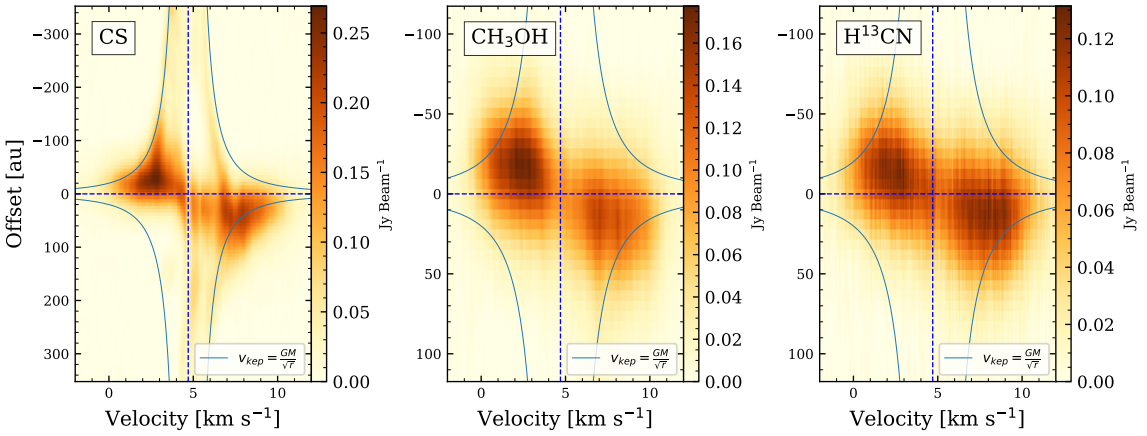


Figure 4.4 Position-velocity plots centered on Source B, extracted along the direction of the velocity gradient seen in $H^{13}CN$ emission. A distance of $d = 235$ pc is assumed in the conversion from arcseconds to au. A Keplerian velocity profile corresponding to a central mass of $M_* = 0.5 M_\odot$ is shown in blue in each plot. Note that the CS plot is zoomed-out to show a larger spatial extent. All three molecules appear to trace the same rotation, with CS tracing this rotating body on larger scales than $CH_3OH$ or $H^{13}CN$.

magnitude of the north-south velocity gradient), and it is effectively perpendicular to the north-south velocity gradient; hence, an outflow originating in a disk surrounding Source B appears likely.

Figure 4.4 shows position-velocity profiles, centered on Source B and along the direction of the compact velocity gradient, for CS, $CH_3OH$, and $H^{13}CN$. A Keplerian velocity curve corresponding to an 0.5 $M_\odot$ central mass is shown, and it appears to define the PV diagram for CS while being consistent with the smaller-scale PV behavior of $CH_3OH$ and $H^{13}CN$.

L1455-IRS1 is a binary protostellar source embedded in an interesting physical environment. Overall, there appears to be evidence consistent with a large-scale bi-lobed outflow and a southwestern filament (both noted previously by Chou et al. 2016), intermediate-scale circumbinary envelope rotation traced by CS, a small-scale one-lobed outflow traced by SiO and SO, and a tentative disk traced by CS, $CH_3OH$, and $H^{13}CN$ which may be in Keplerian rotation. The following analysis investigates the chemical and physical properties of the gas which is present in this tentative disk.

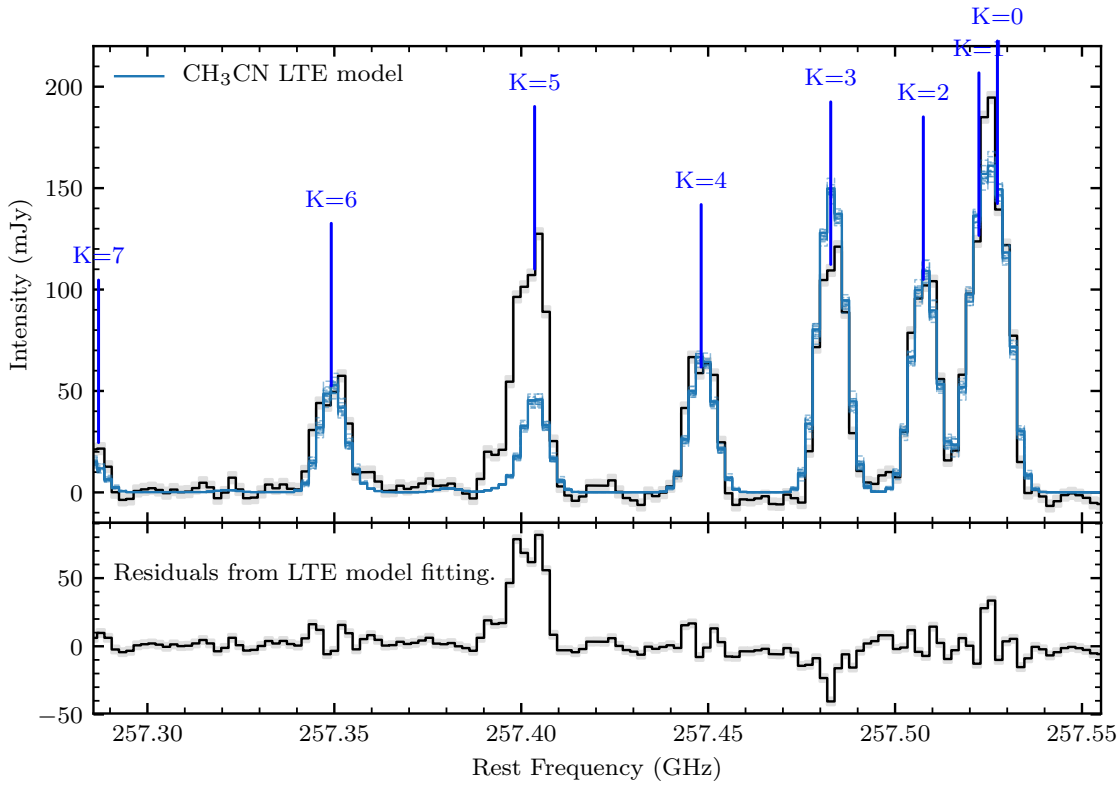


Figure 4.5 The NOEMA WideX spectrum of $CH_3CN$ emission, with an LTE model fit overlaid. A $CH_3OH$ line blend at 257.402 GHz contaminates the $K = 5$ $CH_3CN$ component at 257.404 GHz. The model indicates a gas temperature of $T_{\rm rot} = 165^{+12}_{-10}$ K.

### 4.5.2 NOEMA WideX data

Methyl cyanide ($CH_3CN$), as a symmetric top molecule, allows for sensitive temperature measurements (Loren & Mundy, 1984). It thus serves as a powerful discriminant on whether or not a temperature and excitation model is a good fit to reality. Here we characterize the 257 GHz $CH_3CN$ $14_K - 13_K$ spectrum of L1455 IRS1 as observed by NOEMA. We have the ability to model its spectrum in Local Thermodynamic Equilibrium (LTE), i.e., the situation in which the distribution of molecules among energy states is governed strictly by a Boltzmann distribution. In Section 4.5.3, we fit an LTE model to measure its temperature and column directly, using a source size derived from the ALMA measurements.

Table 4.1. Methyl cyanide lines and fluxes

| Species and line name | Sym-metry | Frequency (GHz) | $E_u/k$ (K) | $A_{ij}$ ($s^{-1}$) | Peak flux (mJy) |
|---|---|---|---|---|---|
| $CH_3CN$ $14_0 - 13_0$ | A | 257.5274 | 92.7 | 1.0e-03 | 113.4 ± 2.2 [a] |
| $CH_3CN$ $14_1 - 13_1$ | E | 257.5224 | 99.8 | 1.0e-03 | 119.7 ± 2.2 [a] |
| $CH_3CN$ $14_2 - 13_2$ | E | 257.5076 | 121.3 | 1.0e-03 | 112.1 ± 1.5 |
| $CH_3CN$ $14_3 - 13_3$ | A | 257.4828 | 157.0 | 9.7e-04 | 126.6 ± 1.4 |
| $CH_3CN$ $14_4 - 13_4$ | E | 257.4481 | 207.0 | 9.3e-04 | 73.0 ± 1.4 |
| $CH_3CN$ $14_5 - 13_5$ | E | 257.4036 | 271.2 | 8.9e-04 | 102.1 ± 3.0 [b] |
| $CH_3CN$ $14_6 - 13_6$ | A | 257.3492 | 349.7 | 8.3e-04 | 55.4 ± 1.5 |
| $CH_3CN$ $14_7 - 13_7$ | E | 257.2849 | 442.5 | 7.6e-04 | 26.1 ± 2.1 [c] |

Note. — Frequencies and $A_{ij}$ values were derived by Müller et al. (2015, 2016), and were accessed via the Cologne Database for Molecular Spectroscopy (CDMS; Müller et al. 2001). Flux fits were derived by using MCMC to fit Gaussians to each line; each line had an independent height, but they shared a jointly constrained line width and velocity center. Uncertainties are taken from the 16th and 84th percentile of the posterior probability distribution for each parameter. Notes: [a] $CH_3CN$ $k = 0$ and $k = 1$ are strongly blended. [b] $CH_3CN$ $k = 5$ is strongly blended with a $CH_3OH$ transition. [c] Only half of the $CH_3CN$ $k = 7$ line lies within our WideX spectrum, as it straddles the edge of the observed window.

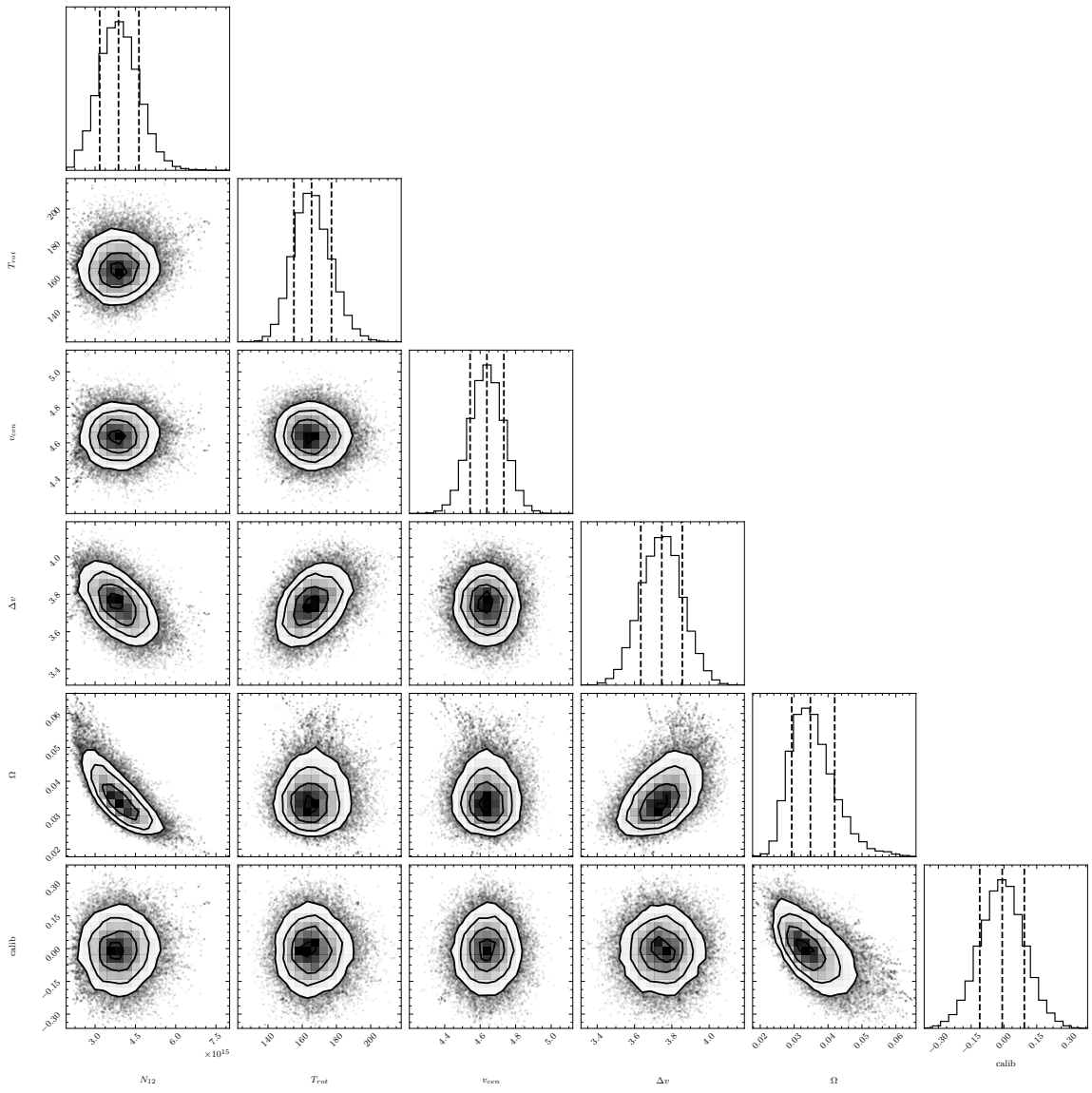


Figure 4.6 Corner plot of MCMC posterior probability distribution from the LTE model fit of the $CH_3CN$ spectrum.

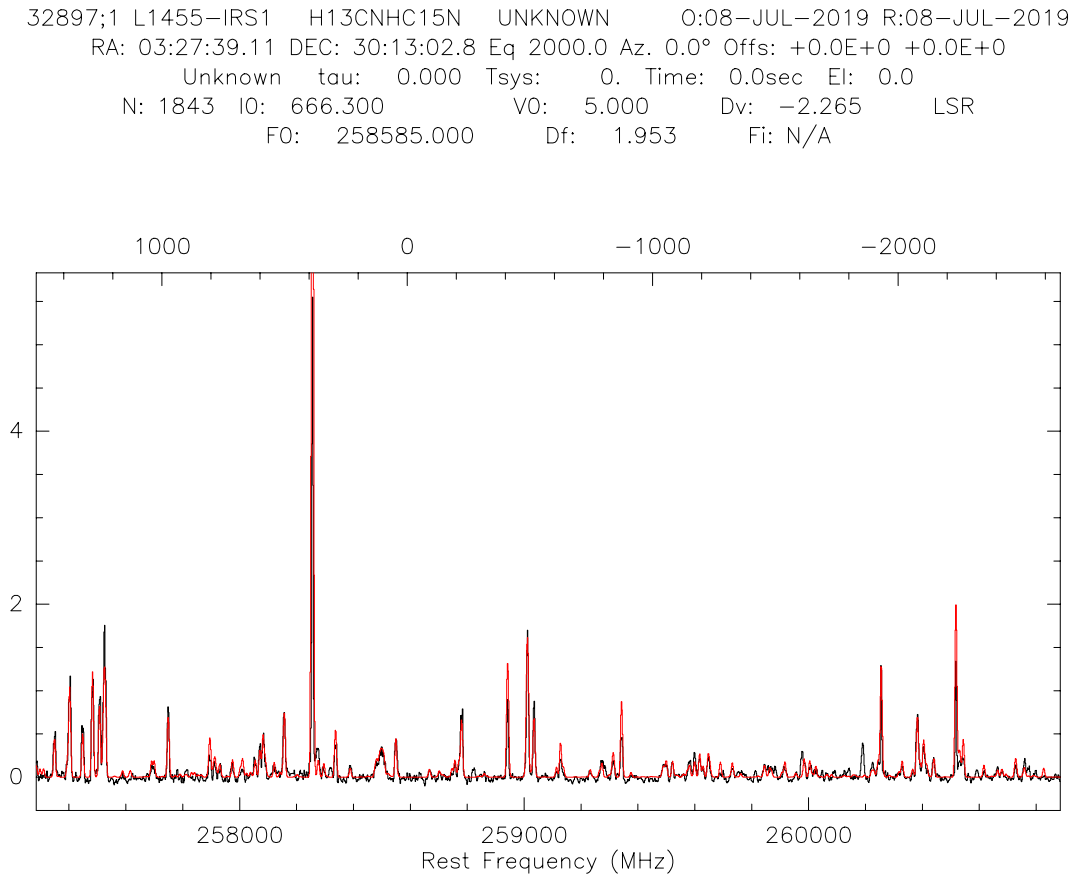


Figure 4.7 The full, 3.6 GHz-wide NOEMA Band 3 WideX spectrum from 257285 to 260884 MHz is shown in black; in red, the `WEEDS` (Maret et al., 2011) model is shown. In this `WEEDS` model, the following species are included: the simple species SO, SiO, $SO_2$, $H^{13}CO^+$, $H^{13}CN$, and $HC^{15}N$; the simple organics $H_2CO$, HDCO and HCOOH; and the complex (i.e, possessing six or more atoms, following Herbst & van Dishoeck 2009) organics $CH_3OH$, $CH_3CN$, $CH_3CHO$, $CH_3OCHO$, $CH_3OCH_3$, and tentatively, $C_2H_5CN$, $CH_2DCN$, and $CH_2DOH$.

Table 4.2. `WEEDS` model parameters

| Species | $N_{\rm tot}$ (cm$^{-2}$) | $T_{\rm ex}$ (K) | Size ($''$) |
|---|---|---|---|
| $H^{13}CN$ | 2e15 | 100 | 0.22 |
| $HC^{15}N$ | 6e14 | 100 | 0.22 |
| SO | 1e16 | 100 | 1.0 |
| SiO | 1e14 | 100 | 1.0 |
| $H^{13}CO^+$ | 3e13 | 100 | 1.0 |
| $SO_2$ | 1e17 | 100 | 0.22 |
| $H_2CO$ | 3e18 | 100 | 0.22 |
| HDCO | 1e16 | 100 | 0.22 |
| HCOOH | 1e16 | 100 | 0.22 |
| $CH_3CN$ | 7e15 | 165 | 0.22 |
| $CH_3OH$ | 5e17 | 165 | 0.22 |
| $CH_3OCHO$ | 1e17 | 165 | 0.22 |
| $CH_3CHO$ | 3e16 | 165 | 0.22 |
| $CH_3OCH_3$ | 1e17 | 165 | 0.22 |
| $C_2H_5CN$? | 3e15 | 165 | 0.22 |
| $CH_2DCN$? | 1e15 | 165 | 0.22 |
| $CH_2DOH$? | 1e17 | 50 | 0.22 |

Note. — WEEDS. All molecules use a single velocity component with $\Delta v_{\rm FWHM} = 8.85$ km s$^{-1}$. Top section: simple species. Second section: simple organics. Third section: confirmed complex organics. Fourth section: tentative complex organics. The corresponding model is shown in Fig. 4.7.

In Figure 4.5, we present the observed NOEMA spectrum which covers eight transitions of $CH_3CN$. The $CH_3CN$ $(J_K)$ $14_K - 13_K$ lines, with each line from $K = 0$ to 7 clearly detected, span upper state energies $E_{\rm u}/k = 92 - 442$ K.

### 4.5.3 LTE model

We now consider LTE excitation, in order to measure the temperature of $CH_3CN$ without being constrained by our pre-existing physical model. In order to assume LTE, the density of the gas typically needs to exceed the so-called "critical density" of the molecule in question. The critical density for the $14_K - 13_K$ ladder is $2 \times 10^6$ cm$^{-3}$ at a temperature of 100 K (extrapolated to higher $J$ from Shirley 2015). This density is exceeded everywhere within a radius of 70 au in our physical model of L1445 IRS1 (i.e., the entire hot core). One subsequent advantage of LTE modeling is its computational efficiency, allowing for many more model evaluations (and thus a wider

parameter search and better constraints on uncertainties; e.g., via MCMC methods). Instead of the usual approach of constructing a population diagram (Goldsmith & Langer, 1999), we here directly model the spectrum, in part because of the high number of line blends and the issues of optical depth.

Below, we describe our approach to modeling the $CH_3CN$ spectrum that takes into account moderate optical depths and line blending. The difference between this LTE case and the previous non-LTE model is that we are exploring constant gas temperature models as opposed to ones that rely on physical gradients, particularly in temperature. Our goal in this simpler model is to understand what temperature is required to reproduce the $CH_3CN$ observations, and then explore what this might mean for the source structure.

Given a column density $N_{\rm tot}$ ($\rm cm^{-2}$) of $CH_3CN$ molecules, which have temperature $T_{\rm rot}$ (K), the population in any energy state is given by

$$\frac{N_u}{g_u} = \frac{N_T}{Q(T_{\rm rot})} e^{-E_u/T_{\rm rot}} \tag{4.1}$$

in which $N_u$ is the column density of molecules in upper-state $u$, $g_u$ is the statistical weight of that state, and $Q$ is the partition function[1], expressed as follows for $CH_3CN$:

$$Q(T_{\rm rot}) = \left(\frac{5.34 \times 10^6}{\sigma}\right)\left(\frac{T_{\rm rot}^3}{B^2 A}\right)^{1/2} \tag{4.2}$$

with $\sigma = 3$, $A = 158099$ MHz, and $B = 9198.9$ MHz, as listed[2] in the Spectral Line Atlas of Interstellar Molecules (SLAIM).

The intensity $S_\nu$, in the optically thin limit, is then given by the following expression:

$$S_\nu = \frac{N_u A_{ul} \Omega h c}{4\pi} \phi(\nu) \tag{4.3}$$

[1]For a full treatment of molecular physics and partition functions, see Gordy & Cook (1984).

[2]`http://www.cv.nrao.edu/php/splat/species_metadata_displayer.php?species_id=606`

where $A_{ul}$ is the Einstein $A$ coefficient (in $s^{-1}$) for the transition in question, $\Omega$ is the solid angle (in steradians) subtended by the source, and $\phi(\nu)$ is the line profile function centered on $\nu = \nu_0$, conventionally normalized such that $\int_0^\infty \phi(\nu) d\nu = 1$.

Typically, one can assume a top-hat function for $\phi$, such that $\phi = 1/\Delta\nu_{\rm FWHM}$. However, we instead choose a Gaussian function for $\phi$, assuming that velocities are dispersed in a Gaussian distribution (e.g., as in a Maxwell-Boltzmann velocity distribution, such as a thermal or turbulent motion). We thus write

$$\phi(\nu) = \frac{1}{\sqrt{2\pi}\sigma_v} e^{-x^2/2\sigma_v^2} \tag{4.4}$$

with $\sigma_v$ the Gaussian $\sigma$ of the velocity spread, $\nu_0$ is the line's rest frequency, and $x = \nu - \nu_0$ represents the difference between the frequency $\nu$ under consideration and the line center $\nu_0$.

When optical depth is important, the equation will be modified as follows (building from Le Gal et al. 2019, Appendix A). The optical depth arising from each molecular state as a function of frequency $\nu$, $\tau_\nu$(line), is given by

$$\tau_\nu(\text{line}) = \phi(\nu) \frac{N_u A_{ul} c^3}{8\pi\nu_0^3} \left(e^{h\nu_0/k_B T_{\rm ex}} - 1\right) \tag{4.5}$$

in which the number of molecules available to absorb light at each frequency is $\phi(\nu) N_u$.

The total optical depth $\tau_\nu$ thus is given by $\tau_\nu = \sum_i^{\rm lines} \tau_\nu(\text{line}_i)$. If multiple species are being modeled, all are included in the sum, which accounts for line blending within and between species. This total $\tau_\nu$ is then used in the full expression for $S_\nu$ for each line in the spectrum:

$$S_\nu(\text{line}) = \phi(\nu) \frac{N_u A_{ul} \Omega h c}{4\pi} \frac{(1 - e^{-\tau_\nu})}{\tau_\nu}. \tag{4.6}$$

Finally, the total spectrum is obtained by summing $S_\nu = \sum_i^{\rm lines} S_\nu(\text{line}_i)$, considering

lines from all species under consideration.

Using the above-derived formalism, we fit an LTE model of $CH_3CN$ lines to the observed NOEMA spectrum. We vary $N_{\rm T}$ and $T_{\rm rot}$, along with the central velocity of the source $v_{\rm cen}$ and the line width $\Delta v$ (expressed here as Gaussian $\sigma$ rather than a FWHM). A flux calibration factor with $\sigma = 10\%$ is introduced to mitigate the effect of calibration error; we marginalize over this "nuisance parameter" in the estimates of the other parameters. We use the Python package `emcee` (Foreman-Mackey et al., 2013a,b), an implementation of the affine-invariant sampler proposed by Goodman & Weare (2010), to perform our model fitting. Our likelihood function,

$$\ln \mathscr{L} = K - \frac{1}{2}\chi^2, \tag{4.7}$$

where $K$ is an arbitrary constant, which is intentionally neglected in the likelihood optimization process (see Hogg & Foreman-Mackey 2018 for further discussion on MCMC methods and likelihood maximization). The likelihood function $\ln \mathscr{L}$ is based on the following $\chi^2$:

$$\chi^2 = \sum_{\nu}^{\rm chan} \frac{\left(I_\nu({\rm data}) - I_\nu({\rm model})\right)^2}{\sigma^2_{\rm data}} \tag{4.8}$$

in which $I_\nu$(data) and $I_\nu$(model) are the intensities in the data and model, respectively, at each channel. We estimate the noise in our spectrum from line-free channels; the rms in the spectrum is approximately 2.5 mJy. We use 24 walkers and run the MCMC sampler for 14,000 steps. Autocorrelation times $\tau$ for each of the four model parameters vary from $\sim$ 130 to 400 steps; we discard the first 5000 as burn-in. Typically, an MCMC chain can be said to be "converged" when it has been run for $\gtrsim 10$ times the autocorrelation time $\tau$ (but, again, see Hogg & Foreman-Mackey 2018 for further discussion).

### 4.5.4 WEEDS spectral modeling

To interpret the remaining features of the WideX spectrum, we used the WEEDS package (Maret et al., 2011), an extension to the CLASS/GILDAS software package (Pety, 2018). Instead of attempting to do a full MCMC fit with all these molecules, we used the temperature of $CH_3CN$ and the spatial size of $CH_3OH$ as prior information to guide the modeling of these additional species. In Table 4.2, we present the molecular parameters used to fit the WideX spectrum; the resulting spectral fit is shown in Figure 4.7.

We identify a large number of organic species that are necessarily present to account for the complex NOEMA spectrum. Among these species are the simple organics $H_2CO$, HDCO, and HCOOH, and the complex organics $CH_3OCHO$, $CH_3CHO$, and $CH_3OCH_3$. We also tentatively identify $C_2H_5CN$, $CH_2DCN$, and $CH_2DOH$.

The presence of these complex organics in this hot ($T \sim 165$ K) gas within a tentative disk indicates a warm, chemically rich environment.

## 4.6 Discussion

The chemically rich and warm gas seen in the central component of L1455-IRS1 B can be compared to two other low-mass Class 0 protostars which are currently being studied in depth, IRAS 16293 and HH 212. IRAS 16293 is a well-known astrochemical template, a binary system with luminosity $21 \pm 5 L_\odot$ which lies at a distance 120 pc and is the target of the PILS ALMA program (Jørgensen et al., 2016). HH 212 is a Class 0 protostar with luminosty 9 $L_\odot$ (Lee et al., 2019) which lies at a distance 400 pc in Orion. For comparison, as measured in Chapter 3, L1455 IRS1 has a luminosity $5.8 L_\odot$ (combined between components A and B), and source B (at 1.2 mm continuum) is about half as bright as source A.

Morphology: IRAS 16293's binary components are separated by 5", and are con-

nected by a dusty filamentary structure seen in continuum wavelengths. HH 212 drives a powerful, rotating bipolar jet.

The chemical complexity of organics seen towards L1455-IRS1B is comparable to that seen in IRAS 16293 and HH 212. Some molecules in IRAS 16293 (notably, ethylene glycol and glycoaldehyde) have an excitation temperature of 300 K, while the organic-rich gas HH 212 is better fit by an excitation temperature 150 ± 50 K (Lee et al., 2019). In this context, the gas temperature measured for L1455-IRS1 is consistent with these objects, and not similar to temperatures seen in more mature protoplanetary disks also measured with $CH_3CN$ lines, such as TW Hya's 32± 3 K (Loomis et al., 2018), MWC 480's 73±28 K, and V4046 Sgr's 29±2 K (Bergner et al., 2018).

### 4.6.1 Structure of the L1455 IRS1 system

Our study of L1455 IRS1 can be put into context with other recent high-resolution studies of this protostar. Notably, Chou et al. (2016) and Tobin et al. (2018) each published high-resolution continuum and line maps of this source. Chou et al. (2016) used IRAM 30m and $4\farcs5 \times 2\farcs7$ SMA maps of $C^{18}O$ and $^{12}CO$ to inspect L1455 IRS1's connection to the larger molecular cloud, noting that it appears to be connected to an infalling filament via which it may actively be accreting gas from the surrounding cloud. In the context of the current observations, they separate the kinematic signatures of the large-scale outflows (principally traced by $^{12}CO$) from a smaller-scale rotation (seen at $C^{18}O$). They claim evidence for a disk of size $< 200$ au, with the same small-scale velocity gradient orientation observed here at $H^{13}CN$.

Tobin et al. (2018), in more recent ALMA observations at 1.3 mm with resolution $0\farcs27 \times 0\farcs16$ (continuum) and $0\farcs35 \times 0\farcs25$ (line), confirmed the outflow orientation arising from L1455 IRS1 (which they denote Per-emb-17), resolved the continuum binary and traced velocity gradients arising both from the small-scale rotation and

the larger outflow using $^{13}$CO, C$^{18}$O, and SO. Their observations of $H_2CO$, especially, confirm the exact rotation morphology seen here at H$^{13}$CN and $CH_3OH$.

### 4.6.2 Protostellar disks

In the current era of high-resolution ALMA observations, resolved line and continuum observations toward low-mass protostellar "hot corinos" are increasingly common. One trend that is becoming increasingly clear is that many of these so-called "hot corinos" are being revealed as molecule-rich, warm protostellar disks, rather than $\sim$ spherically symmetric warm spheres of molecule-rich gas. As a most recent example, HH 212, believed to be a traditional hot corino (Codella et al., 2016), has been shown to have a disk with a warm disk atmosphere that is molecule-bright (Lee et al., 2019) and contains a number of organic molecules. Observations of the young disk at protostar L1527 (van 't Hoff et al., 2018) reveal that it has a warmer temperature than most Class II disks, confirming model predictions regarding the thermal structure of protostellar disks. This disk has recently been observed to display a prominent warp (Sakai et al., 2019), indicating possibly either ongoing accretion of gas in an anisotropic way or a strong magnetic field distorting the disk.

From a more statistical point of view, Segura-Cox et al. (2018) used continuum observations of the VANDAM survey to identify Class 0 disk candidates. In their study, 78% of Class 0 and I protostars did not show signs of disks larger than their 12 au lower limit. Hence, it remains the case that most Class 0 sources do not have resolved disks; it is perhaps only those Class 0 systems which have started to form disks that are observable at bright molecular lines. In the context of this chapter, we are thus likely observing $CH_3CN$ from the warm atmosphere of a protostellar disk that is actively growing via accretion. This accretion provides the needed energy to get very hot gas on the observed spatial scales.

## 4.7 Conclusions

In Conclusion, in this chapter we showed:

1. The low-mass Class 0 protostellar binary L1455-IRS1 lies in a physically and kinematically complex environment. Using resolved ALMA observations, we attempted to disentangle the big outflow from the circumbinary envelope from the disk from a small one-sided outflow. We presented evidence for a tentative Keplerian disk.

2. The NOEMA spectrum shows a rich forest of lines. Eight $CH_3CN$ lines appear in this spectrum, facilitating a sensitive measurement of temperature. We measured the gas temperature in the tentative disk to be $165 \pm 10$ K. Based on this gas temperature measurement, we estimate column densities of a number of other species, including some complex organics such as $CH_3OH$, $CH_3OCHO$, $CH_3CHO$, and $CH_3OCH_3$, as well as possibly $C_2H_5CN$, $CH_2DCN$, and $CH_2DOH$.

# CHAPTER V

# Conclusions and Future Outlook

## 5.1 Summary of conclusions

In this dissertation, I have presented an investigation of nitrogen carriers in protostellar environments with a goal of identifying those nitrogen carriers that would provide the nitrogen ultimately delivered to terrestrial worlds like the Earth. Below is a summary of the findings of each chapter.

Chapter II, "Exploring the Origins of Earth's Nitrogen: Astronomical Observations of Nitrogen-bearing Organics in Protostellar Environments":

1. HCN is by far the most abundant nitrogen-bearing organic in the Orion KL Hot Core.

2. The HCN abundance in the hot inner envelope of IRAS 16293−2422 is $X_{\rm in}$= $5.9 \pm 0.7 \times 10^{-8}$.

3. We make an astronomically-motivated prediction that the HCN binding energy $E_{\rm B}/k = 3840 \pm 140$ K.

4. The N/$H_2O$ ratio in molecular ices seen in the inner protostellar envelopes is not high enough to account for the total N/$H_2O$ seen in comets. We suggest

that the nitrogen contained in interstellar dust is the likely precursor to most of the N in comets.

5. The high $^{15}$N enrichment seen in cometary and meteoritic bodies is likely donated by molecular ices that underwent chemical fractionation of nitrogen isotopes.

Chapter III, "Hunting for Hot Cores: Small-scale HCN Measurements Towards Five Low-mass Protostars":

1. In our sample of five protostars, only L1455 IRS1 had strong detectable H$^{13}$CN $3-2$ emission at small scales.

2. The hot core abundance of L1455 IRS1 is $4.0 \times 10^{-8}$, a value within 50% of IRAS 16293.

3. We have inferred upper limits on the HCN abundances on small scales of the other four protostars.

4. We confirm that small-scale hot corino emission from low-mass protostars depends strongly on their luminosity.

Chapter IV, "High-resolution HCN and $CH_3CN$ Observations from ALMA and NOEMA of L1455 IRS1, a Chemically Rich Low-mass Protostellar Hot Core with Signs of a Warm Disk":

1. We have resolved the H$^{13}$CN-bright hot core of L1455 IRS1 to be 53 au in size. It is smaller and brighter than our model predicted.

2. L1455 IRS1 is a binary with separation 60 au. Essentially all of the H$^{13}$CN emission is centered on the fainter companion (source B).

3. The velocity gradient in the $H^{13}CN$ $3-2$ emission indicates a Keplerian disk of size $r \approx 25$ au and rotation speed $v_{\rm Kep} = \pm 3$ km s$-1$, implying a central mass of 0.25 $M_{\odot}$.

4. Detections of $CH_3CN$ and $CH_3{}^{13}CN$ allow models to infer a hot-core $CH_3CN$ abundance of $X = 2.3 \times 10^{-8}$ and a gas temperature of $T_{\rm rot} = 319 \pm 5$ K.

5. The $CH_3CN$/HCN ratio in this source appears super-cometary, hinting at a rich chemistry of nitrogen-bearing organics.

## 5.2 Future Outlook

### 5.2.1 Broader survey of HCN in protostellar hot cores

In Chapter III, I showed that the detectability of an HCN-bright region in a hot corino is a strong function of the bolometric luminosity of the protostar in question – explaining the non-detections of small-scale $H^{13}CN$ towards four of the five surveyed protostars. The downside to this "null" result is that the variation among HCN abundances in hot corinos remains unexplored. I therefore suggest a program which, building on the techniques and results from Chapter III, would be able to more meaningfully explore these abundances such that even a similar string of non-detections would be highly meaningful. For this survey to be scientifically valuable, we will want to ensure a higher yield of line detections and more informative upper limits on abundances. For a future survey of organic nitrogen carriers in low-mass protostars at small scales, we will take the following items into consideration.

**Targets**– The results from this pilot study do not conclusively identify whether evolutionary stage, or luminosity, determines the detectability of a hot core. In a follow-up survey, we would include a minimum of 15 sources which would span a grid of values in both luminosity and evolutionary class. Suitable targets may include the 16 protostars already observed with the IRAM 30m telescope in Graninger et al.

(2016); Bergner et al. (2017), for which some large-scale chemical abundances have already been determined.

**Observing time**– The sensitivity required for scientifically valuable results may be calculated ahead of time by computing chemical models to predict the strength of hot core emission (similarly to what we did here in Section 3.7). The broad availability of luminosity estimates from catalogs of protostars in Perseus (as compiled, e.g., by Tobin et al. 2016b), will facilitate selection of targets whose presumed hot cores would be detectable in a known amount of integration time. Requesting observations that reach triple this sensitivity for each source will ensure that interesting upper limits are reached even for non-detections.

**Wavelength coverage**– Given the relatively recently expanded wavelength and sensitivity capabilities of NOEMA and the SMA, as well as the preëminence of ALMA, a followup survey which goes substantially deeper while targeting transitions of many more nitrogen-bearing organics (especially $CH_3CN$, HNC, HNCO, $CH_3NH_2$, and possibly others) would yield valuable results without necessarily increasing the required observing time by a notable factor. It will be fruitful to compare the abundance ratios among various nitrogen-bearing species (such as $CH_3CN$/HCN) to those measured in IRAS 16293 by the PILS survey (Jørgensen et al., 2016), as well as to protoplanetary disks (e.g., Öberg et al. 2015; Bergner et al. 2018, 2019) and comets (Mumma & Charnley, 2011). Another desirable adjustment: the $H^{13}CN$ $4-3$ line (345.340 GHz), which probes slightly warmer gas ($E_u/k = 41.4$ K) than the $3-2$ line ($E_u/k = 24.9$ K), would help determine the temperature of any small-scale emission. This line would likely be a more valuable use of observational resources than attempting to image the $H^{13}CN$ $1-0$ line as was done here, despite the more difficult observing conditions at 345 GHz from most millimeter/submillimeter sites.

**Choice of observatory**– NOEMA is a natural choice for this follow-up program. Since the time of the NOEMA observations presented in Chapter III, NOEMA has

expanded from 8 to 10 antennas, increasing its sensitivity and angular resolution. Additionally, the new PolyFIX correlator is operational, facilitating simultaneous observations of a 32 GHz window – meaning that these HCN observations should readily be able to simultaneously include transitions of many other nitrogen-bearing species as well as other interesting chemical and physical tracers. Nonetheless, the SMA would also have most of the capabilities necessary to do this observational work as well. Finally, ALMA may be a reasonable choice as well — its much-higher sensitivity and angular resolution would make the completion of this survey much faster, though ALMA cannot currently match the bandwidth offered by PolyFIX. The next expected NOEMA call for proposals would be September 2019.

### 5.2.2 Higher-resolution observations of $CH_3CN$ in a hot protostellar disk

In Chapter IV, I used resolved (0.″2) ALMA observations of $H^{13}CN$ to show that the HCN-bright "hot corino" at L1455 IRS1 appears to be consistent with a rotating disk. Using $CH_3CN$ emission in an un-resolved (1.″4) NOEMA beam, I constrained the overall temperature of the gas in this disk. However, various issues, including (a) the unknown true size of the $CH_3CN$ emitting region, (b) the optical depth of the $CH_3CN$ lines, (c) the likely presence of a temperature gradient which is "averaged-over" in the NOEMA observations, make a follow-up observation at higher resolution and sensitivity desirable. Ideally, this follow-up would have spatial and spectral resolution sufficient to resolve the disk in 5–10 beam elements (rather than the marginally resolved observations presented in Chapter IV) and the ability to detect the kinematic signature of rotation, as well as the sensitivity needed to measure confidently the $CH_3{}^{13}CN$ lines, thus using the $^{12}C/^{13}C$ ratio to constrain the optical depths of various lines.

In this suggested program, suitable for proposal in ALMA Cycle 8 (expected Call for Proposals: April 2020), I suggest observations of L1455 IRS1 targeting the $CH_3CN$

and $CH_3{}^{13}CN$ $J_K = 14_K - 13_K$ ladders at 257 GHz (the same transitions seen in the NOEMA observations presented in Chapter IV), with the following properties:

- Resolution: $0\farcs02 - 0\farcs04$ (5–10 au)
- Sensitivity: $\sim 1$ mJy beam$^{-1}$
- Spectral resolution: $\sim 0.2$ km s$^{-1}$

For comparison, the $0\farcs036 \times 0\farcs03$ observations at 1.69 km s$^{-1}$ spectral resolution of Lee et al. (2019) reached a similar sensitivity in 98 minutes of on-source time; a simple scaling of sensitivity needs to integration time suggests this program could be completed in about 3 times as much time, or $\sim$ 5 hours of on-source ALMA time – a modest proposal below the median requested time across ALMA proposals in Cycle 7[1].

### 5.2.3 JWST direct observations of nitrogen carriers

The James Webb Space Telescope (JWST) will facilitate direct measurements of a large number of gas-phase molecules (in emission, typically) and ice-phase molecules (in absorption, typically) which will be of key interest to the study of the origins of biogenic materials in terrestrial worlds. An example of such a JWST program which is already scheduled to be carried out upon the successful launch of JWST is called IceAge (P.I: McClure; McClure et al. 2017), which is designed to target many molecular species. Among the molecules (especially in the gas phase) that JWST will be expected to observe are $NH_3$ and HCN, and potentially their D, $^{13}C$, and $^{15}N$ isotopologues.

A deeper understanding of the distributions of these major N-bearing ices $NH_3$ and HCN in a number of planet-forming zones in protostellar and protoplanetary environments will directly inform part of our knowledge of how much nitrogen might be

[1]The ALMA Cycle 7 proposal statistics are compiled at `https://www.almaobservatory.org/en/announcement/high-demand-for-alma-time/`.

received by planetesimals (could be available to planetesimals) in these planet-forming regions. It is not immediately clear if these species would be directly incorporated into solid bodies; certainly, their higher sublimation temperatures relative to NI and N2 would help this factor, but (as of yet) the progenitor of N in these rocks is still unknown and our best measurements available (cf. Pontoppidan et al. 2019). A combined approach which includes JWST gas- and ice-phase measurements (expanding on work done using other facilities by Pontoppidan et al. 2019, Öberg et al. 2008), combined with sensitive ALMA observations as well as detailed chemical models (cf. Cleeves et al. 2018), should be able to advance our view of gas and ice-phase nitrogen carriers in the terrestrial planet forming zone of young disks, and help us understand how much, if any, of these species provide the nitrogen received by rocky planetesimals.

### 5.2.4 On further constraints of refractory nitrogen carriers in the interstellar medium

Most of the analysis in this dissertation has focused on gas- and ice-phase molecular carriers of nitrogen. However, as the conclusions of Chapter II indicated, the bulk of the nitrogen inherited by comets (and likely chondrites) seems to not have been in gas or ice molecular form at the dawn of the Solar System's formation. A consequence of this is that further constraints on the nitrogen in more refractory forms are needed. Refractory carriers of nitrogen may include:

- minerals bound up in dust, especially silicates (e.g., $Si_3N_4$ and complexes of SiC, with pre-solar silicate grains discussed by Clayton & Nittler 2004),
- carbonaceous dust with nitrogen inclusions (e.g., PAHs with nitrogen dopants, as discussed by Chiar et al. 2013 and Jones 2016),
- salts such as ionic compounds of cyanate ($OCN^-$) or ammonium ($NH_4^+$); (Rau-

nier et al. 2004; Boogert et al. 2008), and

- polymers (such as long cyanopolyyne chains, i.e., $HC_nN$, or other carbon chains, e.g., as discussed by Matthews & Minard 2006).

In some cases, remote sensing can allow for detection and study of some of these refractory carriers – for example, via infrared absorption from ices and minerals (e.g., as seen by *Spitzer*, Boogert et al. 2008, who analyze the "XCN" or "$OCN^-$" infrared feature at 4.62 $\mu$m). For these classes of materials, the advent of JWST will facilitate much more sensitive observations; when coupled with laboratory reproductions of ice-dust mixtures that match realistic astrophysical conditions, the abundances of some refractory nitrogen carriers may be measurable. However, not all of these refractory nitrogen carriers are readily observable in interstellar space using remote sensing. Hence, analyses of rocks from our own Solar System are often critical to understanding our origins. Further work in identifying pre-solar materials in sample analyses of meteorites and interplanetary dust particles (IDPs) may yield important insights. And, naturally, the yet-to-be released full accounting of nitrogen-bearing material in the Rosetta analysis of Comet 67P will also provide critical information on this subject.

The analysis presented in Chapter II on the upper limits of nitrogen which could be sequestered in interstellar dust made use of the results from Jensen et al. (2007), who analyzed FUSE and HST observations of neutral atomic nitrogen gas (N I) in the diffuse interstellar medium. While their results were robust, the very small observed depletion of N I may benefit from additional observations to further and more precisely constrain the maximum possible nitrogen budget in interstellar dust. Finally, direct measurements of gas-phase $N_2$ — while extremely difficult — may be a critical path forward in further clarifying the disposition of nitrogen in interstellar space. Knauth et al. (2004) detected $N_2$ via three blended far-ultraviolet transitions at 95.9 and 96.0 nm using the Far Ultraviolet Spectroscopic Explorer (FUSE), a space obser-

vatory specifically designed to operate in the far-ultraviolet regime. $N_2$ has not been confidently detected in any other astrophysical environment since then, but an initial assessment of the spectral resolution and sensitivity of the Cosmic Origins Spectrograph on the *Hubble Space Telescope*, which covers 90—320 nm, indicates that it should be able to repeat the detection of $N_2$ and perhaps make further detections of this elusive yet extremely abundant species. Given how elusive nitrogen's origins are, such observations may prove valuable in this broader context.

### 5.2.5 Perspectives on Habitability

In Chapter I, I comment on the Drake equation parameter $N_e$, the number of potentially habitable worlds per planetary system. I highlight how one way of addressing this topic is to investigate the origins of volatiles on terrestrial worlds: if all terrestrial worlds receive the same volatile content, then $N_e$ may be high; but if terrestrial worlds receive different volatiles, reflecting diverse and particular processes which vary from system to system, then $N_e$ has the potential to be quite low. In this dissertation I have addressed the origins of the Earth's nitrogen through the study of gas phase carriers of nitrogen in protostellar systems. My conclusions include support for a refractory origin of nitrogen on terrestrial worlds. Because these refractory materials were likely to have formed before the birth of the solar system (e.g., in supernova ejecta, or in the outflowing carbonaceous material produced in the atmospheres of old, giant stars), a refractory origin of nitrogen more closely supports the common inheritance scenario for the origins of terrestrial nitrogen. Hence, when it comes specifically to nitrogen at least, this can be interpreted as evidence that terrestrial worlds throughout our Galaxy have the potential to receive similar nitrogen content, all things being equal, and hence the number of potentially habitable worlds ($N_e$) may be high — at the very least, in this interpretation, the provenance of nitrogen would not be a bottleneck.

A variety of further factors will have to be addressed before such a conclusion

can be considered definitive. For example, the processes within a given solar system's terrestrial planet forming zone may separate relatively nitrogen-rich rocks from relatively nitrogen-poor rocks (e.g., it may be the case that the refractory nitrogen carriers in dust may still sublimate at intermediate to high temperatures experienced by solid particles closest to the young star, whereas dust and solids further from the star would stay cool and retain more nitrogen). Thus, even if all solar systems receive nitrogen in the same way that our Solar System did, the specific processes by which rocks are assembled in these systems could play a major role in whether there are many or few rocky worlds with notable amounts of nitrogen. (As an example, one can consider a system identical to ours, except that there were no major "Grand Tack"-style migrations of giant worlds. In this scenario, all terrestrial habitable zone worlds may end up forming entirely from rocks that began close to the star, and would end up as nitrogen-poor bodies quite different from the Earth in nitrogen content despite having many similarities to the Earth in other respect.) It is unknown how little nitrogen could be on a planet and it still to be considered habitable, but one can imagine planets so nitrogen-poor that the chemistry we understand as necessary for life is far more inefficient to the point that chemical and biological development evolves much more slowly or not at all, due to nitrogen starvation.

## 5.3 Final Remarks

As the study of structure, chemistry, and evolution of embedded protostellar disks catches up to the rapidly maturing study of protoplanetary disks (cf. Bergin & Cleeves 2018), detailed chemical models of protostellar disks, and observations which accompany them, should become common. The interpretation of these data will lead to better inferences about the chemical conditions present at the dawn of the planet-forming process. This new knowledge, combined with continued analysis of Solar System information such as the Rosetta mission (Altwegg et al., 2019), will permit

greater insights about the ultimate origins of the material that makes life on Earth possible – helping us understand better not only how life arose on our planet, but whether it is common on the terrestrial worlds throughout our Galaxy.

# APPENDICES

# APPENDIX A

# *Herschel* Line Fitting Results for IRAS 16293

In this Appendix, we show the detailed results of fitting the HCN, $H^{13}CN$, and $HC^{15}N$ lines of IRAS 16293 from the *Herschel* data, as well as the derived properties (such as the optical depth $\tau$) of each state that are measured from comparisons of the isotopologues. The lines and their Gaussian fits are shown in Figure A.1. The fit parameters for the *Herschel* lines, as well as for the ground-based lines from Caux et al. (2011) and Wampfler et al. (2014), are presented in A.1, and the properties derived from these fits are shown in A.2.

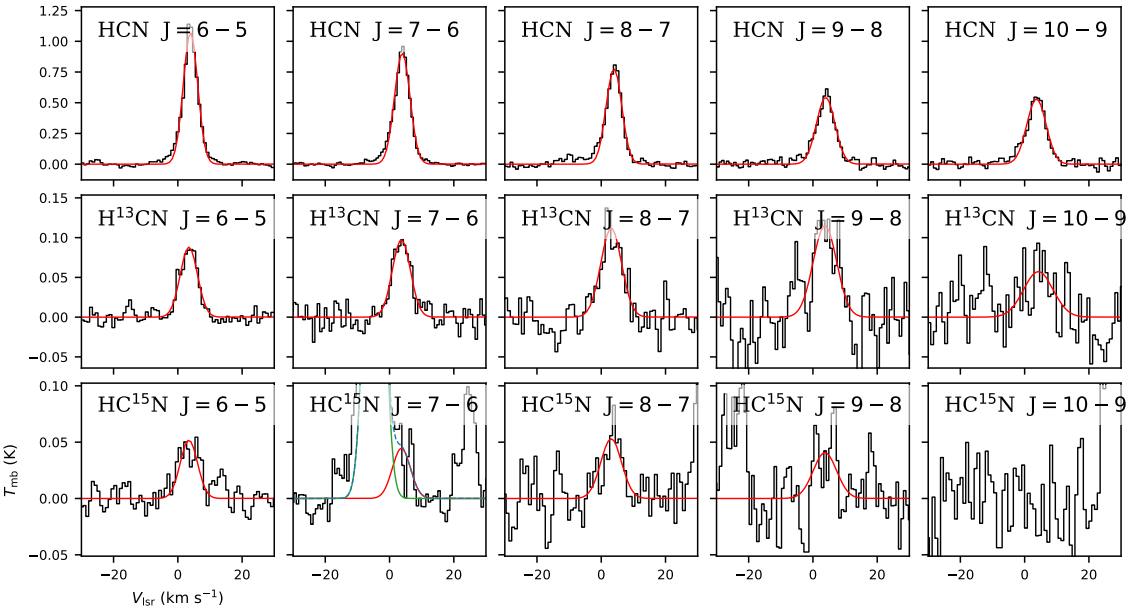


Figure A.1 Gaussian fits to the HCN and isotopologue lines in the HIFI data of IRAS 16293. Smoothed to 3× the resolution of the lowest HCN line. We fit the $HC^{15}N$ $J = 7 - 6$ line simultaneously with the blended SO $J = 14 - 13$ line at 602.292 GHz. We consider $HC^{15}N$ $J = 10 - 9$ to be undetected.

Table A.1. Observed lines of HCN and isotopologues towards IRAS 16293

| Species & Transition | Frequency | Telescope | $\theta_{mb}$ | $V_0$ | FWHM | peak flux | $\int T_{mb} dv$ |
|---|---|---|---|---|---|---|---|
| HCN J= 1 − 0 | 88.6316 | IRAM-30m | 28.4 | 4.46 ± 0.33 | 9.50 ± 0.79 | 1.765 | 21.71 ± 2.39 |
| HCN J= 3 − 2 | 265.8864 | APEX-1 | 24.3 | 3.72 ± 0.01 | 6.81 ± 0.02 | 9.66 | 27.52 ± 2.3 |
| HCN J= 6 − 5 | 531.7164 | HIFI 1a | 40.5 | 3.94 ± 0.02 | 5.30 ± 0.07 | 1.072 | 6.04 ± 0.06 |
| HCN J= 7 − 6 | 620.3041 | HIFI 1b | 34.7 | 3.96 ± 0.02 | 5.70 ± 0.05 | 0.903 | 5.48 ± 0.04 |
| HCN J= 8 − 7 | 708.8772 | HIFI 2a | 30.4 | 3.98 ± 0.06 | 5.74 ± 0.15 | 0.776 | 4.74 ± 0.10 |
| HCN J= 9 − 8 | 797.4337 | HIFI 2b | 27.0 | 3.97 ± 0.09 | 6.80 ± 0.22 | 0.543 | 3.93 ± 0.11 |
| HCN J= 10 − 9 | 885.9714 | HIFI 3b | 24.3 | 3.69 ± 0.09 | 7.06 ± 0.24 | 0.531 | 3.99 ± 0.11 |
| $H^{13}CN$ J= 1 − 0 | 86.3402 | IRAM-30m | 29.1 | 3.88 ± 0.09 | 2.91 ± 0.25 | 0.284 | 1.04 ± 0.12 |
| $H^{13}CN$ J= 3 − 2 | 259.0118 | APEX-1 | 24.3 | 3.75 ± 0.03 | 5.70 ± 0.08 | 0.68 | 3.24 ± 0.3 |
| $H^{13}CN$ J= 4 − 3 | 345.3397 | APEX-2 | 18.2 | 4.28 ± 0.04 | 6.11 ± 0.09 | 1.08 | 5.56 ± 0.8 |
| $H^{13}CN$ J= 6 − 5 | 517.9698 | HIFI 1a | 41.6 | 3.44 ± 0.14 | 6.35 ± 0.30 | 0.088 | 0.60 ± 0.03 |
| $H^{13}CN$ J= 7 − 6 | 604.2679 | HIFI 1b | 35.7 | 3.69 ± 0.20 | 6.62 ± 0.49 | 0.097 | 0.69 ± 0.04 |
| $H^{13}CN$ J= 8 − 7 | 690.5521 | HIFI 2a | 31.2 | 3.10 ± 0.29 | 7.63 ± 0.69 | 0.112 | 0.91 ± 0.07 |
| $H^{13}CN$ J= 9 − 8 | 776.8203 | HIFI 2b | 27.7 | 3.73 ± 0.61 | 8.60 ± 1.48 | 0.115 | 1.05 ± 0.15 |
| $H^{13}CN$ J= 10 − 9 | 863.0706 | HIFI 3b | 25.0 | 4.27 ± 1.41 | 10.80 ± 3.91 | 0.057 | 0.66 ± 0.18 |
| $HC^{15}N$ J= 1 − 0 | 86.0550 | IRAM-30m | 29.2 | 4.03 ± 0.18 | 3.51 ± 0.43 | 0.114 | 0.51 ± 0.06 |
| $HC^{15}N$ J= 3 − 2 | 258.1570 | APEX-1 | 24.3 | 3.71 ± 0.09 | 6.2 ± 0.2 | 0.27 | 1.37 ± 0.1 |
| $HC^{15}N$ J= 4 − 3 | 344.2001 | APEX-2 | 18.2 | 3.11 ± 0.09 | 6.4 ± 0.2 | 0.44 | 2.02 ± 0.3 |
| $HC^{15}N$ J= 6 − 5 | 516.2615 | HIFI 1a | 41.8 | 3.44 ± 0.14 | 6.35 ± 0.30 | 0.052 | 0.35 ± 0.04 |
| $HC^{15}N$ J= 7 − 6 | 602.2754 | HIFI 1b | 35.8 | 3.69 ± 0.20 | 6.62 ± 0.49 | 0.044 | 0.31 ± 0.08 |
| $HC^{15}N$ J= 8 − 7 | 688.2758 | HIFI 2a | 31.3 | 3.10 ± 0.29 | 7.63 ± 0.69 | 0.053 | 0.43 ± 0.25 |
| $HC^{15}N$ J= 9 − 8 | 774.2605 | HIFI 2b | 27.8 | 3.73 ± 0.61 | 8.60 ± 1.48 | 0.041 | 0.37 ± 0.11 |

Table A.2. Derived properties of each energy state of HCN towards IRAS 16293

| $J_u$ | $\tau_{\mathrm{H^{13}CN}}$ | $\tau_{\mathrm{HCN}}$ | $\tau_{\mathrm{HC^{15}N}}$ | $\mathrm{H^{13}CN\,/\,HC^{15}N}$ | $^{14}\mathrm{N}\,/\,^{15}\mathrm{N}$ |
|---|---|---|---|---|---|
| 6 | 0.09 | 5.92 | 0.05 | 1.7 | 119 |
| 7 | 0.11 | 7.87 | 0.05 | 2.3 | 155 |
| 8 | 0.16 | 10.73 | 0.07 | 2.2 | 151 |
| 9 | 0.24 | 16.41 | 0.08 | 3.0 | 210 |
| 10 | 0.11 | 7.87 | — | — | — |

Note. — Derived properties for HCN and $^{14}\mathrm{N}\,/\,^{15}\mathrm{N}$ assume a $^{12}\mathrm{C}\,/\,^{13}\mathrm{C}$ ratio of $69 \pm 6$ following Wilson (1999).

# APPENDIX B

## Corner plots for four protostars

Here are the remaining corner plots referenced by Figure 3.6.

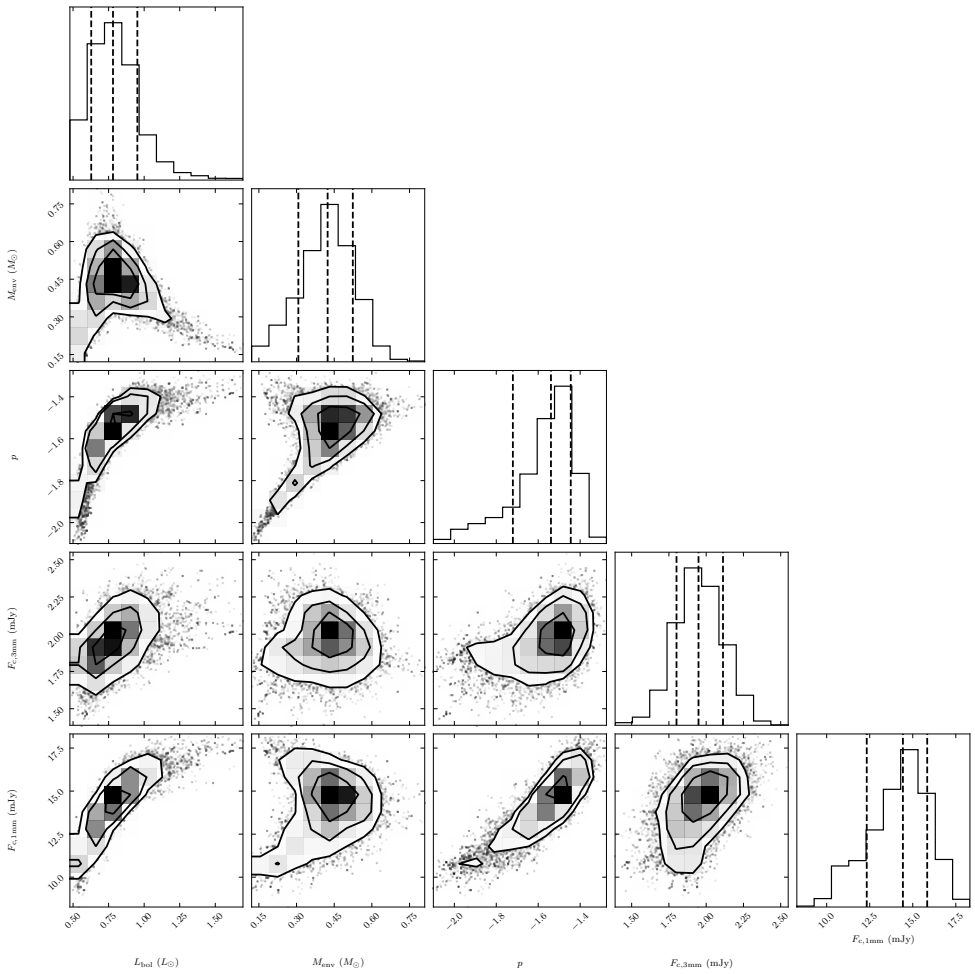


Figure B.1 Corner plot for B1-a's physical model parameters.

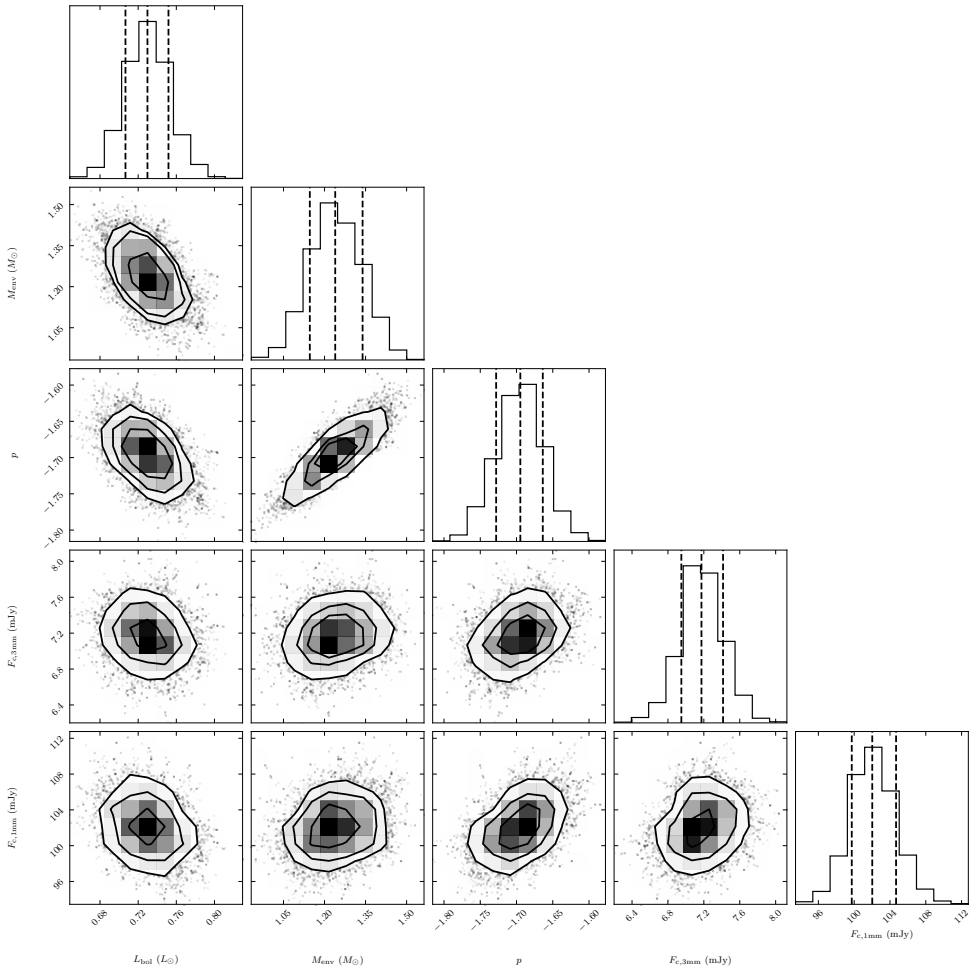


Figure B.2 Corner plot for IRAS 03235's physical model parameters.

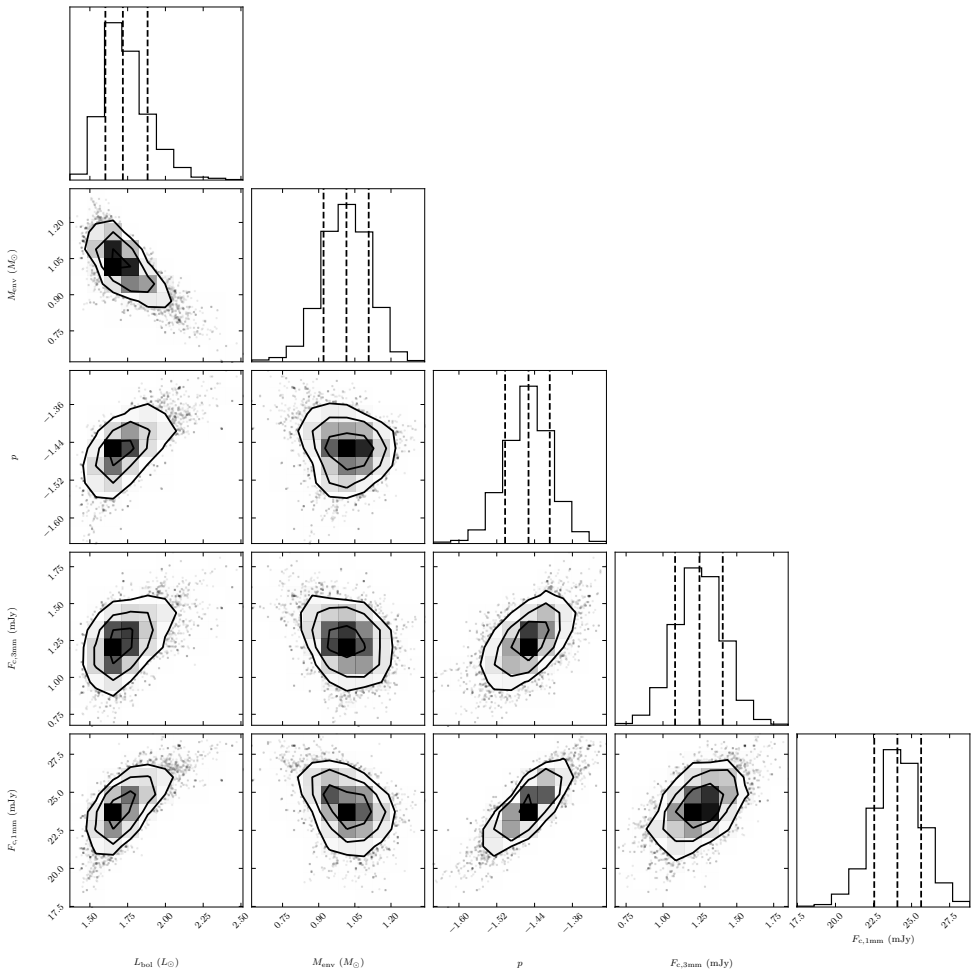


Figure B.3 Corner plot for B5 IRS1's physical model parameters.

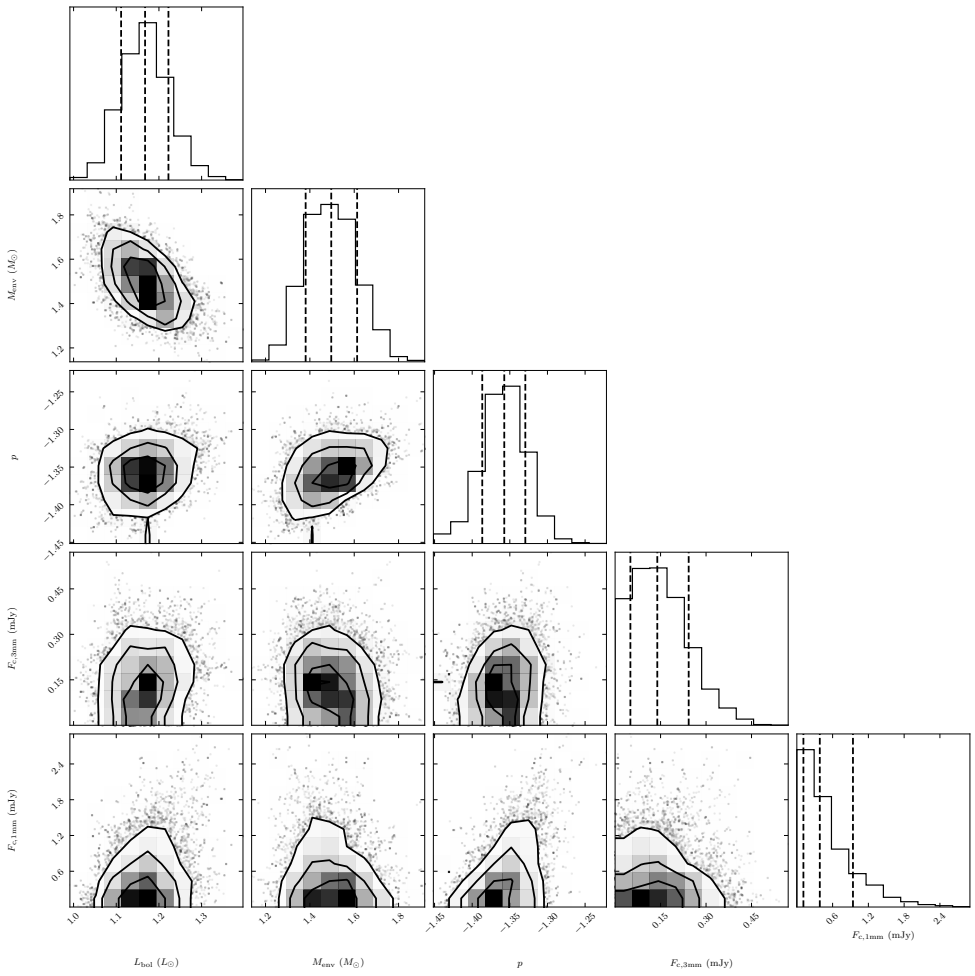


Figure B.4 Corner plot for L1455 IRS4's physical model parameters.

# APPENDIX C

# A comparison of local sources of the CHON carrier $C_8H_{10}N_4O_2$

The CHON carrier $C_8H_{10}N_4O_2$ (note[1]) has not yet been detected in interstellar space (McGuire, 2018), though its presence has been noted in low Earth orbit[2]. This organic molecule is readily obtainable on Earth, and takes part in a variety of non-essential[3] biological processes. $C_8H_{10}N_4O_2$ played a key role in the research carried out in this dissertation; as such, an accounting of its local sources is presented here.[4]

I came to Ann Arbor in 2013 having only lightly dabbled in coffee drinking. As a college senior at Harvard, I couldn't stand dining-hall coffee, and only hesitatingly learned to enjoy the local Starbucks' caramel frappucinos and white chocolate mochas. The situation did not improve much in the subsequent year I spent in Portland, Hawai'i, and San Francisco; I mostly stuck to tea. But in the course of my first and second years of graduate school, I came to respect and then even revere coffee in this town. Ann Arbor is the city where I learned to love coffee, and the coffee-shop culture in this town is special: Ann Arbor cafés punch far above their weight,

[1] Commonly known as "Caffeine."

[2] "How Kjell Lindgren Brews a Cup of Coffee in Space": `https://www.youtube.com/watch?v=L___xygPC94`

[3] Arguably.

[4] Yes! This is a personal review of coffee shops in Ann Arbor.

and in few other places in this country can you find such a geographically dense concentration of excellent coffee shops. In addition to coming to love coffee itself, I have had the pleasure of getting to know many of the devoted baristas in this town, and I've learned a thing or two about artisinal coffee drinks and the coffee industry.

## C.1 A ranked list of the best coffee in Ann Arbor

1. **Vertex Coffee Roasters**. They just opened up at the corner of South University and Washtenaw. The owner and operator, Kara, is incredibly kind and focused on her coffee, and it shows. The space and atmosphere is fantastic; the coffee really comes alive, and it is a delight to try all of their myriad drinks. They often have multiple espresso options available for your espresso-based drinks, a luxury I have only otherwise experienced at **Coffee Collective** in Copenhagen[5]. I regret that they opened only in my final month of living in Ann Arbor; I likely would have written most of my dissertation here if I'd had the chance.

2. **Comet Coffee**. The best pour-over coffees I've had in Ann Arbor. I'm fond of their espresso drinks, even though their straight espresso can taste quite sour. My favorite drink here is their mocha — not sweet, but made with a strong dark chocolate. Perfect for grim, rainy days in the late Fall.

3. **Roos Roast**. I mainly frequent the Liberty St location. I mostly come for the atmosphere; the baristas are lovely. The coffee is good; their roasts are darker than I usually prefer, so instead of my standard cortado I'll usually order a traditional cappucino — the darker roast is well-served by an additional couple ounces of steamed milk.

4. **Literati Coffee**. Consistent and tasty coffee, and a lovely café atmosphere.

[5] An aside: I think Coffee Collective is the best coffee in the world.

The café space can become extremely crowded and noisy, which is the main strike against this space.

5. **Black Diesel**. Fantastic coffee. The only thing that keeps this from spot number three or four is its location relative to me — it's far enough away from downtown Ann Arbor that I've only been here three or four times.

## C.2 Notable mentions.

**Mighty Good Coffee** – For most of my six years in Ann Arbor, the central pillar of this town's coffee scene was Mighty Good Coffee. Their drip coffee was affordable and tasty, and their espresso drinks were extremely consistent; I was a devotee of their $3 cortado, which fueled much of the research that made its way into this dissertation. In October 2018, I was excited to learn that the baristas had voted to form an employees' union, the Washtenaw Area Coffee Workers' Association (WACWA). Disappointingly, the owners closed their cafés in April 2019 amidst contract negotiations with the union[6], laying off their unionized baristas on short notice while continuing their bean roasting business; I can't in good conscience continue to patronize their business.

**Argus Farm Stop** — In the dark, overcast days of wintertime, their greenhouse space can be a godsend. Once Spring arrives, though, I find myself exclusively gravitating to other cafés, in part because of this spot's slightly out-of-the-way location. Still, it's a great off-campus spot to have a cup of coffee with someone and enjoy the natural light.

**Lab Cafe** — I want to like this café more, but the clientele gravitates towards an undergrad-centric, "cool sorority girl" vibe, which isn't what I'm usually looking for in a café. It's my preferred near-campus spot to grab a friendly coffee with someone,

[6] `https://www.mlive.com/news/ann-arbor/2019/04/baristas-protest-short-notice-layoffs-at-mighty-good-coffee.html`

though!

**Elixir Vitae** — Mainly notable because they offer a discount to GEO (grad student union) members, and because I had my first-ever cortado here. I was turned off from this café partly because of a really rude barista.

**Stovetop Roasters** — For six months in 2018, Stovetop operated a pop-up café in the first-floor space of the Bar at 327 Braun Court. Their coffee drinks were always served on a wooden serving platter with a glass of sparkling water and a spoon. It was the best coffee in the Midwest. If they were still operating, they'd sit proudly as number one on this list, even despite the café being a laptop-free space. Their main roaster and barista, Sam Schaefer, now runs **Mockingbird Coffee**, which is building a roastery and tasting room just north of downtown. As of this writing, Mockingbird is not in full operation yet.

**Espresso Royale** — Don't shop here.

**Biggby Coffee** – There's a Biggby location on E Liberty Street. I don't think I've ever bought their coffee. The most notable thing about this coffee company is that for my entire first year here, I was *sure* that it was spelled "Bigby" coffee, and I had a weird Mandela Effect[7] moment when I finally noticed that there are two "g"s in the name.

[7]The Mandela Effect: `https://rationalwiki.org/wiki/Mandela_effect`

# BIBLIOGRAPHY

# BIBLIOGRAPHY


Adams, F. C., & Shu, F. H. 1986, *ApJ*, 308, 836

Adande, G. R., Woolf, N. J., & Ziurys, L. M. 2013, Astrobiology, 13, 439

Agúndez, M., Marcelino, N., Cernicharo, J., Roueff, E., & Tafalla, M. 2019, *A&A*, 625, A147

Albarede, F., Ballhaus, C., Blichert-Toft, J., et al. 2013, *Icarus*, 222, 44

Alexander, C. M. O. ., Bowden, R., Fogel, M. L., et al. 2012, Science, 337, 721

Alexander, C. M. O. ., Cody, G. D., De Gregorio, B. T., Nittler, L. R., & Stroud, R. M. 2017, Chemie der Erde / Geochemistry, 77, 227

Alexander, C. M. O. ., Fogel, M., Yabuta, H., & Cody, G. D. 2007, *Geochim. Cosmochim. Acta*, 71, 4380

Alexander, C. M. O. D., Grossman, J. N., Ebel, D. S., & Ciesla, F. J. 2008, Science, 320, 1617

Altwegg, K., Balsiger, H., & Fuselier, S. A. 2019, Annual Review of Astronomy and Astrophysics, 57, null

Anders, E., & Grevesse, N. 1989, *Geochim. Cosmochim. Acta*, 53, 197

Andrae, R., Schulze-Hartung, T., & Melchior, P. 2010, ArXiv e-prints, arXiv:1012.3754

Andre, P., Ward-Thompson, D., & Barsony, M. 1993, *ApJ*, 406, 122

André, P., Men'shchikov, A., Bontemps, S., et al. 2010, *A&A*, 518, L102

Andron, I., Gratier, P., Majumdar, L., et al. 2018, *MNRAS*, 481, 5651

Askne, J., Hoglund, B., Hjalmarson, A., & Irvine, W. M. 1984, *A&A*, 130, 311

Bacmann, A., Caux, E., Hily-Blant, P., et al. 2010, *A&A*, 521, L42

Beichman, C., Benneke, B., Knutson, H., et al. 2014, *PASP*, 126, 1134

Bergin, E. A., Blake, G. A., Ciesla, F., Hirschmann, M. M., & Li, J. 2015, Proceedings of the National Academy of Sciences, 112, 8965

Bergin, E. A., & Cleeves, L. I. 2018, Chemistry During the Gas-Rich Stage of Planet Formation, 137

Bergin, E. A., Cleeves, L. I., Crockett, N., & Blake, G. A. 2014, Faraday Discussions, 168, arXiv:1405.7394

Bergin, E. A., Goldsmith, P. F., Snell, R. L., & Ungerechts, H. 1994, *ApJ*, 431, 674

Bergin, E. A., Langer, W. D., & Goldsmith, P. F. 1995, *ApJ*, 441, 222

Bergin, E. A., & Tafalla, M. 2007, *ARA&A*, 45, 339

Bergin, E. A., Phillips, T. G., Comito, C., et al. 2010, *A&A*, 521, L20

Bergner, J. B., Guzmán, V. G., Öberg, K. I., Loomis, R. A., & Pegues, J. 2018, *ApJ*, 857, 69

Bergner, J. B., Öberg, K. I., Bergin, E. A., et al. 2019, *ApJ*, 876, 25

Bergner, J. B., Öberg, K. I., Garrod, R. T., & Graninger, D. M. 2017, *ApJ*, 841, 120

Bertin, M., Doronin, M., Fillion, J.-H., et al. 2017, *A&A*, 598, A18

Bisschop, S. E., Jørgensen, J. K., Bourke, T. L., Bottinelli, S., & van Dishoeck, E. F. 2008, *A&A*, 488, 959

Bockelée-Morvan, D., Calmonte, U., Charnley, S., et al. 2015, *Space Sci. Rev.*, 197, 47

Boogert, A. C. A., Pontoppidan, K. M., Lahuis, F., et al. 2004, *ApJS*, 154, 359

Boogert, A. C. A., Pontoppidan, K. M., Knez, C., et al. 2008, *ApJ*, 678, 985

Borucki, W. J., Koch, D., Basri, G., et al. 2010, Science, 327, 977

Bottinelli, S., Ceccarelli, C., Neri, R., et al. 2004, *ApJ*, 617, L69

Brinch, C., Jørgensen, J. K., & Hogerheijde, M. R. 2009a, *A&A*, 502, 199

—. 2009b, *A&A*, 502, 199

Calcutt, H., Jørgensen, J. K., Müller, H. S. P., et al. 2018a, ArXiv e-prints, arXiv:1804.09210

—. 2018b, *A&A*, 616, A90

Calcutt, H., Fiechter, M. R., Willis, E. R., et al. 2018c, ArXiv e-prints, arXiv:1807.02909

—. 2018d, *A&A*, 617, A95

Carr, J. S., & Najita, J. R. 2008, Science, 319, 1504

—. 2011, *ApJ*, 733, 102

Caselli, P., & Ceccarelli, C. 2012, *A&A Rev.*, 20, 56

Caux, E., Kahane, C., Castets, A., et al. 2011, *A&A*, 532, A23

Cazaux, S., Tielens, A. G. G. M., Ceccarelli, C., et al. 2003, *ApJ*, 593, L51

Ceccarelli, C., Caselli, P., Herbst, E., Tielens, A. G. G. M., & Caux, E. 2007, in Protostars and Planets V, ed. B. Reipurth, D. Jewitt, & K. Keil, 47

Ceccarelli, C., Castets, A., Caux, E., et al. 2000a, *A&A*, 355, 1129

Ceccarelli, C., Loinard, L., Castets, A., Tielens, A. G. G. M., & Caux, E. 2000b, *A&A*, 357, L9

Ceccarelli, C., Bacmann, A., Boogert, A., et al. 2010, *A&A*, 521, L22

Cernicharo, J. 2012, in EAS Publications Series, Vol. 58, EAS Publications Series, ed. C. Stehlé, C. Joblin, & L. d'Hendecourt, 251–261

Cernicharo, J., Kisiel, Z., Tercero, B., et al. 2016, *A&A*, 587, L4

Chandler, C. J., Brogan, C. L., Shirley, Y. L., & Loinard, L. 2005, *ApJ*, 632, 371

Charbonneau, D., Brown, T. M., Latham, D. W., & Mayor, M. 2000, *ApJ*, 529, L45

Charbonneau, D., Brown, T. M., Noyes, R. W., & Gilliland, R. L. 2002, *ApJ*, 568, 377

Charnley, S. B., & Rodgers, S. D. 2008, *Space Sci. Rev.*, 138, 59

Cheung, A. C., Rank, D. M., Townes, C. H., Thornton, D. D., & Welch, W. J. 1968, *Phys. Rev. Lett.*, 21, 1701

—. 1969, *Nature*, 221, 626

Chiar, J. E., Tielens, A. G. G. M., Adamson, A. J., & Ricca, A. 2013, *ApJ*, 770, 78

Chou, H.-G., Yen, H.-W., Koch, P. M., & Guilloteau, S. 2016, *ApJ*, 823, 151

Clayton, D. D., & Nittler, L. R. 2004, Origin and Evolution of the Elements, 297

Cleeves, L. I., Öberg, K. I., Wilner, D. J., et al. 2018, *ApJ*, 865, 155

Codella, C., Ceccarelli, C., Cabrit, S., et al. 2016, *A&A*, 586, L3

Coutens, A., Zakharenko, O., Lewen, F., et al. 2019a, *A&A*, 623, A93

Coutens, A., Vastel, C., Caux, E., et al. 2012, *A&A*, 539, A132

Coutens, A., Willis, E. R., Garrod, R. T., et al. 2018, *A&A*, 612, A107

Coutens, A., Ligterink, N. F. W., Loison, J. C., et al. 2019b, *A&A*, 623, L13

Crimier, N., Ceccarelli, C., Maret, S., et al. 2010, *A&A*, 519, A65

Crockett, N. R., Bergin, E. A., Neill, J. L., et al. 2014a, *ApJ*, 781, 114

—. 2015, *ApJ*, 806, 239

Crockett, N. R., Bergin, E. A., Wang, S., et al. 2010, *A&A*, 521, L21

Crockett, N. R., Bergin, E. A., Neill, J. L., et al. 2014b, *ApJ*, 787, 112

Douglas, A. E., & Herzberg, G. 1941, *ApJ*, 94, 381

Draine, B. T. 2003, *ARA&A*, 41, 241

Drake, F. D. 1962, Intelligent life in space.

Dressing, C. D., & Charbonneau, D. 2015, *ApJ*, 807, 45

Dullemond, C. P., van Zadelhoff, G. J., & Natta, A. 2002, *A&A*, 389, 464

Dumouchel, F., Faure, A., & Lique, F. 2010, *MNRAS*, 406, 2488

Eistrup, C., Walsh, C., & van Dishoeck, E. F. 2018, *A&A*, 613, A14

Enoch, M. L., Evans, Neal J., I., Sargent, A. I., & Glenn, J. 2009, *ApJ*, 692, 973

Enoch, M. L., Young, K. E., Glenn, J., et al. 2006, *ApJ*, 638, 293

Evans, Neal J., I., Allen, L. E., Blake, G. A., et al. 2003, *PASP*, 115, 965

Evans, Neal J., I., Dunham, M. M., Jørgensen, J. K., et al. 2009, *ApJS*, 181, 321

Ewen, H. I., & Purcell, E. M. 1951, *Nature*, 168, 356

Fayolle, E. C., Balfe, J., Loomis, R., et al. 2016, *ApJ*, 816, L28

Foreman-Mackey, D. 2016, corner.py: corner.py v1.0.2, doi:10.5281/zenodo.45906

Foreman-Mackey, D., Hogg, D. W., Lang, D., & Goodman, J. 2013a, *PASP*, 125, 306

Foreman-Mackey, D., Conley, A., Meierjurgen Farr, W., et al. 2013b, emcee: The MCMC Hammer, Astrophysics Source Code Library, ascl:1303.002

Fray, N., Bardyn, A., Cottin, H., et al. 2016, *Nature*, 538, 72

—. 2017, *MNRAS*, 469, S506

Füri, E., & Marty, B. 2015, Nature Geoscience, 8, 515

Furlan, E., Fischer, W. J., Ali, B., et al. 2016, ArXiv e-prints, arXiv:1602.07314

Garrod, R. T., & Herbst, E. 2006, *A&A*, 457, 927

Garrod, R. T., Widicus Weaver, S. L., & Herbst, E. 2008, *ApJ*, 682, 283

Geiss, J., & Gloeckler, G. 1998, *Space Sci. Rev.*, 84, 239

Goesmann, F., Rosenbauer, H., Bredehöft, J. H., et al. 2015, Science, 349, http://science.sciencemag.org/content/349/6247/aab0689.full.pdf

Goldsmith, P. F., & Langer, W. D. 1999, *ApJ*, 517, 209

Gong, Y., Henkel, C., Thorwirth, S., et al. 2015, *A&A*, 581, A48

Goodman, A. A. 2004, in Astronomical Society of the Pacific Conference Series, Vol. 323, Star Formation in the Interstellar Medium: In Honor of David Hollenbach, ed. D. Johnstone, F. C. Adams, D. N. C. Lin, D. A. Neufeeld, & E. C. Ostriker, 171

Goodman, J., & Weare, J. 2010, Communications in applied mathematics and computational science, 5, 65

Gordy, W., & Cook, R. L. 1984, Microwave molecular spectra (Wiley,)

Graninger, D. M., Wilkins, O. H., & Öberg, K. I. 2016, *ApJ*, 819, 140

Green, J. D., Yang, Y.-L., Evans, II, N. J., et al. 2016, *AJ*, 151, 75

Greenberg, R., Wacker, J. F., Hartmann, W. K., & Chapman, C. R. 1978, *Icarus*, 35, 1

Guzmán, V. V., Öberg, K. I., Huang, J., Loomis, R., & Qi, C. 2017, *ApJ*, 836, 30

Guzmán, V. V., Öberg, K. I., Loomis, R., & Qi, C. 2015, *ApJ*, 814, 53

Hasegawa, T. I., & Herbst, E. 1993, *MNRAS*, 261, 83

Hatchell, J., Fuller, G. A., Richer, J. S., Harries, T. J., & Ladd, E. F. 2007, *A&A*, 468, 1009

Henry, G. W., Marcy, G. W., Butler, R. P., & Vogt, S. S. 2000, *ApJ*, 529, L41

Herbst, E., & Klemperer, W. 1973, *ApJ*, 185, 505

Herbst, E., & van Dishoeck, E. F. 2009, *ARA&A*, 47, 427

Heyer, M., & Dame, T. M. 2015, *ARA&A*, 53, 583

Hily-Blant, P., Bonal, L., Faure, A., & Quirico, E. 2013, *Icarus*, 223, 582

Hily-Blant, P., Magalhaes, V., Kastner, J., et al. 2017, *A&A*, 603, L6

Hily-Blant, P., Maret, S., Bacmann, A., et al. 2010, *A&A*, 521, L52

Hirota, T., Bushimata, T., Choi, Y. K., et al. 2008, *PASJ*, 60, 37

Ho, P. T. P., & Townes, C. H. 1983, *ARA&A*, 21, 239

Hogerheijde, M., & van der Tak, F. 2000a, RATRAN: Radiative Transfer and Molecular Excitation in One and Two Dimensions, Astrophysics Source Code Library, ascl:0008.002

Hogerheijde, M. R., & van der Tak, F. F. S. 2000b, *A&A*, 362, 697

Hogg, D. W., & Foreman-Mackey, D. 2018, *ApJS*, 236, 11

Hollenbach, D., Kaufman, M. J., Bergin, E. A., & Melnick, G. J. 2009, *ApJ*, 690, 1497

Ivezic, Z., & Elitzur, M. 1997, *MNRAS*, 287, 799

Ivezic, Z., Nenkova, M., & Elitzur, M. 1999, arXiv e-prints, astro

Jacobsen, S. K., Jørgensen, J. K., van der Wiel, M. H. D., et al. 2017, ArXiv e-prints, arXiv:1712.06984

Jansky, K. G. 1933, *Nature*, 132, 66

Jensen, A. G., Rachford, B. L., & Snow, T. P. 2007, *ApJ*, 654, 955

Johansen, A., & Lambrechts, M. 2017, Annual Review of Earth and Planetary Sciences, 45, 359

Jones, A. P. 2016, Royal Society Open Science, 3, 160221

Jørgensen, J. K. 2011, in IAU Symposium, Vol. 280, The Molecular Universe, ed. J. Cernicharo & R. Bachiller, 53–64

Jørgensen, J. K., Bourke, T. L., Myers, P. C., et al. 2005a, *ApJ*, 632, 973

Jørgensen, J. K., Favre, C., Bisschop, S. E., et al. 2012, *ApJ*, 757, L4

Jørgensen, J. K., Johnstone, D., Kirk, H., & Myers, P. C. 2007a, *ApJ*, 656, 293

Jørgensen, J. K., Schöier, F. L., & van Dishoeck, E. F. 2002, *A&A*, 389, 908

—. 2005b, *A&A*, 435, 177

—. 2005c, *A&A*, 435, 177

Jørgensen, J. K., van Dishoeck, E. F., Visser, R., et al. 2009, *A&A*, 507, 861

Jørgensen, J. K., Bourke, T. L., Myers, P. C., et al. 2007b, *ApJ*, 659, 479

Jørgensen, J. K., van der Wiel, M. H. D., Coutens, A., et al. 2016, *A&A*, 595, A117

Karska, A., Kristensen, L. E., van Dishoeck, E. F., et al. 2014, *A&A*, 572, A9

Kasting, J. F., Whitmire, D. P., & Reynolds, R. T. 1993, *Icarus*, 101, 108

Kepley, A. A., Donovan Meyer, J., Brogan, C., et al. 2016, in Society of Photo-Optical Instrumentation Engineers (SPIE) Conference Series, Vol. 9910, Observatory Operations: Strategies, Processes, and Systems VI, 99100C

Kirk, H., Johnstone, D., & Di Francesco, J. 2006, *ApJ*, 646, 1009

Kirk, H., Johnstone, D., & Tafalla, M. 2007, *ApJ*, 668, 1042

Kissel, J., & Krueger, F. R. 1987, *Nature*, 326, 755

Knauth, D. C., Andersson, B.-G., McCandliss, S. R., & Moos, H. W. 2003, *ApJ*, 596, L51

Knauth, D. C., Andersson, B. G., McCandliss, S. R., & Warren Moos, H. 2004, *Nature*, 429, 636

Kopparapu, R. K., Ramirez, R., Kasting, J. F., et al. 2013, *ApJ*, 765, 131

Kramer, C. 1997

Kristensen, L. E., van Dishoeck, E. F., Mottram, J. C., et al. 2017, *A&A*, 605, A93

Lammer, H., Bredehöft, J. H., Coustenis, A., et al. 2009, *A&A Rev.*, 17, 181

Law, C. J., Öberg, K. I., Bergner, J. B., & Graninger, D. 2018, *ApJ*, 863, 88

Le Gal, R., Öberg, K. I., Loomis, R. A., Pegues, J., & Bergner, J. B. 2019, *ApJ*, 876, 72

Le Roy, L., Altwegg, K., Balsiger, H., et al. 2015, *A&A*, 583, A1

Lee, C.-F., Codella, C., Li, Z.-Y., & Liu, S.-Y. 2019, *ApJ*, 876, 63

Ligterink, N. F. W., Coutens, A., Kofman, V., et al. 2017a, *MNRAS*, 469, 2219

—. 2017b, *MNRAS*, 469, 2219

Ligterink, N. F. W., Calcutt, H., Coutens, A., et al. 2018, *A&A*, 619, A28

Loinard, L., Torres, R. M., Mioduszewski, A. J., & Rodríguez, L. F. 2008, *ApJ*, 675, L29

Loomis, R. A., Cleeves, L. I., Öberg, K. I., et al. 2018, *ApJ*, 859, 131

Looney, L. W., Mundy, L. G., & Welch, W. J. 2000, *ApJ*, 529, 477

Lopez-Morales, M., Currie, T., Teske, J., et al. 2019, in *BAAS*, Vol. 51, 162

Loren, R. B., & Mundy, L. G. 1984, *ApJ*, 286, 232

Lowell, P. 1895, Mars

—. 1906, Mars and its Canals

Lykke, J. M., Coutens, A., Jørgensen, J. K., et al. 2017, *A&A*, 597, A53

Magalhães, V. S., Hily-Blant, P., Faure, A., Hernand ez-Vera, M., & Lique, F. 2018, *A&A*, 615, A52

Maret, S., Ceccarelli, C., Tielens, A. G. G. M., et al. 2005, *A&A*, 442, 527

Maret, S., Hily-Blant, P., Pety, J., Bardeau, S., & Reynier, E. 2011, *A&A*, 526, A47

Maret, S., Ceccarelli, C., Caux, E., et al. 2004, *A&A*, 416, 577

Marty, B. 2012, Earth and Planetary Science Letters, 313, 56

Marty, B., Zimmermann, L., Pujol, M., Burgess, R., & Philippot, P. 2013, Science, 342, 101

Marty, B., Avice, G., Sano, Y., et al. 2016, Earth and Planetary Science Letters, 441, 91

Marty, B., Altwegg, K., Balsiger, H., et al. 2017, Science, 356, 1069

Matthews, C. N., & Minard, R. D. 2006, Faraday Discussions, 133, 393

May, E. M., Gardner, T., Rauscher, E., & Monnier, J. D. 2018a, arXiv e-prints, arXiv:1809.10211

May, E. M., Zhao, M., Haidar, M., Rauscher, E., & Monnier, J. D. 2018b, *AJ*, 156, 122

Mayor, M., & Queloz, D. 1995, *Nature*, 378, 355

McClure, M., Bailey, J., Beck, T., et al. 2017, IceAge: Chemical Evolution of Ices during Star Formation, JWST Proposal ID 1309. Cycle 0 Early Release Scienc

McElroy, D., Walsh, C., Markwick, A. J., et al. 2013, *A&A*, 550, A36

McGuire, B. A. 2018, *ApJS*, 239, 17

McKeegan, K., Aléon, J., Bradley, J., et al. 2006, Science, 314, 1724

McKellar, A. 1940, *PASP*, 52, 187

McMullin, J. P., Waters, B., Schiebel, D., Young, W., & Golap, K. 2007, in Astronomical Society of the Pacific Conference Series, Vol. 376, Astronomical Data Analysis Software and Systems XVI, ed. R. A. Shaw, F. Hill, & D. J. Bell, 127

Messenger, S., Keller, L. P., & Lauretta, D. S. 2005, Science, 309, 737

Morbidelli, A., Lunine, J. I., O'Brien, D. P., Raymond, S. N., & Walsh, K. J. 2012, Annual Review of Earth and Planetary Sciences, 40, 251

Muller, C. A., & Oort, J. H. 1951, *Nature*, 168, 357

Müller, H. S. P., Drouin, B. J., Pearson, J. C., et al. 2016, *A&A*, 586, A17

Müller, H. S. P., Thorwirth, S., Roth, D. A., & Winnewisser, G. 2001, *A&A*, 370, L49

Müller, H. S. P., Brown, L. R., Drouin, B. J., et al. 2015, Journal of Molecular Spectroscopy, 312, 22

Mumma, M. J., & Charnley, S. B. 2011, *ARA&A*, 49, 471

Neill, J. L., Crockett, N. R., Bergin, E. A., Pearson, J. C., & Xu, L.-H. 2013a, *ApJ*, 777, 85

Neill, J. L., Wang, S., Bergin, E. A., et al. 2013b, *ApJ*, 770, 142

Neill, J. L., Bergin, E. A., Lis, D. C., et al. 2014, *ApJ*, 789, 8

Nieva, M.-F., & Przybilla, N. 2012, *A&A*, 539, A143

Noble, J. A., Theule, P., Borget, F., et al. 2013, *MNRAS*, 428, 3262

Öberg, K. I., Boogert, A. C. A., Pontoppidan, K. M., et al. 2008, *ApJ*, 678, 1032

Öberg, K. I., Guzmán, V. V., Furuya, K., et al. 2015, *Nature*, 520, 198

Öberg, K. I., Lauck, T., & Graninger, D. 2014, *ApJ*, 788, 68

Oort, J. H., & van de Hulst, H. C. 1946, Bulletin of the Astronomical Institutes of the Netherlands, 10, 187

Ospina-Zamudio, J., Lefloch, B., Ceccarelli, C., et al. 2018, *A&A*, 618, A145

Ossenkopf, V., & Henning, T. 1994, *A&A*, 291, 943

Oya, Y., Sakai, N., Watanabe, Y., et al. 2017, *ApJ*, 837, 174

Parise, B., Caux, E., Castets, A., et al. 2005, *A&A*, 431, 547

Persson, M. V. 2014, doi:10.6084/m9.figshare.654555.v7

Persson, M. V., Harsono, D., Tobin, J. J., et al. 2016, *A&A*, 590, A33

Persson, M. V., Jørgensen, J. K., & van Dishoeck, E. F. 2013, *A&A*, 549, L3

Pety, J. 2018, in Submillimetre Single-dish Data Reduction and Array Combination Techniques, 11

Pezzuto, S., Fiorellino, E., Benedettini, M., et al. 2017, *Mem. Soc. Astron. Italiana*, 88, 806

Pinilla, P., Benisty, M., & Birnstiel, T. 2012, *A&A*, 545, A81

Plume, R., Bergin, E. A., Phillips, T. G., et al. 2012, *ApJ*, 744, 28

Polanyi, M., & Wigner, E. 1925, Zeitschrift fur Physik, 33, 429

Pontoppidan, K. M., Salyk, C., Banzatti, A., et al. 2019, *ApJ*, 874, 92

Pontoppidan, K. M., Salyk, C., Bergin, E. A., et al. 2014, Protostars and Planets VI, 363

Raunier, S., Chiavassa, T., Duvernay, F., et al. 2004, *A&A*, 416, 165

Raymond, S. N., Kokubo, E., Morbidelli, A., Morishima, R., & Walsh, K. J. 2014, Protostars and Planets VI, 595

Rice, T. S., Bergin, E. A., Jørgensen, J. K., & Wampfler, S. F. 2018, *ApJ*, 866, 156

Ricker, G. R., Winn, J. N., Vanderspek, R., et al. 2015, Journal of Astronomical Telescopes, Instruments, and Systems, 1, 014003

Ridge, N. A., Di Francesco, J., Kirk, H., et al. 2006, *AJ*, 131, 2921

Rodgers, S. D., & Charnley, S. B. 2003, *ApJ*, 585, 355

Romano, D., Matteucci, F., Zhang, Z.-Y., Papadopoulos, P. P., & Ivison, R. J. 2017, *MNRAS*, 470, 401

Roueff, E., Loison, J. C., & Hickson, K. M. 2015, *A&A*, 576, A99

Rubie, D. C., Frost, D. J., Mann, U., et al. 2011, Earth and Planetary Science Letters, 301, 31

Sadavoy, S. I., Di Francesco, J., André, P., et al. 2014, *ApJ*, 787, L18

Sagan, C. 1961, Science, 133, 849

Sakai, N., Hanawa, T., Zhang, Y., et al. 2019, *Nature*, 565, 206

Sakai, N., Oya, Y., Sakai, T., et al. 2014, *ApJ*, 791, L38

Salyk, C., Pontoppidan, K. M., Blake, G. A., Najita, J. R., & Carr, J. S. 2011, *ApJ*, 731, 130

Sandford, S. A., Aléon, J., Alexander, C. M. O. ., et al. 2006, Science, 314, 1720

Sault, R. J., Teuben, P. J., & Wright, M. C. H. 1995, in Astronomical Society of the Pacific Conference Series, Vol. 77, Astronomical Data Analysis Software and Systems IV, ed. R. A. Shaw, H. E. Payne, & J. J. E. Hayes, 433

Schöier, F. L., Jørgensen, J. K., van Dishoeck, E. F., & Blake, G. A. 2002, *A&A*, 390, 1001

Schöier, F. L., van der Tak, F. F. S., van Dishoeck, E. F., & Black, J. H. 2005, *A&A*, 432, 369

Schwarz, K. R., & Bergin, E. A. 2014, *ApJ*, 797, 113

Seager, S. 2018, International Journal of Astrobiology, 17, 294

Seager, S., Bains, W., & Petkowski, J. J. 2016, Astrobiology, 16, 465

Seager, S., & Sasselov, D. D. 2000, *ApJ*, 537, 916

Seager, S., Turner, E. L., Schafer, J., & Ford, E. B. 2005, Astrobiology, 5, 372

Segura-Cox, D. M., Harris, R. J., Tobin, J. J., et al. 2016, *ApJ*, 817, L14

Segura-Cox, D. M., Looney, L. W., Tobin, J. J., et al. 2018, *ApJ*, 866, 161

Shirley, Y. L. 2015, *PASP*, 127, 299

Shu, F. H. 1977, *ApJ*, 214, 488

Snyder, L. E., & Buhl, D. 1971, *ApJ*, 163, L47

Snyder, L. E., Buhl, D., Zuckerman, B., & Palmer, P. 1969, *Phys. Rev. Lett.*, 22, 679

Szőri, M., & Jedlovszky, P. 2014, The Journal of Physical Chemistry C, 118, 3599

Takakuwa, S., Ohashi, N., Bourke, T. L., et al. 2007, *ApJ*, 662, 431

Teague, R., & Foreman-Mackey, D. 2018, Research Notes of the American Astronomical Society, 2, 173

Terebey, S., Shu, F. H., & Cassen, P. 1984, *ApJ*, 286, 529

Testi, L., Birnstiel, T., Ricci, L., et al. 2014, in Protostars and Planets VI, ed. H. Beuther, R. S. Klessen, C. P. Dullemond, & T. Henning, 339

Tielens, A., & Charnley, S. 2013, in Planetary and Interstellar Processes Relevant to the Origins of Life, ed. D. Whittet (Springer Netherlands), 25–51

Times, N. Y. 1933, NEW RADIO WAVES TRACED TO CENTRE OF THE MILKY WAY: MYSTERIOUS STATIC, REPORTED BY K.G. JANSKY, HELD TO DIFFER FROM COSMIC RAY. DIRECTION IS UNCHANGING RECORDED AND TESTED FOR MORE THAN YEAR TO IDENTIFY IT AS FROM EARTH'S GALAXY. ITS INTENSITY IS LOW ONLY DELICATE RECEIVER IS ABLE TO REGISTER – NO EVIDENCE OF INTERSTELLAR SIGNALING, copyright - Copyright New York Times Company May 5, 1933; Last updated - 2010-05-21

Tobin, J. J., Looney, L. W., Li, Z.-Y., et al. 2016a, *ApJ*, 818, 73

—. 2016b, *ApJ*, 818, 73

—. 2018, *ApJ*, 867, 43

Townes, C. H. 1957, in IAU Symposium, Vol. 4, Radio astronomy, ed. H. C. van de Hulst, 92

Trumpler, R. J. 1930, *PASP*, 42, 214

van der Tak, F., & Hogerheijde, M. 2007, ArXiv Astrophysics e-prints, astro-ph/0702385

van der Tak, F. F. S., van Dishoeck, E. F., Evans, Neal J., I., & Blake, G. A. 2000, *ApJ*, 537, 283

van Dishoeck, E. F., & Blake, G. A. 1998, *ARA&A*, 36, 317

van Dishoeck, E. F., Blake, G. A., Draine, B. T., & Lunine, J. I. 1993, in Protostars and Planets III, ed. E. H. Levy & J. I. Lunine, 163–241

van Dishoeck, E. F., Blake, G. A., Jansen, D. J., & Groesbeck, T. D. 1995, *ApJ*, 447, 760

van Kooten, E. M. M. E., Nagashima, K., Kasama, T., et al. 2017, *Geochim. Cosmochim. Acta*, 205, 119

van 't Hoff, M. L. R., Tobin, J. J., Harsono, D., & van Dishoeck, E. F. 2018, *A&A*, 615, A83

Visser, R., Jørgensen, J. K., Kristensen, L. E., van Dishoeck, E. F., & Bergin, E. A. 2013, *ApJ*, 769, 19

Viti, S., Collings, M. P., Dever, J. W., McCoustra, M. R. S., & Williams, D. A. 2004, *MNRAS*, 354, 1141

Wakelam, V., Loison, J.-C., Mereau, R., & Ruaud, M. 2017, Molecular Astrophysics, 6, 22

Wakelam, V., Herbst, E., Loison, J.-C., et al. 2012, *ApJS*, 199, 21

Walsh, K. J., Morbidelli, A., Raymond, S. N., O'Brien, D. P., & Mandell, A. M. 2011, *Nature*, 475, 206

Wampfler, S. F., Jørgensen, J. K., Bizzarro, M., & Bisschop, S. E. 2014, *A&A*, 572, A24

Wang, S., Bergin, E. A., Crockett, N. R., et al. 2011, *A&A*, 527, A95

Weidenschilling, S. J. 1980, *Icarus*, 44, 172

Weinreb, S., Barrett, A. H., Meeks, M. L., & Henry, J. C. 1963, *Nature*, 200, 829

Weiss, L. M., Marcy, G. W., Petigura, E. A., et al. 2018, *AJ*, 155, 48

Whiting, L. 1906, THERE IS LIFE ON THE PLANET MARS: PROF. PERCIVAL LOWELL RECOGNIZED AS THE GREATEST AUTHORITY ON THE SUBJECT, DECLARES THERE CAN BE NO DOUBT THAT LIVING BEINGS INHABIT OUR NEIGHBOR WORLD, copyright - Copyright New York Times Company Dec 9, 1906; Last updated - 2010-05-21

Whittet, D. 2013, Planetary and Interstellar Processes Relevant to the Origins of Life (Springer Netherlands)

Whittet, D. C. B. 2010, *ApJ*, 710, 1009

Whittet, D. C. B., Poteet, C. A., Chiar, J. E., et al. 2013, *ApJ*, 774, 102

Wilson, R. W., Jefferts, K. B., & Penzias, A. A. 1970, *ApJ*, 161, L43

Wilson, T. L. 1999, Reports on Progress in Physics, 62, 143

Wirström, E. S., & Charnley, S. B. 2018, *MNRAS*, 474, 3720

Wirström, E. S., Charnley, S. B., Cordiner, M. A., & Milam, S. N. 2012, *ApJ*, 757, L11

Wood, B. J., Wade, J., & Kilburn, M. R. 2008, *Geochim. Cosmochim. Acta*, 72, 1415

Wright, I. P., Sheridan, S., Barber, S. J., et al. 2015, Science, 349, doi:10.1126/science.aab0673

Wu, J., Dunham, M. M., Evans, Neal J., I., Bourke, T. L., & Young, C. H. 2007, *AJ*, 133, 1560

Wyckoff, S., Tegler, S. C., & Engel, L. 1991, *ApJ*, 367, 641

Youdin, A. N., & Goodman, J. 2005, *ApJ*, 620, 459

Zapata, L. A., Loinard, L., Rodríguez, L. F., et al. 2013, *ApJ*, 764, L14

Zernickel, A., Schilke, P., Schmiedeke, A., et al. 2012, *A&A*, 546, A87